



Detailed Characterization of the Performance of the MAGIC LIDAR Using a 7-year Dataset

Detallierte Charakterisierung der
Leistungsfähigkeit des MAGIC-LIDAR anhand
eines 7-jährigen Datensatzes

A thesis submitted for the degree of
Master of Science

Felix Schmuckermaier

03669155

October 15, 2021

Supervisor: PD Dr. Béla Majorovits

Co-supervisor: PD Dr. Jochen Greiner

Lidar plots show multiple layers of clouds below 5km that change from shot to shot. We keep on with the observations of Crap Crab. We hope someone can make some sense of these data.

Unkown MAGIC shifter

Abstract

The Major Atmospheric Gamma-ray Imaging Cherenkov (MAGIC) telescopes are a system of two Imaging Atmospheric Cherenkov Telescopes (IACTs) located at the Roque de Los Muchachos Observatory, on the Canary island of La Palma at an altitude of 2200 m. With a mirror diameter of 17 m, MAGIC is able to observe gamma radiation between 50 GeV and 50 TeV, making it one of the leading experiments in the field of ground-based gamma-ray astronomy. IACTs make calorimetric use of Earth's atmosphere, which allows these instruments to reach effective areas in the order of km^2 , but also makes them strongly dependent on the quality of the atmosphere at the time of the observations. Changes in the atmospheric conditions due to clouds or dust can affect the shape and brightness of the shower images detected in the telescope cameras, which ultimately can lead to a wrong reconstruction of the gamma-ray data. In order to mitigate this problem, the MPP group built and has been operating a single wavelength elastic LIDAR (LIght Detection And Ranging) system, located next to the MAGIC telescopes, to perform real time ranged-resolved measurements of the atmospheric transmission. This information is then used to quantify the quality of the telescope data, as well as to correct the data taken under suboptimal atmospheric conditions. This work presents a detailed characterization of the correction capabilities of the LIDAR system. This is obtained through a dedicated set of analyses scripts that permit an automated and uniform determination of the accuracy of the applied LIDAR corrections on data from the Crab Nebula spanning over seven years. The study reports the LIDAR performance for a variety of atmospheric conditions and for two different strategies to correct the gamma-ray data. The MAGIC telescopes are currently the only operational IACT using a LIDAR system, and hence this pioneering work will have a positive impact on the performance of MAGIC, and also in that of future Cherenkov telescopes, such as CTA.

Kurzfassung

Die Major Atmospheric Gamma-ray Imaging Cherenkov (MAGIC)-Teleskope sind ein System aus zwei abbildenden atmosphärischen Cherenkov-Teleskopen (IACTs), die sich an Roque de Los Muchachos Observatorium auf der Kanareninsel La Palma in einer Höhe von 2200 m befinden. Mit einem Spiegeldurchmesser von 17 m ist MAGIC in der Lage, Gammastrahlung zwischen 50 GeV und 50 TeV zu beobachten, was es zu einem der führenden Experimente auf dem Gebiet der bodengebundenen Gammastrahlenastronomie macht. IACTs nutzen die Erdatmosphäre kalorimetrisch, was diesen Instrumenten ermöglicht, effektive Flächen in der Größenordnung von km^2 zu erreichen, sie aber auch stark von der Qualität der Atmosphäre zum Zeitpunkt der Beobachtungen abhängig macht. Veränderungen der atmosphärischen Bedingungen aufgrund von Wolken oder Staub können die Form und Helligkeit der von den Teleskopkameras erfassten Schauerbilder beeinflussen, was letztlich zu einer falschen Rekonstruktion der Gammastrahlendaten führen kann. Um dieses Problem zu entschärfen, hat die MPP-Gruppe ein elastisches LIDAR-System (LIght Detection And Ranging) mit einer einzigen Wellenlänge gebaut und in Betrieb genommen, das sich neben den MAGIC-Teleskopen befindet, um Echtzeit-Messungen der über die Entfernung aufgelösten atmosphärischen Transmission durchzuführen. Diese Informationen werden dann verwendet, um die Qualität der Teleskopdaten zu quantifizieren und um die unter suboptimalen atmosphärischen Bedingungen aufgenommenen Daten zu korrigieren. Diese Arbeit stellt eine detaillierte Charakterisierung der Korrekturfähigkeiten des LIDAR-Systems vor, die durch eine Reihe von Analyseskripten gewonnen wird, welche eine automatisierte und einheitliche Bestimmung der Genauigkeit der angewandten LIDAR-Korrekturen an den Daten des Krebsnebels über einen Zeitraum von sieben Jahren ermöglichen. Die Studie zeigt die LIDAR-Leistungsfähigkeit für eine Vielzahl von atmosphärischen Bedingungen und für zwei verschiedene Strategien zur Korrektur der Gammastrahlendaten. Die MAGIC-Teleskope sind derzeit die einzigen in Betrieb befindlichen IACT-Teleskope, die ein LIDAR-System verwenden. Daher wird diese Pionierarbeit Auswirkungen auf die Leistung von MAGIC und auch auf die von zukünftigen Cherenkov-Teleskopen wie CTA haben.

Contents

| | |
|---|-------------|
| List of Figures | viii |
| List of Tables | x |
| List of Acronyms | xi |
| 1 Gamma-ray astronomy | 1 |
| 1.1 High-energy astrophysics | 1 |
| 1.1.1 Cosmic rays | 1 |
| 1.1.2 Gamma rays | 4 |
| 1.1.3 Neutrinos | 6 |
| 1.1.4 Gravitational waves | 6 |
| 1.2 Gamma-ray sources in the Universe | 7 |
| 1.3 Gamma-ray detection | 8 |
| 1.3.1 Satellite-based detection | 8 |
| 1.3.2 Ground-based detection | 9 |
| 2 The MAGIC telescopes and the atmosphere above them | 14 |
| 2.1 The telescope structure and components | 14 |
| 2.2 The trigger system and data analysis chain | 15 |
| 2.3 The ORM site | 16 |
| 2.4 The influence of the atmosphere | 17 |
| 2.4.1 Atmospheric scattering and absorption | 17 |
| 2.4.2 Influence to observations with IACTs | 18 |
| 3 The MAGIC LIDAR system | 20 |
| 3.1 The LIDAR setup | 20 |
| 3.2 Analysis of the LIDAR data | 22 |
| 3.2.1 The LIDAR equation | 22 |
| 3.2.2 Determination of the transmission profile | 23 |
| 3.3 LIDAR-based data correction | 26 |
| 3.3.1 Correction of the energy | 26 |
| 3.3.2 Correction of the effective collection area | 26 |
| 3.3.3 Unfolding of the energy spectra | 28 |

| | | |
|----------|--|-----------|
| 3.3.4 | Alternative method to compute the LIDAR-corrected effective area | 29 |
| 4 | Evaluation of the performance of the LIDAR-based corrections | 32 |
| 4.1 | Construction of the reference spectra | 32 |
| 4.2 | Evaluation of the current performance | 35 |
| 4.2.1 | Methodology | 35 |
| 4.2.2 | Evaluation of the LIDAR performance on a nightly basis | 39 |
| 4.2.3 | Period-averaged results | 50 |
| 4.3 | Comparison of the correction algorithms | 54 |
| 4.3.1 | Comparison of the correction algorithms before unfolding | 54 |
| 4.3.2 | Comparison of the algorithms on unfolded period-averaged spectra | 58 |
| 4.3.3 | Discussion | 62 |
| 5 | Conclusion | 63 |
| | Appendix A Investigation and resolution of recurring LIDAR crashes | 66 |
| | Appendix B A new laser guidance tube and target for laser alignment | 69 |

List of Figures

| | | |
|------|--|----|
| 1.1 | Cosmic-ray energy spectrum | 2 |
| 1.2 | Composition of cosmic rays | 3 |
| 1.3 | Multiwavelength observations of the Crab Nebula | 5 |
| 1.4 | Map of TeV gamma-ray sources | 7 |
| 1.5 | Atmospheric absorption of the electromagnetic spectrum | 8 |
| 1.6 | The Fermi satellite | 9 |
| 1.7 | All-sky map produced by Fermi-LAT | 9 |
| 1.8 | Schematic view of the development of extended air showers | 10 |
| 1.9 | Simulation of air showers with CORSIKA | 10 |
| 1.10 | Schematic view of the Cherenkov effect | 11 |
| 1.11 | Sketch of the imaging atmospheric Cherenkov technique | 12 |
| 1.12 | Selection of currently operating and planned IACTs | 13 |
| | | |
| 2.1 | The location of the ORM on La Palma | 14 |
| 2.2 | The MAGIC telescopes | 14 |
| 2.3 | Several telescopes of the ORM | 16 |
| 2.4 | Satellite image showing Calima | 17 |
| 2.5 | Impact on the transmission of light by atmospheric molecules and aerosols | 18 |
| 2.6 | Emission profile of Cherenkov light for 100 GeV gamma rays | 19 |
| | | |
| 3.1 | Image of the upright LIDAR | 20 |
| 3.2 | CAD image of the LIDAR | 21 |
| 3.3 | LabVIEW user interface to control the LIDAR | 22 |
| 3.4 | Real data example of the range-corrected LIDAR return signal | 24 |
| 3.5 | Extraction of the aerosol transmission profile | 25 |
| 3.6 | Sketch of the energy correction | 27 |
| 3.7 | Sketch of the effective area correction | 27 |
| 3.8 | Example histogram for the migration of events from uncorrected to corrected estimated energy | 30 |
| | | |
| 4.1 | The Crab Nebula | 32 |
| 4.2 | Example reference Crab Nebula spectra | 34 |
| 4.3 | Reference spectra of all included analysis periods | 35 |

| | | |
|------|---|----|
| 4.4 | Influence of the spectral parameters to the log-parabola function | 36 |
| 4.5 | Range corrected photoelectron count on November 13, 2015 | 37 |
| 4.6 | Integrated atmospheric transmission on November 13, 2015 | 37 |
| 4.7 | Example Crab Nebula spectrum, taken on November 13, 2015 | 38 |
| 4.8 | Scatter plot of the flux deviation of individual nights from the reference data to the reference spectrum. | 39 |
| 4.9 | Scatter plot of the flux deviation from the reference spectrum of individual nights . . . | 40 |
| 4.10 | Mean percental and statistical deviation of the flux of the reference data below 250 GeV | 42 |
| 4.11 | Mean percental and statistical deviation of the flux below 250 GeV | 42 |
| 4.12 | Mean percental and statistical deviation of the flux of the reference data between 250 GeV and 1 TeV | 44 |
| 4.13 | Mean percental and statistical deviation of the flux between 250 GeV and 1 TeV | 44 |
| 4.14 | Mean percental and statistical deviation of the flux of the reference data above 1 TeV . | 45 |
| 4.15 | Mean percental and statistical deviation of the flux above 1 TeV | 45 |
| 4.16 | Scatter plot of the percental and statistical parameter deviation of the reference data . | 46 |
| 4.17 | Scatter plot of the percental and statistical parameter deviation | 47 |
| 4.18 | Mean percental and statistical deviation of the amplitude parameter, f , for the reference data | 48 |
| 4.19 | Mean percental and statistical deviation of the amplitude parameter, f | 48 |
| 4.20 | Mean percental and statistical deviation of the index parameter, a , for the reference data | 49 |
| 4.21 | Mean percental and statistical deviation of the index parameter, a | 49 |
| 4.22 | Spectra from the Crab Nebula derived with period-averaged data | 51 |
| 4.23 | Relative difference of the period-averaged spectral fits to the reference spectrum . . . | 52 |
| 4.24 | Percental deviation of the period-averaged spectral fit to the reference spectrum . . . | 53 |
| 4.25 | Comparison of the mean deviations of the flux below 250 GeV | 55 |
| 4.26 | Comparison of the mean deviations of the flux between 250 GeV and 1 TeV | 56 |
| 4.27 | Comparison of the mean deviations of the flux above 1 TeV | 57 |
| 4.28 | Example spectrum showing a better performance of the time algorithm | 58 |
| 4.29 | Example spectrum showing a better performance of the event algorithm | 58 |
| 4.30 | Spectra from the Crab Nebula derived with period-averaged data for different correction algorithms | 59 |
| 4.31 | Relative difference of the period-averaged fspectral its to the reference for different correction algorithms | 60 |
| 4.32 | Percental deviation of the period-averaged spectral fit to the reference spectrum for different correction algorithms | 61 |
| A.1 | Hardware damage and misalignment as a consequence of the LIDAR crash in 2020. . | 67 |
| B.1 | CAD image of the new guidance tube with inserted baffle rings to reduce stray light. . | 69 |
| B.2 | Newly implemented tube setup | 69 |
| B.3 | Attachable target for laser alignment during the day. | 70 |
| B.4 | New laser target | 70 |

List of Tables

- 4.1 Fitted spectral parameters of the reference spectra of all periods. 34
- 4.2 Amount of used data for the given transmission bins. 36

List of Acronyms

| | |
|--------------|--|
| AGN | Active Galactic Nucleus |
| CTA | Cherenkov Telescope Array |
| GRB | Gamma-Ray Burst |
| HPD | Hybrid Photo Detector |
| IACT | Imaging Atmospheric Cherenkov Telescope |
| LIDAR | Light Detection And Ranging |
| MAGIC | Major Atmospheric Gamma Imaging Cherenkov Telescopes |
| MARS | MAGIC Analysis and Reconstruction Software |
| MC | Monte Carlo |
| PMT | Photomultiplier tube |
| PWN | Pulsar Wind Nebula |
| SED | Spectral Energy Distribution |

1. Gamma-ray astronomy

Being one of the oldest natural sciences, astronomy was already practiced by ancient civilizations. Starting out with simple observations by eye and using astronomy as a tool for navigation or making calendars, the only source of information at that time was the visible optical light. The invention of the optical telescope and other auxiliary instruments further improved the scientific capabilities, but optical light still remained the sole cosmic messenger up until the 1930s, when radio waves of cosmic origin were first discovered (Jansky, 1933). Nowadays, the full electromagnetic spectrum is being exploited. From low to high frequency, this involves radio waves, microwaves, infrared, optical light, ultraviolet radiation, X-rays and lastly gamma radiation, which is the form of electromagnetic radiation with the highest energy.

In the following chapter, an introduction to the field of gamma-ray astronomy will be given by first addressing high-energy astrophysics in general, then providing an overview of known cosmic sources of gamma radiation, and finally describing the used detection methods.

1.1 High-energy astrophysics

High-energy astrophysics can be defined as the physics of high-energy processes and their application in astrophysical and cosmological contexts (Longair, 2011). These processes entail the emission of highly energetic electromagnetic radiation, from radio to gamma rays, and other cosmic messengers like high-energy cosmic rays, neutrinos and gravitational waves. The discipline is therefore heavily connected to the field of astroparticle physics, which studies particles of cosmic origin and their relation to astrophysics, cosmology and fundamental physics. Due to this strong connection, the section starts with an overview of cosmic rays, and then gamma rays, neutrinos and finally gravitational waves are covered in the following sections.

1.1.1 Cosmic rays

After the discovery of radioactivity, even present on places without sources of radioactivity, it was believed that this radiation originates from the Earth itself. To test this hypothesis, a number of experiments on balloons were carried out by Victor Hess and Werner Kolhörster. Contrary to their expectation, the measured ionization of the atmosphere due to radiation was increasing at higher altitudes above about 1.5 km, indicating that the radiation originates above Earth's atmosphere. After performing more refined experiments and further investigation, it became apparent that these cosmic rays induced showers of charged particles after their primary interaction with the atmosphere. These

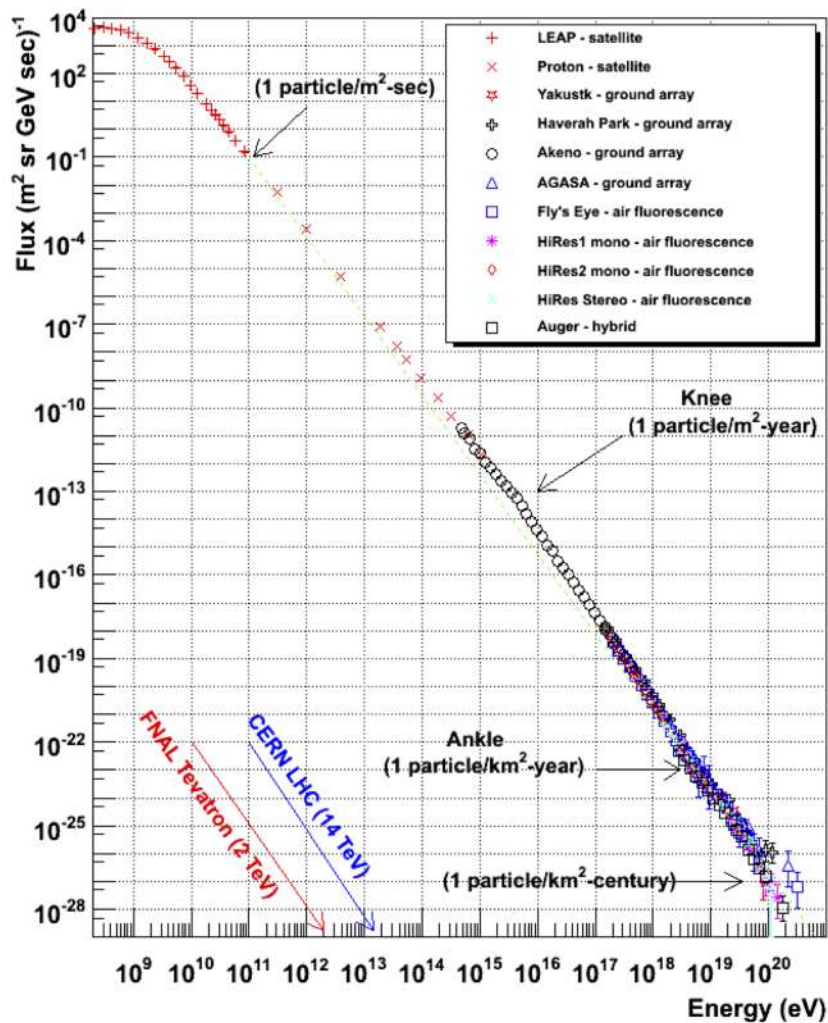


Figure 1.1: The differential cosmic-ray energy spectrum over eleven decades of energy. For reference, the center of mass energy at the Tevatron collider and the LHC is shown in red and blue, respectively. (taken from <http://www.physics.utah.edu/~whanlon/spectrum.html>).

showers can be distributed over 100 m on ground and contain up to millions of ionizing particles. Until the 1950s, when man-made accelerators reached similar energies, studying the particles created in air showers lead to the discovery of a number of new particles, like positrons, muons, kaons or pions (Longair, 2011).

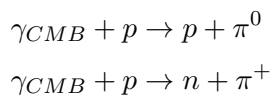
After the discovery of cosmic rays, it was unclear for a while whether primary cosmic rays were consisting of charged particles or gamma radiation. The mystery was resolved, when a change of intensity with latitude as well as a preferred arrival direction from West was discovered, since these effects imply positively charged particles. According to current knowledge, cosmic rays consist primarily of protons heavier nuclei and to a small fraction of electrons/positrons (De Angelis and Pimenta, 2018).

The energies carried by primary cosmic rays cover many orders of magnitude. Image 1.1 shows the flux as a function of energy from GeV up to several EeV obtained by a large number of different experiments. The flux also ranges over many orders of magnitude. At lower energies, around 1 GeV, the fluxes are in the order of several thousand particles per square meter per second, but falls off to

higher energies lower than one particle per square kilometer per year. The behavior of the flux as a function of energy can be approximately described by a power-law function:

$$I(E) \propto E^{-\gamma} \quad (1.1)$$

The spectral index γ is usually in the range of 2.7 to 3.3. Although the distribution follows a power law with a similar spectral index over the whole energy range, small differences in the index lead to observable features in the spectrum. The most notable ones are the so-called knee at an energy of around $5 \cdot 10^{15}$ eV, where γ changes from around 2.7 to 3.1 and the ankle, at around $5 \cdot 10^{18}$ eV, where the spectral index decreases again (De Angelis and Pimenta, 2018). At the highest energies, around $6 \cdot 10^{19}$ eV, the spectrum drops off significantly. The most likely explanation for this behavior is the so called Greisen-Zatsepin-Kuzmin (GZK) suppression. Protons with energies above this threshold will interact with photons of the cosmic microwave background to produce pions via:



Cosmic rays at such energies originating more than 50 Mpc away should therefore not be observable on Earth, and hence create the observed suppression in the spectrum (De Angelis and Pimenta, 2018). However, it is worth mentioning that the presented argument only holds for protons. Current experiments seem to indicate that cosmic rays at highest energies could be primarily made up of heavier nuclei (Aab et al., 2017), in which case, the argument would not apply. As previously mentioned, cosmic rays primarily consist of protons and heavier nuclei. Image 1.2 shows the composition of cosmic rays compared to the abundance of elements in the Solar System. Besides hydrogen and helium, the distribution shows a similar relative abundance of the elements as what is observed in the Solar System.

Depending on the energy region, different mechanisms for acceleration are considered. In the lower energy sector, up until around 1 GeV, the primary source of cosmic rays is the Sun. Solar processes however are not capable of acceleration to higher energies. Several acceleration mechanisms for higher energies are discussed in the literature, where the Fermi mechanism is probably the most relevant one for discussion. In the original Fermi mechanism, charged particles are reflected at so called magnetic mirrors, corresponding to irregularities in the Galactic magnetic field. Multiple stochastic reflections at randomly moving magnetic mirrors can lead to a power-law distribution of particle energies. This

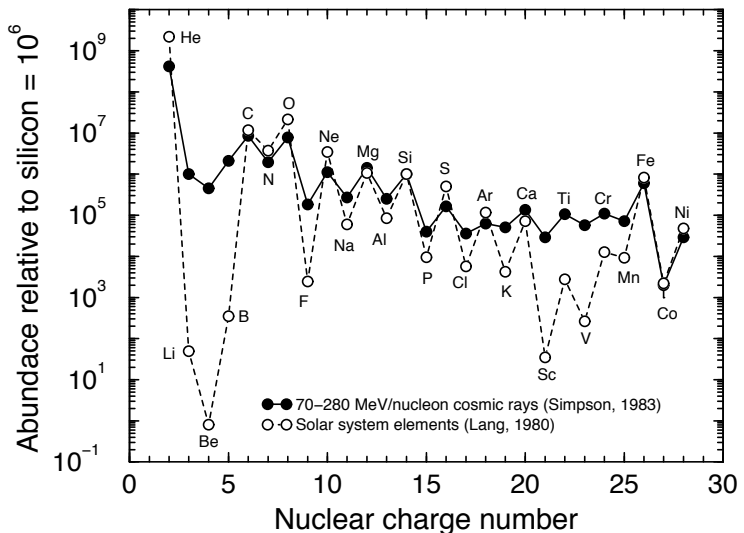


Figure 1.2: The relative elemental abundances of cosmic rays with an energy of 70-280 MeV/nucleon (filled circles) compared to the solar system abundances (open circles) normalized to Si at 10^6 (Mashnik, 2000).

is also called second-order Fermi acceleration, since the average energy gain per reflection depends quadratically on the velocity of the magnetic mirrors. However, the model is insufficient in explaining the concrete value of the resulting spectral index, and ionization losses impede the acceleration of particles from low energies. The more modern picture, also called diffuse shock acceleration or first-order Fermi acceleration, describes particle acceleration via a moving shock front. Here, the average velocity gain depends linearly on the shock velocity and the model results in a power law with spectral index of around -2, resulting in a better agreement with observational data (Longair, 2011).

Since charged particles can be deflected from their trajectory in the presence of magnetic field, cosmic rays generally do not point back to their sources. This makes the identification of sources responsible for the production and acceleration of cosmic rays with the sole study of cosmic rays very challenging. Candidate sources are supernovae, their remnants, gamma-ray bursts or active galactic nuclei. As we will see in the next two sections, sites of hadronic accelerations are also believed to emit gamma rays and neutrinos in the process, making it possible to look for cosmic ray sources with different messengers, that do in fact point back to their sources.

1.1.2 Gamma rays

This section focuses on different emission mechanisms of gamma rays and their connection to cosmic rays. Known cosmic sources of gamma radiation and the techniques for detection are discussed in their respective sections later on.

In general, high-energy photons are produced by an interaction of charged particles with nuclear targets (e.g. molecular clouds), radiation fields (e.g. magnetic fields) or via the decay of heavy particles (De Angelis and Pimenta, 2018). The production mechanisms can be divided into leptonic and hadronic models. Since the instruments discussed in this thesis measure photons with energies larger than 20 GeV, gamma rays emitted by nuclear decays do not play a role in this context.

Leptonic models

Leptonic models include all mechanisms in which highly energetic photons are produced with the involvements of leptons. The three most relevant mechanisms are Bremsstrahlung, synchrotron radiation and the inverse Compton effect.

Bremsstrahlung occurs when leptons, typically electrons, are deflected by the Coulomb field of other charged particles, like atomic nuclei (Longair, 2011).

Synchrotron radiation is produced when charged particles are accelerated radially, meaning perpendicular to their velocity. The power loss of charged particles in the presence of magnetic fields can be expressed by

$$-\frac{dE}{dt} = \frac{e^4 B_{\perp}^2}{6\pi\epsilon_0 c m^2} \beta^2 \gamma^2. \quad (1.2)$$

Due to the inverse dependency on the mass of the charged particle, energy losses, and hence photon yield, are much higher for electrons than protons given the same circumstances.

Regular Compton scattering describes the scattering of a photon by a charged particle, where the interaction results in a decrease of frequency of the photon. However, when highly energetic electrons and lower energy photons are present, the effect can happen inversely. This inverse Compton effect

results in an increase of photon energy due to the scattering process.

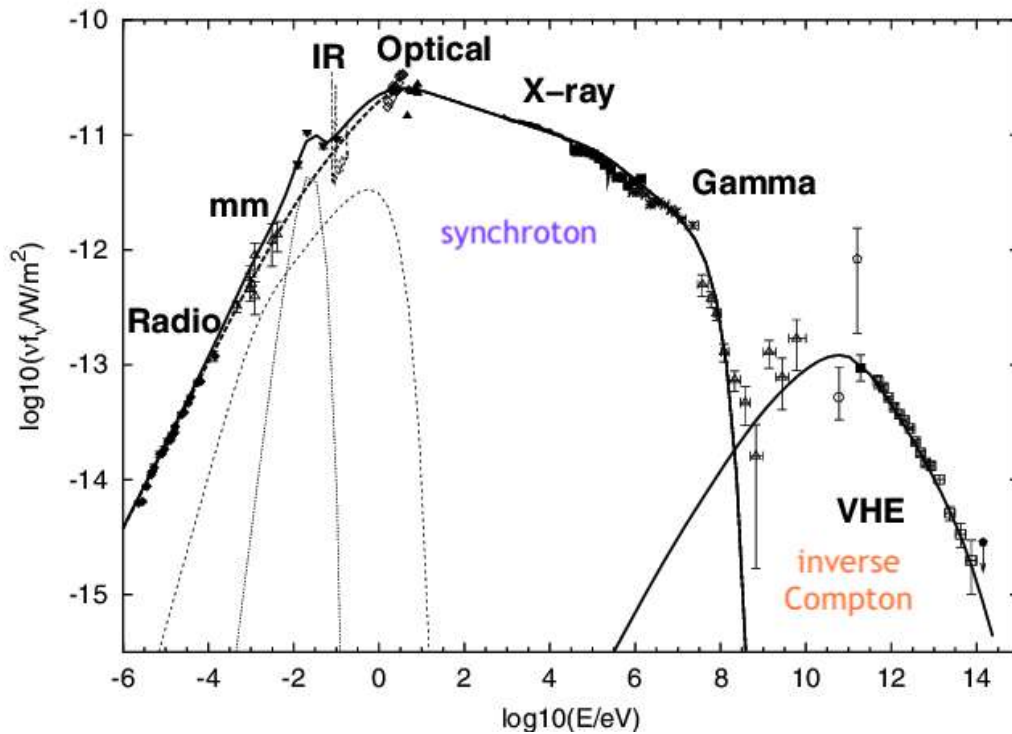


Figure 1.3: Multiwavelength observations of the Crab Nebula. With the SSC emission model, it is possible to explain the entire energy range. The synchrotron radiation emitted by the high-energy electrons starts in radio and extends up until the multi-MeV region. The inverse Compton scattering on the same electrons produces a second peak in the very-high energy gamma radiation up to 50 TeV and beyond (Aharonian, 2005).

A simple complete model for a purely leptonic acceleration mechanism is the self-synchrotron Compton (SSC) mechanism. It describes the process of first creating photons via synchrotron radiation, where the resulting photons create an observable peak in the infrared to X-ray range. The produced photons can then interact with the electrons, which were responsible for their original production, via the inverse Compton effect. The increase of photon energy can produce a second peak in the gamma-ray (GeV-TeV) region in the spectrum. An example of such a complete spectrum is shown in figure 4.1, where the photon spectrum of the Crab Nebula over 20 orders of magnitude in energy is shown.

Hadronic model

Despite the production and acceleration of photons via leptonic interactions, astronomical sources and phenomena capable of hadronic acceleration are also believed to produce high-energy photons. The dominant mechanism for photon production is the favored decay of neutral pions into a pair of gamma rays:

$$\pi^0 \rightarrow \gamma + \gamma$$

Neutral pions are present at sites of hadronic acceleration due to the interaction of cosmic rays with nearby gas or radiation (for example via $\gamma + p \rightarrow p + \pi^0$) and hence a clear identification of sources

emitting photons of hadronic origin would also indicate the acceleration of cosmic rays. Therefore, the study of high energy gamma rays can contribute to the search for sources of high energy cosmic rays (De Angelis and Pimenta, 2018).

1.1.3 Neutrinos

Following the same reasoning as before, cosmic sites of hadronic acceleration also produce charged pions on the side (for example via $\gamma + p \rightarrow n + \pi^+$ or $\gamma + n \rightarrow p + \pi^-$). The produced pions can then decay into electron and muon neutrinos:

$$\begin{aligned}\pi^+ &\rightarrow \mu^+ + \nu_\mu \rightarrow e^+ + \nu_e + \bar{\nu}_\mu + \nu_\mu \\ \pi^- &\rightarrow \mu^- + \bar{\nu}_\mu \rightarrow e^- + \bar{\nu}_e + \nu_\mu + \bar{\nu}_\mu\end{aligned}$$

Due to this connection and the fact that neutrinos can travel undeflected and unabsorbed for very long distances through the cosmos, they are promising messengers to identify the sources of high-energy cosmic rays, and they are sometimes referred to as a *smoking gun* signal (Ahlers, 2019).

On September 22, 2017, the IceCube detector detected a high-energy neutrino with an energy of around 290 TeV, whose arrival direction was consistent with the known blazar TXS 0506+056 in a flaring state as reported by the Fermi-LAT and MAGIC collaborations. A chance correlation of the measurements can be rejected at the 3σ level and therefore suggests that blazars might be a source of high-energy neutrinos and hence cosmic rays (Aartsen et al., 2018).

1.1.4 Gravitational waves

The discipline of combining the above mentioned cosmic messengers is called multi-messenger astronomy. Coincident detection of an astronomical phenomena or sources by more than one cosmic messenger can significantly improve the understanding of the observed object. Also, non-detection by a messenger can yield a higher understanding of the physical processes involved. The fourth messenger in this context are gravitational waves, and hence it is not related to particle physics.

Gravitational waves were first proposed by Henri Poincare in 1905 and later postulated by Albert Einstein as a consequence of describing gravity as a manifestation of the curvature of space-time in his General Theory of Relativity (Cervantes-Cota et al., 2016). The first indirect evidence for gravitational waves was discovered 1974 (Cervantes-Cota et al., 2016) and followed 50 years later by the first direct evidence on September 14, 2015, when the LIGO and VIRGO collaboration announced the detection of gravitational waves signals originating from a binary black hole merger (Abbott et al., 2016). On the 17th of August 2017, the Advanced LIGO and Virgo detectors registered a gravitational wave signal originating from a binary neutron star merger (Abbott et al., 2017). Additionally, the Fermi and INTEGRAL satellite were both able to independently detect a short gamma-ray burst (GRB) 1.7 seconds after the gravitational wave signal. This gives the first direct evidence for an origin model of short GRBs. It confirms that binary neutron star mergers and their associated kilonovae are progenitors of short GRBs, which marks a breakthrough in multi-messenger astronomy, and shows how the combination of different cosmic messengers can yield a better physical understanding of high-energy astrophysical processes.

1.2 Gamma-ray sources in the Universe

Figure 1.4 contains almost 250 sources with gamma-ray emission at TeV energies. Most of the sources were discovered using IACTs, which will be discussed in more detail later on. The map includes galactic as well as extragalactic sources. In the following, some of the most important types of sources of high-energy gamma radiation as well as transient phenomena will be discussed (Spurio, 2018).

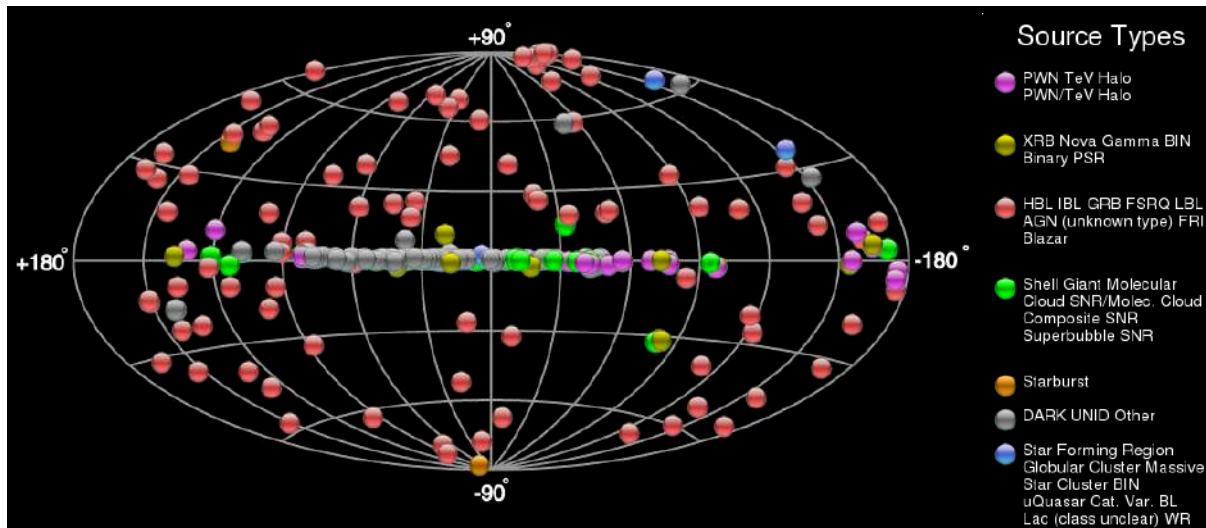


Figure 1.4: Map of TeV gamma-ray sources (2021) (taken from <http://tevcat.uchicago.edu>).

Active galactic nuclei Active galactic nuclei (AGN) are inner regions of galaxies containing super-massive black holes in their center, which are surrounded by an accretion disc. Accretion of matter can lead to the formation of powerful jets with increased emission, making them the one of the most luminous sources of electromagnetic radiation. As can be seen in figure 1.4, AGN are the most abundant observed sources of TeV emission.

Supernova remnants Supernova remnants are the remaining structures from supernovae. Due to the initial stellar explosion, these objects contain shock waves of ejected material expanding into the interstellar medium, making them very plausible candidates for cosmic-ray acceleration.

Pulsars When nuclear fusion becomes unable to sustain the core of very massive stars, they end up in core-collapse supernovae. The remaining cores with masses between around 1.4 and 2.1 solar masses end up as neutron stars, which are very compact and dense objects. Fast rotating neutron stars emitting a strong beam of electromagnetic radiation are called pulsars. Pulsars surrounded by an extended nebula emitting radiation then form pulsar wind nebulae.

Gamma-ray bursts Gamma-ray bursts (GRBs) are very energetic transient phenomena resulting in a strong emission of electromagnetic radiation in a jet-like direction. They can be roughly categorized by their duration into short GRBs (less than two seconds), which are associated with merger events of

two compact objects (i.e. two neutron stars or neutron star and black hole), as discussed previously, and long GRBs (more than two seconds), which are believed to be a result of core collapse supernovae.

1.3 Gamma-ray detection

Observing electromagnetic radiation from Earth contains the inherent difficulty of having Earth's atmosphere along the line of sight. As can be seen in figure 1.5, there are windows in the atmospheric absorption, primarily in the optical and radio regions, where observations from Earth's surface can be performed without the majority of radiation being absorbed. However, for high energies in the gamma-ray region, the atmosphere absorbs 100% of the incoming radiation, making direct detections from the ground impossible. This leads to two main measurement strategies: Either performing measurements above the atmosphere with space-based instruments mounted on satellites or measuring the incoming gamma rays indirectly by observing extended air showers from the ground.

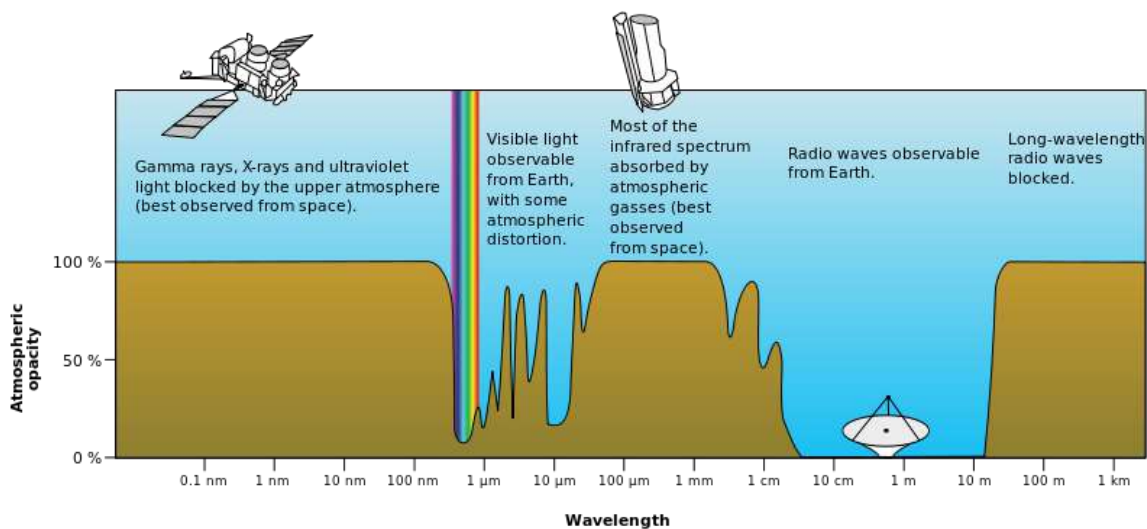


Figure 1.5: Atmospheric absorption of the electromagnetic spectrum from gamma rays to radio waves (taken from <http://www.sun.org/de/images/absorption-of-electromagnetic-radiation-in-the-atmosphere>).

1.3.1 Satellite-based detection

Since the 1960s, satellites are capable of detecting gamma rays of cosmic origin. Several dedicated missions were launched since then, but one of the most successful and currently still operating satellites is the Fermi Gamma-ray Space Telescope, usually only referred to as the Fermi satellite (Atwood et al., 2009). The satellite, figure 1.6, was launched by NASA in 2008 and carries two main scientific instruments. The GBM that operates from a few KeV to about 30 MeV, and the LAT, an imaging gamma-ray detector covering an energy range from around 20 MeV to beyond 300 GeV. LAT is a wide field-of-view detector consisting of an anticoincidence detector, pair conversion foils converting the incoming gamma rays into electron-positron pairs, several tracking detectors to detect the particles trajectory and a calorimeter to estimate the deposited energy. Figure 1.7 shows the energy flux above 1 GeV measured with LAT over the whole sky. Fermi can detect gamma rays with energies upwards



Figure 1.6: The Fermi satellite (taken from <https://science.nasa.gov/toolkits/spacecraft-icons>).

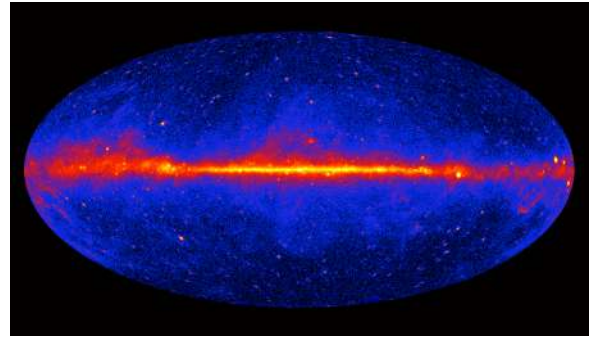


Figure 1.7: All-sky map of the photon flux above 1 GeV produced by Fermi-LAT (taken from https://imagine.gsfc.nasa.gov/observatories/learning/fermi/multimedia/science_gallery.html).

of 300 GeV, but for energies above 100 GeV space-based instruments are more and more limited by poor event statistics. Their small spatial extend results in a limited effective area, which makes the gathering of sufficient data challenging or even impossible for faint sources. As a consequence ground based methods are of great advantage at energies above 100 GeV.

1.3.2 Ground-based detection

Atmospheric air showers

The basis of ground based gamma-ray detection lies in the observations of extended air showers (Spurio, 2018). Extended air showers develop when primary gamma rays or cosmic rays with energies above around 1 GeV strike the atmosphere and initiate a cascade of particles and radiation after their first interaction in the atmosphere. Depending on the type of primary particle, the morphology and content of the resulting shower differs. A primary gamma ray will produce an electron-positron pair in its first interaction. The resulting electron and positron will release additional gamma rays via Bremsstrahlung induced by the nuclei in the atmosphere, as shown in the left part of figure 1.8. The process repeats and an electromagnetic air shower, a cascade of electron, positrons and gamma rays, forms. The cascade effect comes to a halt, when ionization induced by the charged particles becomes the dominant form of energy loss over pair production.

If the primary particle is a cosmic ray, a hadronic shower (figure 1.8 right) will be initiated by interacting with an atmospheric nucleus. At the interaction, a cascade of hadrons, including neutral and charged pions, will be produced. Neutral pions will decay into a pair of gamma rays, where the daughter gamma rays will each initiate an electromagnetic shower. The charged pions will either decay into leptons (muons, electrons and neutrinos) or will produce new hadrons when further interacting with an atmospheric nucleus. Again, the cascade like behavior will continue until energy losses by ionization become dominant.

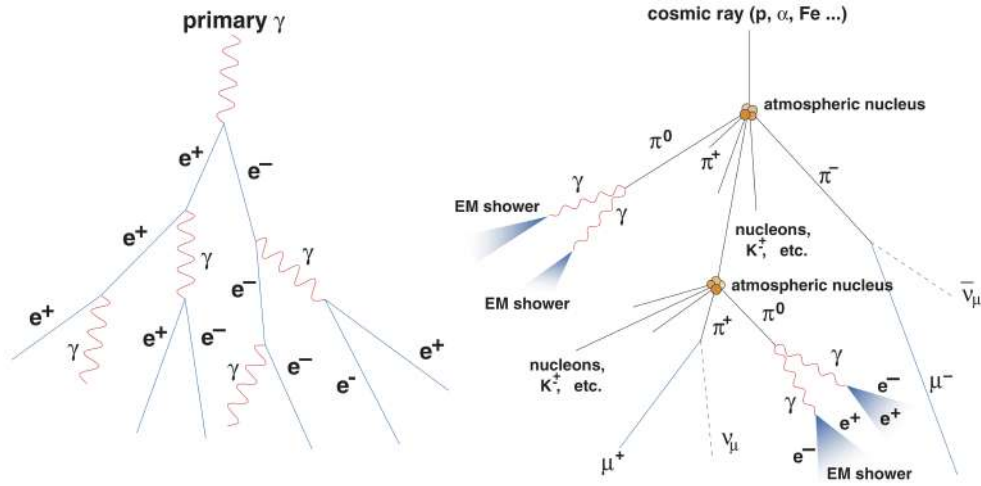


Figure 1.8: Schematic view of the development of an electromagnetic (left) and hadronic (right) air shower (Otte, 2007).

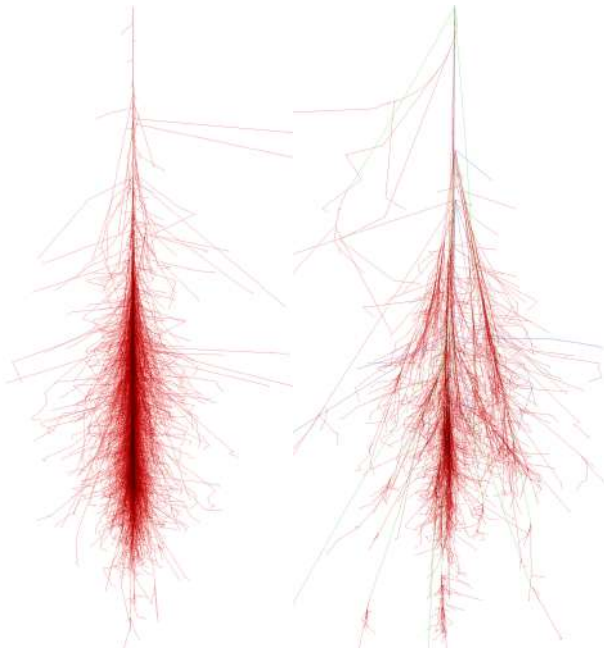


Figure 1.9: Electromagnetic (left) and hadronic (right) air shower simulated with CORSIKA (taken from <https://www.iap.kit.edu/corsika/>).

Despite the particle content, air showers differ in their morphology. Electromagnetic showers have a more uniformly and tighter structure, whereas hadronic showers can have a more fragmented and spread out shape, due to the formation of electromagnetic sub-showers. Examples of simulated showers initiated by a primary gamma ray and cosmic ray with 100 GeV can be seen in figure 1.9. Detecting these air shower and reconstructing the primary particles energy and direction therefore corresponds to an indirect detection of the particle. There are two main methods of measuring air showers: First, measuring Cherenkov light emitted by the secondary particles, and second, directly measuring the secondary particles themselves.

Imaging Atmospheric Cherenkov Telescopes

Cherenkov radiation is emitted when a charged particle travels through a medium faster than the speed of light in that medium. Responsible for the emission is the asymmetrical polarization of the surrounding medium when the charged particle passes, which gives rise to a varying electric dipole moment. The result is a wavefront of light with a peak wavelength in the region of around 300-350 nm

(Spurio, 2018) and a characteristic opening angle given by:

$$\cos\theta = \frac{1}{n\beta} \quad (1.3)$$

For standard conditions in air, the refractive index, n , is about 1.00029, which corresponds to an opening angle of $\theta = 1.3^\circ$ for highly relativistic particles ($\beta \approx 1$) (Spurio, 2018). A sketch of such polarization and the resulting wavefront can be seen in figure 1.10.

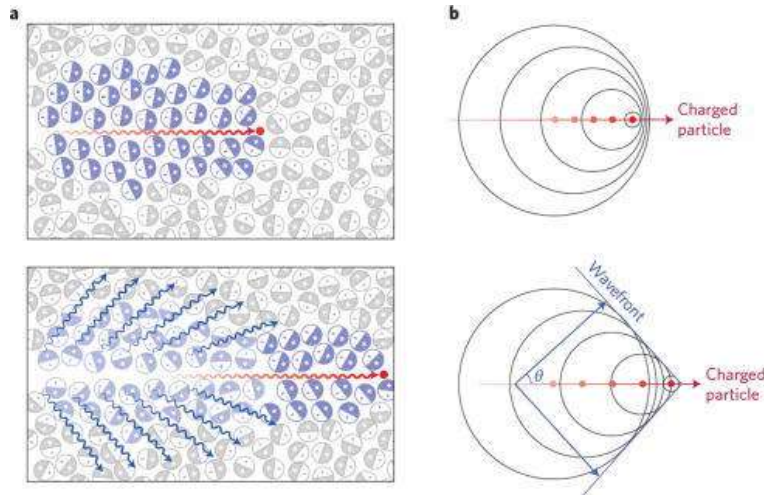


Figure 1.10: Schematic view of the Cherenkov effect (Shaffer et al., 2017).

In order to detect Cherenkov light produced by secondary particles from air showers, telescopes need to combine a large light collection area, high light sensitivity and fast cameras. Imaging atmospheric Cherenkov telescopes (IACTs) meet these requirements by using a large primary mirror with high reflectivity to map an image of the Cherenkov light cone onto a fast, light sensitive camera, usually consisting of an array of photomultiplier tubes (PMTs) (Spurio, 2018). The detection principle and a resulting image of an air shower taken with a PMT array can be seen in figure 1.11.

Compared to satellite experiments, IACTs have the main advantage of using the atmosphere as part of the detector in a calorimetric measurement. This leads to a massive increase in the effective area, which allows the detection of lower fluxes and with that the detection of gamma rays with energies up to around 100 TeV. The method, however, introduces the downside of being exposed to environmental circumstances in the atmosphere. The presence of winds, clouds and other phenomena lead to fast changing conditions that can significantly impair the reconstruction of gamma-ray induced air showers. The underlying problem and methods to address this will be discussed in more detail over the next chapters.

The development of IACTs was pioneered by the Whipple and HEGRA experiments. Currently the second generation of instruments is running with three main experiments: the High Energy Stereoscopic System (H.E.S.S.) in Namibia, the Very Energetic Radiation Imaging Telescope Array System (VERITAS) in Arizona, and the Major Atmospheric Gamma Imaging telescopes (MAGIC), which will be subject of the next chapter, on the Canary Island of La Palma. The third generation of experiments will be realized with the Cherenkov Telescope Array (CTA). CTA will have two sites, the first next to

MAGIC also on La Palma and the second in Paranal in Chile. This way the northern and southern hemispheres are covered, which favors different scientific goals. A selection of currently running and planned IACTs can be seen in figure 1.12.

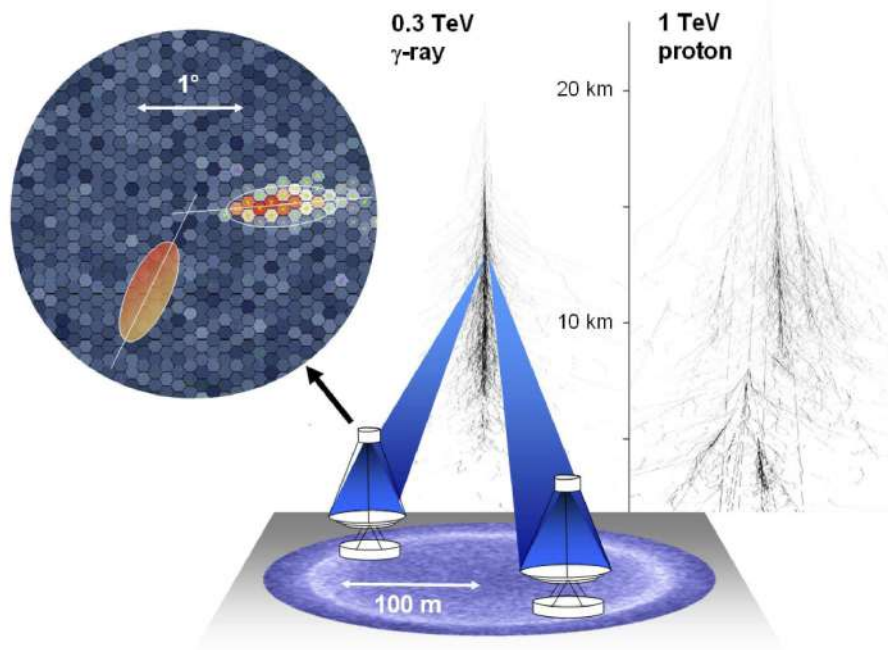


Figure 1.11: Sketch of the imaging atmospheric Cherenkov technique (Hinton and Hofmann, 2009).

Extensive air shower arrays

The second technique to detect VHE gamma rays involves directly measuring the secondary particles at high altitudes with extensive air shower arrays. This enlarges the field of view of the telescope compared to IACTs and allows measurements during day time, resulting in the ability to detect gamma rays with energies beyond 100 TeV. However, extensive air showers suffer from a worse angular resolution compared to IACTs. Two of the leading experiments in this regime are the High Altitude Water Cherenkov (HAWC) observatory and the Large High Altitude Air Shower Observatory (LHAASO).



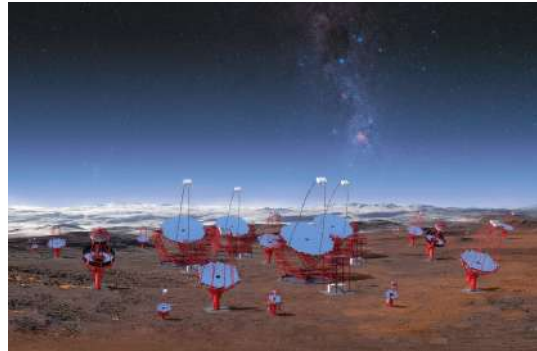
(a) MAGIC



(b) VERITAS



(c) HESS



(d) CTA South

Figure 1.12: Selection of currently operating and planned IACTs (taken from <https://www.mpg.de/593689/pressRelease20090415>, <https://uni-tuebingen.de/en/91800>, https://astro.desy.de/gamma_astronomy/veritas, <https://www.eso.org/public/germany/news/eso1841/>).

2. The MAGIC telescopes and the atmosphere above them

The MAGIC telescopes consist of two IACTs (MAGIC I and MAGIC II) located at an altitude of about 2200m above sea level at the Observatorio Astrofísico del Roque de los Muchachos (ORM) on the Canary island of La Palma (figure 2.1). They started operating in 2003 and 2009, respectively, have both a mirror diameter of 17 m and are placed at a distance of 85 m from each other as shown in figure 2.2. This allows them to detect gamma rays with energies from around 50 GeV up to more than 50 TeV (Aleksić et al., 2016b). Depending on the energy of the primary gamma ray, MAGIC has an energy resolution of around 15% to 25%, and an angular resolution ranging from around 0.09° for low energies up to 0.04° for higher energies above 1 TeV (Aleksić et al., 2016b).

The following chapter provides a short description of the MAGIC telescopes, the atmospheric properties of its site, and the resulting influence on the observation of gamma rays.



Figure 2.1: The location of the ORM on La Palma.



Figure 2.2: The MAGIC telescopes at sunset (Credit: Giovanni Ceribella, 2019).

2.1 The telescope structure and components

Although Cherenkov telescopes observe light in the visible spectrum, their design differs significantly from traditional optical telescopes. IACTs need to be able to resolve Cherenkov light flashes, which are

only a few nanoseconds long and very faint. The requirements for the optical resolution, on the other hand, are much lower. Hence, the MAGIC telescopes consist of only one parabolic mirror to bundle light into the camera system. The mirror has a total diameter of 17 m and consists of 247 individual spherical mirrors approximating the overall parabolic shape. This amounts to a total reflecting area of around 240 m². The underlying structure of the telescopes is made from carbon fiber and steel tubes. Due to the choice of carbon fiber as the main material for the telescope dish, the total weight of the telescope stays relatively low with around 70 t. This enables a repositioning of the telescope to any desired location in about 20-30 s, which is needed for the follow-up observation of short transient events like GRBs. Since the telescope structure can bend slightly different under its own gravitational load, depending on the zenith angle of the telescope, an active mirror control can adjust the individual mirrors to compensate for this effect and restore the desired parabolic shape.

To meet the timing and light sensitivity requirements, the camera of both telescopes consists of an array of PMTs. The cameras are mounted at the top of an aluminium arch, which is additionally fixed by steel cables against lateral movement. PMTs are very sensitive light sensors, and have a time resolution down to the nanosecond timescale, which makes them suitable detector elements for IACTs. The camera of MAGIC I was made up of 577 PMTs, for which both 1 inch and 2 inch diameter PMTs were used. MAGIC II on the other hand uses 1039 1 inch PMTs. In 2011-2012, a big upgrade aimed to improve and unify both telescopes was performed. As a consequence, the camera of MAGIC I now also operates with 1039 pixels made from 1 inch PMTs (Aleksić et al., 2016a). The measured signal from the PMTs gets transferred via optical fiber cables to the so-called Counting House, where the controlling of the telescopes and processing of the data takes place.

2.2 The trigger system and data analysis chain

Besides fast light sensors inside the camera, IACTs also need fast electronics to trigger events, acquire the data and discriminate real events from background light. For MAGIC to detect a primary gamma ray, the resulting signal needs to go through several trigger levels (Aleksić et al., 2016a). An individual telescope is triggered by going through two trigger levels. First, individual pixels of the camera are triggered, if the PMT signal is above a certain threshold value. If then a specific number of neighboring pixels meet this first criteria, the telescope as a whole is triggered. Having two telescopes, a further stereo trigger can be established, which requires both telescopes to trigger coincident to initiate the readout of an event. The stereoscopic combination of two telescopes improves background discrimination, and later on allows for a more accurate reconstruction of the event. The unprocessed raw data of an event are then stored for later offline analysis.

The event reconstruction and analysis taking the data from their raw form to scientific results is being performed by the MAGIC Analysis and Reconstruction Software (MARS) (Zanin et al., 2013). It is a collection of ROOT-based programs written in C++. The first step of the analysis chain consists of calibrating the raw data and extracting the photon signal. The raw data contain the waveform of the electric voltage of all PMTs, when the trigger was initiated. From that, the number of photoelectrons and their arrival time for each PMT is estimated. The resulting data are further cleaned by removing all pixels, that are believed to not originate from the recorded air shower. From the remaining

pixels, the shower image gets parameterized by a small set of parameters describing the shape of the image, and further properties like timing. At the next level, the information from both telescopes get combined to perform the event reconstruction. This includes the discrimination between background and signal events, and the estimation of the primary particle energy and incoming direction. The rejection of background events, which are caused by hadronic showers, is achieved by using machine learning methods, more precisely Random Forests. They get trained with data from sky regions with no expected gamma-ray flux, providing the background events, and simulated gamma-ray events as signal events. For the latter, dedicated Monte Carlo data are produced for different shower energies, zenith angles and further specifications. They aim to accurately model the telescopes behavior by including the complete process from the primary gamma ray striking the atmosphere, to the shower formation, production of Cherenkov light, photon reflection on the mirrors, the photon detection by the PMT cameras, and finally the described event readout. The reconstruction of the energy deposited in the event is then accomplished either by using look up tables, produced using MC data, or again using a Random Forest. Lastly, the incoming direction is estimated from the intersection of the directions given by the single-telescope images. After the event reconstruction, the data can be used to obtain the high-level scientific results. Examples for these are the production of sky maps, the estimation of excess events in a given sky region and, most relevant for this work, the production of energy spectra, which is performed by the MARS program *flute*. These high-level results contain the physics information of the observed sources, and are then being used to address the scientific goals of MAGIC.

2.3 The ORM site

As previously mentioned, MAGIC is located at the ORM on the island of La Palma ($28^{\circ} 45' 42''$ N, $18^{\circ} 53' 25''$ W). The ORM is operated by the Instituto de Astrofísica de Canarias, and hosts a variety of astronomical instruments, including other Cherenkov telescopes and optical telescopes. Especially noteworthy is the Gran Telescopio Canarias, which is currently the largest single aperture telescope in the world, with a primary mirror of 10.4 m diameter. All this makes the ORM one of the most important astronomical sites in the northern hemisphere. The main reason for the high astronomical suitability of the site are the weather conditions at the Canary Islands, which give rise to a very dust-free and dry air and hence provide a good transparency of the sky throughout the year (Puerto-Giménez et al., 2013). Additionally, La Palma has one of the lowest light of the night sky background compared to other astronomical sites (Benn and Ellison, 1998). A dedicated national law (*Ley del Cielo*) protects the light background by regulating the public and private usage of outdoor lighting.



Figure 2.3: Several telescopes of the ORM with stratocumulus clouds in the back.

However, due to its location, some weather phenomena with negative influence on the sky transparency can occur (Fruck, 2015). The islands are located at a latitude of around 30° , which

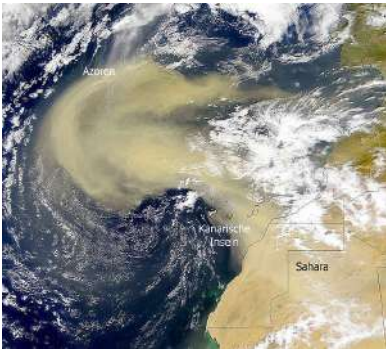


Figure 2.4: Satellite image showing Calima from the Sahara desert (taken from <https://earthobservatory.nasa.gov/newsroom>).

locates them between two large atmospheric cells, namely the Hadley cell in southern direction and the Mid-altitude cell or Ferrel cell in the North. The rotation of the cells gives rise to a prevailing wind direction. Up until 30° , trade winds coming from an eastern direction subsist, which are stronger during summer and hence can further extend North. Between around 30° and 60° , the Westerlies prevail, which are strongest in winter. Since La Palma is situated on the border of both phenomena, it is influenced by both in a seasonal manner. A consequence of the atmospheric circulation is the presence

of a temperature inversion layer at around 1300m above sea level (Puerto-Giménez et al., 2013), where a sea of stratocumulus clouds often can be seen, as in figure 2.3. Below this layer moist maritime air can be found, whereas above it the air is usually dry, and hence free of clouds. Although during winter the stronger Westerlies can cause clouds at all altitudes and hence impair the transparency of the sky. During summer, trade winds can bring large amounts of Saharan dust to the atmosphere above the island, giving rise to a decrease in optical transmission due to higher aerosol scattering in the sky. This is referred to as *Calima* and a satellite image of the phenomena can be seen in figure 2.4.

2.4 The influence of the atmosphere

2.4.1 Atmospheric scattering and absorption

There are several mechanisms that can influence the propagation of the Cherenkov photons in the atmosphere. The main influential ones are absorption bands by molecules and aerosols, as well as scattering caused by molecules (Rayleigh scattering) and aerosols (Mie scattering) (Bernlöhr, 2000). The impact of several mechanisms for different wavelengths can be seen in figure 2.5. It describes the total integral transmission through the atmosphere from a height of 100 km down to 2.2 km as a function of wavelength. Additionally, the individual absorption and scattering mechanisms making up the total transmission are displayed. For short wavelengths, ozone is the most dominant absorber. Below 300 nm it produces an almost total reduction of transmission and quickly loses influence for wavelengths above 310 nm. A similar behavior can be found for oxygen, where the absorption is most dominant below 250 nm. For wavelengths above 310 nm, molecular and aerosol scattering form the strongest impact. Molecular scattering is described by Rayleigh scattering, since the size of the object causing the scattering (mostly nitrogen and oxygen molecules) is much smaller than the wavelengths of light in the UV and optical region. Rayleigh scattering has a dependence on the wavelength as λ^{-4} and hence its influence is stronger for lower wavelengths, and decreases with increasing wavelength. Aerosol scattering is primarily caused by larger particles like water droplets, dust or sea salt in the atmosphere. Since the size of these particles (around 1 nm to 100 μm) is comparable to the considered wavelengths, it can be described by Mie scattering. In figure 2.5 the influence of aerosol scattering is

displayed as a linearly decreasing impact and becomes dominant over the molecular part at around 475 nm for standard atmospheric conditions.

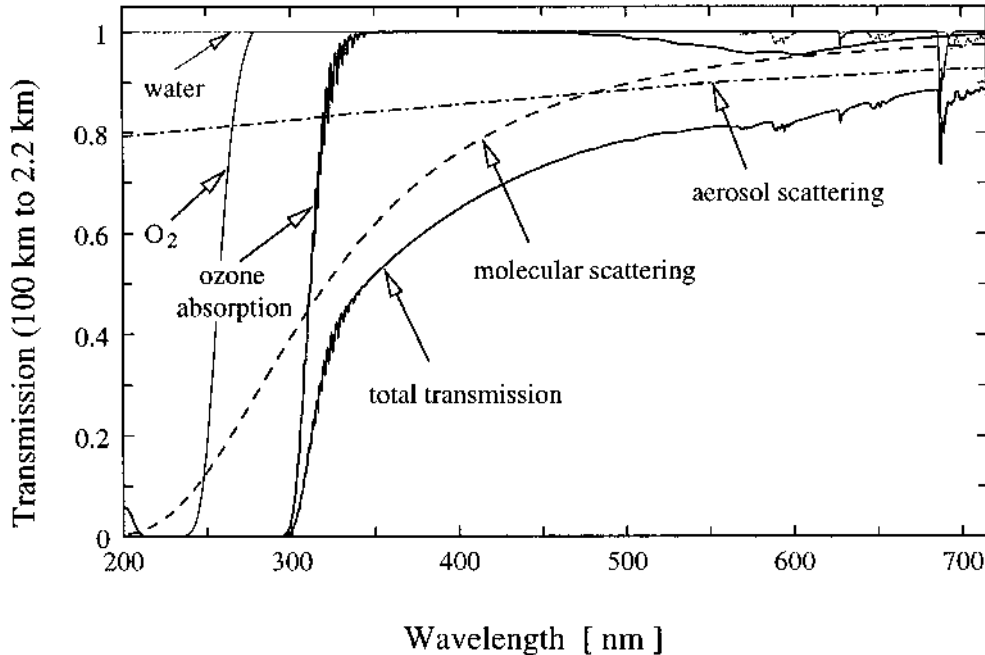


Figure 2.5: Impact on the transmission of light from 100 km altitude down to 2.2 km from the most important absorbers and scatterers (Bernlöhr, 2000).

2.4.2 Influence to observations with IACTs

Most of the mass of the atmosphere is contained in the Troposphere and Stratosphere, corresponding to an altitude up to around 50 km. Hence, primary gamma rays interact primarily far below 50 km altitude, due to the higher atmospheric density. The atmospheric composition up to an altitude of around 20 km, where the density is largest, has, therefore, the most influence on the observation of gamma-ray showers with IACTs. Since the primary interaction is followed by a cascade-like production of particles, which decreases again when the energy losses by ionization become dominant, the emission profile of Cherenkov photons roughly matches a Gaussian distribution in height. Figure 2.6 shows the emission profile of Cherenkov light for four different atmospheric models. Most simulations of air showers rely on the U.S. Standard Atmosphere model (Bernlöhr, 2000). The left plot shows the total emission of photons along the shower axis for different heights. The U.S. std shows a shower maximum at around 9-10 km. For atmospheric models with colder atmospheres, this maximum is shifted downwards to regions of higher density, whereas for the tropical model the maximum lies a bit higher. The right image displays the profile of only photons arriving within 50 m of the shower core at an observation level of 2200 m altitude. The distributions are more asymmetric, since photons emitted at lower altitudes arrive within a tighter area.

Molecular absorption and scattering are relatively well understood and do not vary significantly at a particular site over time. However, the aerosol content of the atmosphere can vary strongly due to the present climatic conditions, which can vary on a timescale of minutes up to a seasonal variability.

As previously mentioned, during the winter months there is an increased presence of clouds. This can increase the aerosol scattering and absorption due to a higher density of water droplets at high altitudes. In summer, Calima can increase the aerosol content significantly at low altitudes. Both can

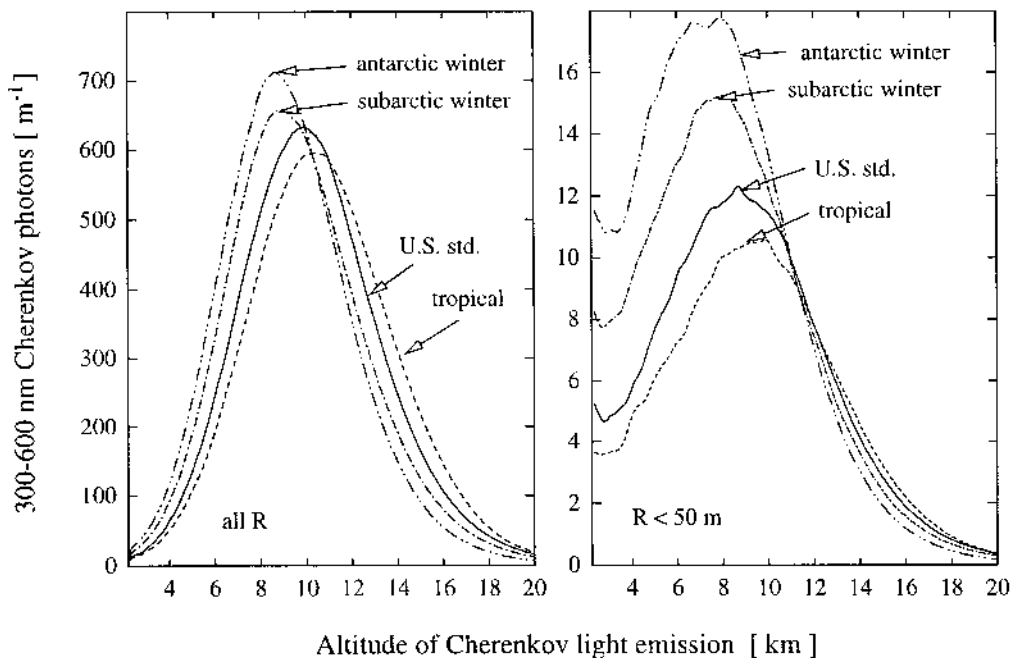


Figure 2.6: Left: Total emission of Cherenkov light as a function of height for air showers originating from 100 GeV gamma rays for four different atmospheric profiles. Right: Same profile, but only including photons arriving within 50 m of the shower core at an observation level of 2200 m. (Bernlöhr, 2000).

impair the transmission of Cherenkov light, as described in the previous section, and hence can impair the accuracy of reconstructing the properties of the primary gamma rays.

The decreased atmospheric transmission reduces the overall number of detected Cherenkov photons emitted by a given air shower. This makes the shower appear less luminous compared to perfect atmospheric conditions. The total light yield of a shower is roughly proportional to the energy of the primary particle. The fewer number of detected photons thus leads to an underestimation of the reconstructed energy. Additionally, the impaired transmission affects the telescopes trigger efficiency. The lower total light yield leads to a less luminous image on the PMT camera, which might prevent a telescope to trigger on an event, which would have triggered the telescope under clear atmospheric conditions. This effect modifies the detection probability of events and with that the effective area, especially for lower energies. A partial sky coverage by clouds might also lead to a distortion of the projected shower image. This can impair the gamma-hadron separation and again lead to a worse total event reconstruction. For all these reasons, IACTs need to implement a method of atmospheric monitoring. The main instrument of the MAGIC collaboration is a Light Detection and Ranging (LIDAR) system for the range-resolved monitoring of atmospheric scattering. Its objectives, structure and methodology will be subject of the next chapter.

3. The MAGIC LIDAR system



Figure 3.1: Image of the upright LIDAR taken in November, 2020.

MAGIC is operating a number of instruments for atmospheric monitoring. Most of these instruments provide information about the general weather conditions, like humidity or clouds. These criteria can be used to determine whether the data taken with MAGIC meet certain quality standards, but cannot be used to correct data taken under suboptimal conditions. In order to correct data, the atmospheric transmission profile needs to be known. To obtain the required range-resolved information about the atmospheric transmission, the MAGIC collaboration operates a LIDAR system (fig. 3.1). The working principle is the following: The LIDAR shoots a laser beam close to the direction of the currently observed coordinates, collects the backscattered light with a mirror, and detects the photons with a detector module in the focal point.

Arrival time and intensity of the backscattered light can then be used to create a range dependent profile of the atmospheric transmission. Section 3.1 describes the current setup of the LIDAR, followed by section 3.2 covering the analysis of LIDAR data, and section 3.3 shows how to correct data taken with the MAGIC telescopes.

3.1 The LIDAR setup

The LIDAR is located in a protective dome on top of a small tower, on the roof of the Counting House. Inside the tower, the control for the mount and supply voltages as well as the readout PC is located. A CAD image of the LIDAR with all its components is shown in figure 3.2. The structural base of the LIDAR is provided by a commercially available equatorial telescope mount, the Astelco NTM 500. To raise the LIDAR over the edge of the protective dome, and hence increase the observable zenith-angle range, the mount is raised with steel beams by around 33 cm. The telescope mount carries a welded aluminium frame functioning as the telescope tube, on which all other components are attached. The laser used for the LIDAR is a passively Q-switched Nd:YAG laser firing pulses of $25 \mu\text{J}$ energy, operated at a repetition rate of 250 Hz. Naturally, the wavelength of Nd:YAG lasers is at 1064 nm. Using a non-linear optical material, the frequency can be doubled to a wavelength of 532 nm, which is close to the peak wavelength of Cherenkov light in air, and hence suitable for our purpose. Ideally, the wavelength of the used laser is as close to the peak Cherenkov wavelength as possible to determine the wavelength-dependent transmission accurately. Since this peak lies in the UV region, it is not visible for the human eye, which entails some issues from a safety and practicability standpoint.

As a compromise, 532 nm was chosen as the favored wavelength. The laser beam directly enters a beam expander, which widens the beam width by a factor of 20 to reduce the beam divergence to around 0.9 mrad. From the beam expander, the laser beam enters a guidance tube containing baffle rings to further reduce any remaining stray light. The whole laser setup is mounted on a plate that can be adjusted along two axes. This way, the laser can be manually aligned to achieve a maximal

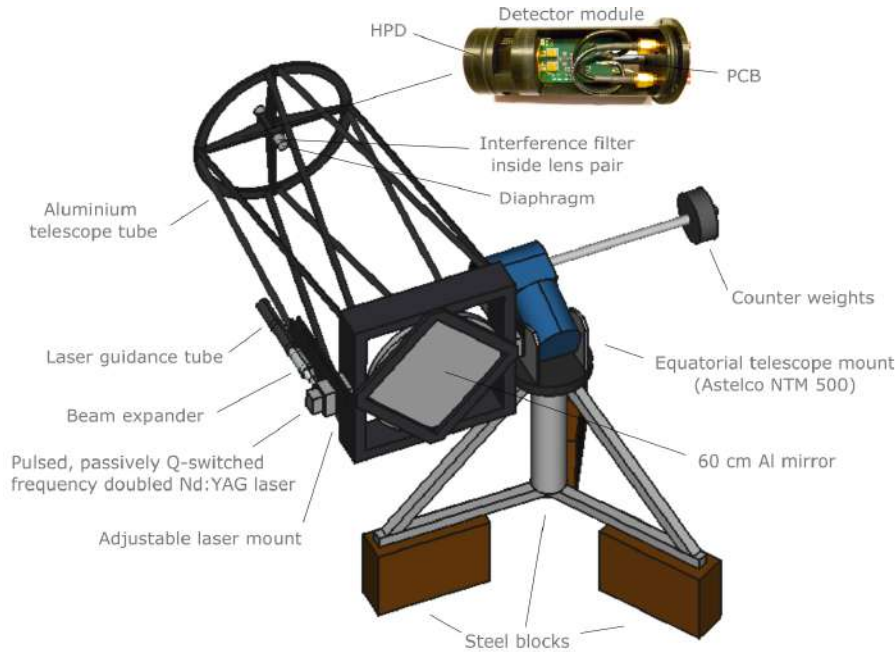


Figure 3.2: CAD image of the LIDAR showing the technical components.

overlap with the telescopes field of view. The backscattered light then gets focused by a 60 cm massive aluminium mirror with a focal length of 150 cm into a diaphragm with an aperture of around 6 mm on the detector module. To reduce the light of the night sky (LoNS) background, a lense parallelizes the backscattered light before it passes an interference filter. The filter has a bandwidth of 3 nm around 532 nm and helps to reduce the LoNS background by over a factor of 100. After that, a second lens focuses the light back into the hybrid photo detector (HPD). For the LIDAR, a Hamamatsu R9792U-40 HPD is used with a quantum efficiency of around 50% at 532 nm (Orito et al., 2009). The HPD uses a GaAsP cathode, and provides single photoelectron resolution at a fast response time. The HPD is supplied by a bias voltage of about 400 V for the incorporated avalanche diode, and a high voltage of 8 kV (generated by a NIM module) for the photocathode. The signal is pre-amplified right after the detector to minimize noise. The amplified signal is then transmitted down to the LIDAR PC, where a FADC card records the signals. Two main readout algorithms then proceed with counting the photoelectrons. The first algorithm is looking for peaks caused by single photoelectrons. This is used for distances above around 4.5 km, where the overlap of multiple single photoelectron peaks become rare. For closer ranges, the second algorithm integrates the waveform and divides by the charge of a single photoelectron.

The LIDAR is controlled via a LabVIEW program providing a user interface used by the MAGIC shifters. A screenshot of the user interface can be seen in figure 3.3. The daily routine operation, as well as specific tests, can be performed from the interface. Under normal operation, the LIDAR

receives the current coordinates of MAGIC and tracks them with a slight offset of 5° to avoid firing the laser inside the MAGIC field of view. Additionally, information about the weather conditions, like humidity and wind speed, is transmitted. This information is evaluated by the LabView program and can trigger a shutdown of the LIDAR system to avoid any damage to the system.

Within the scope of this thesis, a long standing issue in the controlling of the LIDAR was investigated and resolved. Additionally, minor hardware improvements were also performed. A detailed description of these efforts is given in the Appendices A and B.



Figure 3.3: Screenshot of the LabVIEW user interface to control the LIDAR.

3.2 Analysis of the LIDAR data

3.2.1 The LIDAR equation

The analysis of LIDAR data starts with an expression for the differential number of backscattered photons per distance, the LIDAR equation (Fruck, 2015). The light emitted by the laser travels along the optical axis into the atmosphere. Part of the beam is backscattered by the presence of molecules and aerosols. The number of recorded backscattered photons per time can be expressed as the number of photons per distance, dN/dr , due to the constant speed of light. The magnitude of the detected signal depends on several parameters:

- N_0 The number of emitted photons by the laser.
 C_F A calibration factor, containing contributions from e.g. the mirror reflectivity and quantum efficiency of the HPD.
 $G(r)$ A geometric factor, including the overlap of the laser beam and field of view of the LIDAR telescope.
 A/r^2 The solid angle covered by the detector.
 $\beta(r)$ The back-scattering coefficient, consisting of a molecular and aerosol component:
 $\beta(r) = \beta_{mol}(r) + \beta_{aer}(r)$.
 $\alpha(r)$ The extinction coefficient, describing the absorption along the travel path. It also consists of two contributions: $\alpha(r) = \alpha_{mol}(r) + \alpha_{aer}(r)$.

The total number of photons per distance can then be expressed in the form of the LIDAR equation:

$$\frac{dN}{dr} = N_0 C_F G(r) \frac{A}{r^2} \beta(r) \exp\left(-2 \int_0^r \alpha(r') dr'\right) \quad (3.1)$$

Due to the short duration of the laser pulses (FWHM ≈ 1 ns), the differential number of photons can be simply integrated along the digitization length, l :

$$N(r) = \int_{r-\frac{l}{2}}^{r+\frac{l}{2}} dN(r') \approx N_0 C_F G(r) \frac{A}{r^2} \beta(r) l \exp\left(-2 \int_0^r \alpha(r') dr'\right) \quad (3.2)$$

The geometric decrease with distance has the biggest impact on the return signal. To isolate the effect of the atmospheric scattering and absorption, the logarithm of the range-corrected return signal is used (the influence of $G(r)$ diminishes for longer distances):

$$\Sigma(r) = \ln(N(r) \cdot r^2) = \ln(N_0 C_F A l) + \ln(\beta(r)) - 2 \int_0^r \alpha(r') dr' \quad (3.3)$$

Expressed in differential form, this becomes:

$$\frac{d\Sigma(r)}{dr} = \frac{1}{\beta} \frac{d\beta}{dr} - 2\alpha \quad (3.4)$$

Given only one equation but two variables, it is not possible to extract the backscattering and extinction coefficient from the return signal without further assumptions or information.

3.2.2 Determination of the transmission profile

In the case of the MAGIC LIDAR, a special algorithm was developed to extract the aerosol extinction component (Fruck, 2015), which will be later necessary to correct data taken with MAGIC. Figure 3.4 displays an example profile of the range-corrected return signal, which contains the photon counts in bins of 48 m width up to a distance of around 20 km. In general, there are two main cases, where increased aerosol scattering occurs in the atmosphere. First, at the atmospheric boundary layer directly above the ground, which contains a higher aerosol density. The ground layer shows the heaviest aerosol scattering during periods of strong Calima. Second, the presence of clouds can

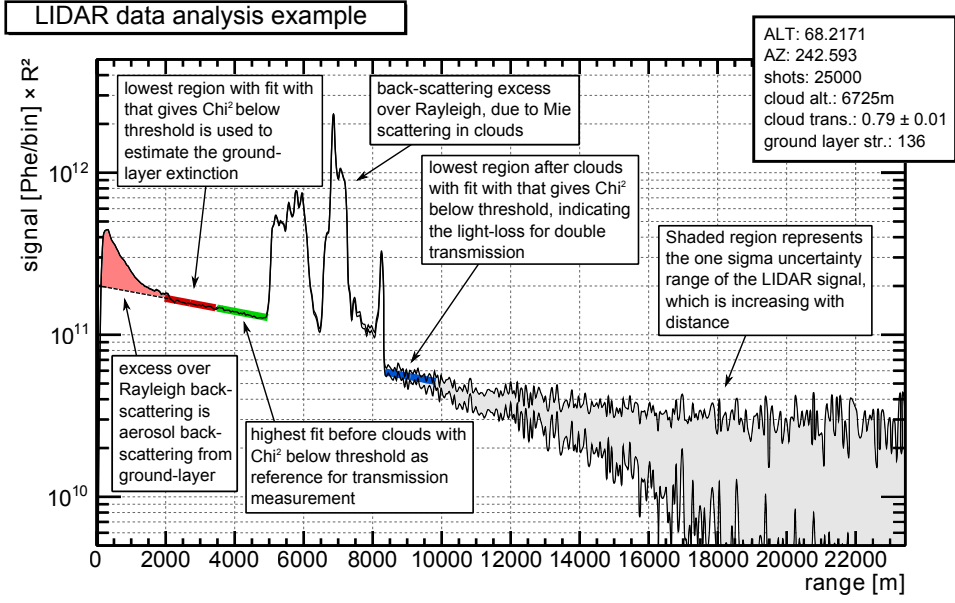


Figure 3.4: Real data example of the range-corrected LIDAR return signal explaining the relevant regions and features of the profile (Fruck et al., 2014).

increase the aerosol scattering above the planetary boundary layer, as it is shown in figure 3.4 at a height of around 6 km. In between, where the atmosphere primarily consists of clear air, Rayleigh scattering on molecules is the dominating form of scattering. The molecular density of the atmosphere decreases exponentially, which leads to a close to exponential decrease of the return signal showing itself in a linear decrease on the logarithmic scale in figure 3.4 for altitudes between 2 km and 5 km. To determine the excess aerosol scattering on top of the molecular Rayleigh scattering, the analysis algorithm first fits a clear-air pure-Rayleigh barometric-density-profile model for all altitudes inside a sliding window:

$$S_{mol}(h) = C \cdot \exp \frac{h}{h_s} \quad (3.5)$$

The profile is parameterized by an amplitude, C , and a scale height, h_s . By evaluating the goodness of the fit with a reduced Chi square, regions of pure Rayleigh scattering can be identified. Sudden worsening and followed improvements of the Chi square value are then used to locate regions of excess aerosol scattering like clouds.

After the identification of a cloud layer, there are two methods of calculating the excess aerosol extinction on top of the molecular Rayleigh scattering. The first method is the "extinction method" and determines the total attenuation of a cloud layer, by comparing the amplitude of the Rayleigh fit before and after the cloud. The transmission of a given cloud can be expressed by taking the square root of the ratio of amplitudes:

$$\tau_{aer} = \sqrt{\frac{C_2}{C_1}} \quad (3.6)$$

For the molecular component of the region covered by the cloud a mean Rayleigh fit can be assumed:

$$\bar{S}_{mol}(h) = \frac{C_1 + C_2}{2} \cdot \exp \frac{h}{h_s} \quad (3.7)$$

The excess of the return signal, $S(h)$, over the Rayleigh fit can then be used to determine the aerosol extinction coefficient:

$$\alpha_{aer}(h) = \sqrt{\frac{C_2}{C_1}} \frac{S(h) - \bar{S}_{mol}(h)}{\int_{h_1}^{h_2} (S(h) - \bar{S}_{mol}(h)) dh} \quad (3.8)$$

As previously discussed, the extinction and backscatter coefficient cannot be extracted from the return signal without further assumptions due to the underconstrained nature of the problem. In order to resolve this, the second method ("LIDAR ratio method") assumes a known and constant value for the LIDAR ratio inside a given cloud. The LIDAR ratio, K , is defined as the ratio between the extinction coefficient over the backscatter coefficient. The aerosol extinction coefficient can then be approximated from the backscattered signal excess above the Rayleigh fit:

$$\alpha_{aer}(h) = K_{aer} \beta_{mol}(h) \frac{S(h) - \bar{S}_{mol}(h)}{\bar{S}_{mol}(h)} \quad (3.9)$$

In the case of optically thin clouds with an absorption of less than 10%, the LIDAR ratio method is more sensitive, whereas for clouds with less transmission, the extinction method is used. In order to later apply corrections, the aerosol extinction coefficient is used to determine the integral aerosol transmission to the ground at h_0 :

$$\tau_{aer}(h) = \int_{h_0}^h \alpha_{aer}(h) dh \quad (3.10)$$

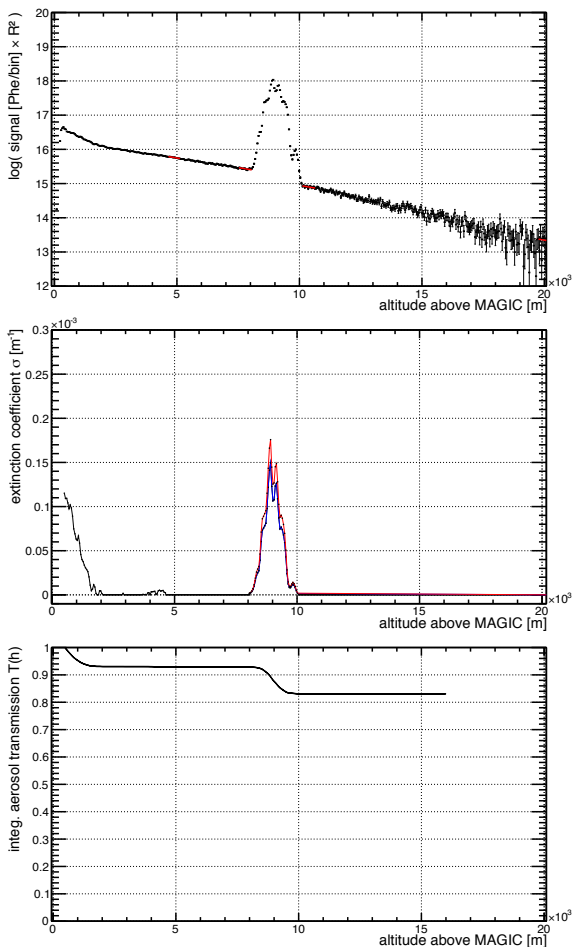


Figure 3.5: Top: Range-corrected return signal showing an excess backscattering due to the ground layer and a cloud layer at around 9 km height. Middle: The aerosol extinction coefficient determined by the LIDAR ratio method (red) and the extinction method (blue). Bottom: Resulting integral aerosol transmission profile. (Fruck et al., 2014).

Figure 3.5 displays an example dataset for the return signal, the corresponding aerosol extinction determined with both methods and the resulting integral transmission.

For the purpose of determining the transmission of the ground layer, the methods described previously cannot be used, since they rely on the Rayleigh fit before and after the given aerosol layer. For the ground layer absorption, the reference is given by measurements taken in nights with perfect clear sky conditions. The transmission by the ground layer can then be determined similar as before:

$$\tau_{g.l.} = \sqrt{\frac{C_0}{C_{ref}}} \quad (3.11)$$

Here, C_{ref} describes the amplitude of the Rayleigh fit under perfect conditions. This approach assumes that

the system stays reasonably stable over time, which is justified within certain error limits. The final resulting integral aerosol transmission as a function of height is then used to perform corrections to the energy spectra obtained with MAGIC.

3.3 LIDAR-based data correction

The ideal case for the analysis of data taken under suboptimal atmospheric conditions would be the usage of tailored Monte-Carlo (MC) data, as it is done for data taken under different zenith angles. Since this would require an enormous amount of data to adequately cover the relevant atmospheric situations, this is not a practical approach. Instead the favored approach relies on the fact that the main observational effect of higher aerosol contents is the decrease of the light content of the measured air shower images. On the other hand, this biases the energy reconstruction of a shower, and on the other, hand decreases the telescopes trigger efficiency. Therefore, one can make the assumption that air showers impaired by atmospheric extinction look similar to showers with smaller energies taken under perfect conditions. In order to correct for this effect, the reconstructed energy gets corrected to account for the lower light content, and the effective area is evaluated at the energy before the correction (Fruck, 2015). In the following, both steps will be outlined.

3.3.1 Correction of the energy

In the event reconstruction, the number of detected photons in a shower image roughly scales linearly with the energy of the primary gamma ray. Assuming a profile for the photon emission of a shower as a function of height, $\epsilon(h)$, one can estimate the atmosphere-induced light yield bias using the transmission profile obtained with the LIDAR. Integrating over the emission profile weighted with the transmission profile results in the average optical depth:

$$\bar{\tau} = \int_0^{\infty} \epsilon(h) \cdot \tau(h) dh \quad (3.12)$$

The emission profile is obtained by estimating the altitude of the shower maximum from stereo reconstruction, and assuming a Gaussian distribution, which is supported by MC simulations. The corrected energy is then obtained by scaling the reconstructed estimated energy with the inverse of the average optical depth:

$$E_{corr} = \frac{E_{est}}{\bar{\tau}} \quad (3.13)$$

Figure 3.6 shows an illustration of the correction process.

3.3.2 Correction of the effective collection area

The effective area of a telescope describes the geometric area weighted with the detection probability. The effective collection area of the MAGIC telescopes is typically calculated from MC data for individual energy bins and zenith angle bins. During low atmospheric transmission, the light yield of events is reduced by aerosol extinction, which impairs the trigger efficiency of MAGIC. This decreases the detection probability, and hence the effective area, especially for lower energies. By first correcting

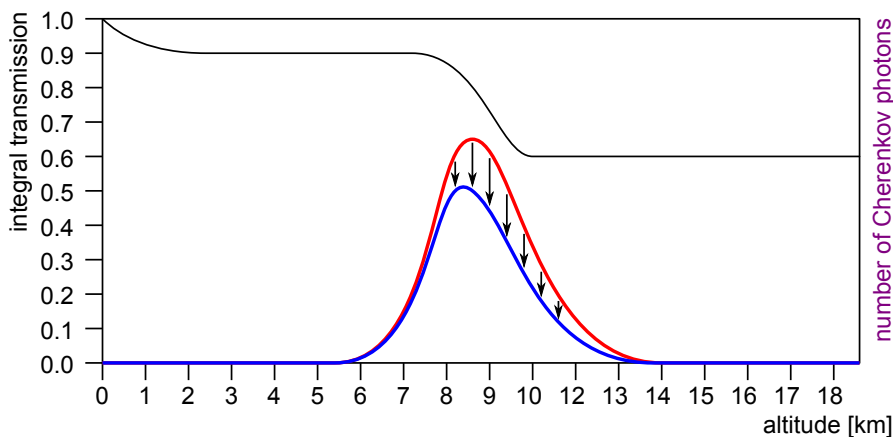


Figure 3.6: Folding of the integral transmission (black) over the assumed light emission (red) results in the corrected emission profile (blue). The number of Cherenkov photons is given in arbitrary units to illustrate the method. Figure from Fruck 2015.

the reconstructed energy, individual events can migrate to a different energy bin and hence a different effective area might apply to them. This would lead to an overestimation of the effective area, and hence to an underestimation of the resulting gamma-ray flux.

But since atmospherically impaired events approximately resemble events with lower energies, the effective area needs to be evaluated before applying corrections to the energy. The resulting effect is that the energy of events get up-scaled, but the effective area is evaluated at smaller energies as it is sketched in figure 3.7. The full correction algorithm averages over the migrating events to recompute the effective area of all energy bins, and it is described in the following.

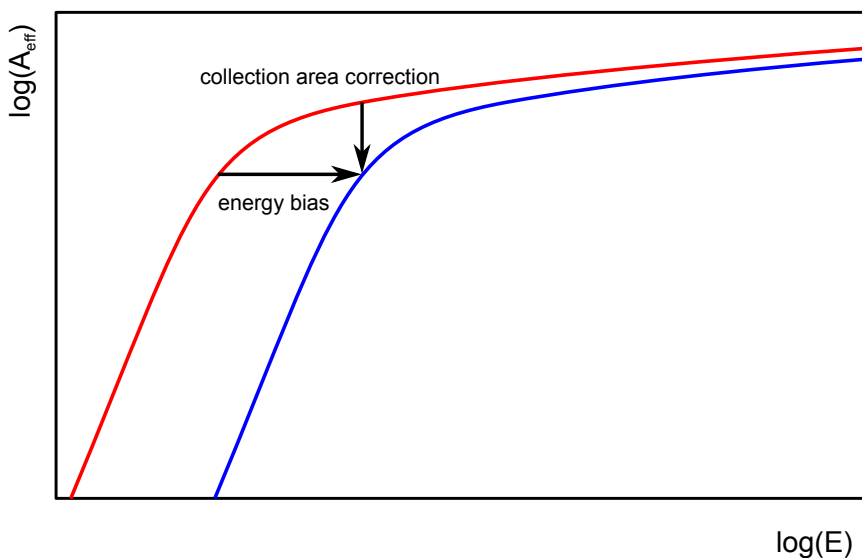


Figure 3.7: Sketch of the resulting shift of the effective area from uncorrected (red) to corrected (blue) energies due to aerosol extinction. Figure from Fruck 2015.

First, the gamma-ray flux is given by evaluating the effective area with the energy bias $\Delta E(t)$, de-

scribing the difference between originally estimated and then corrected energy:

$$F(E, t) = \frac{dN(E, t)}{dt} \cdot \frac{1}{A(E - \Delta E(t), t)} \quad (3.14)$$

Since measurements are always performed over longer periods of time, the average over a time period, T , needs to be taken:

$$\langle F(E) \rangle = \frac{1}{T} \int_0^T \frac{dN(E, t)}{dt} \cdot \frac{1}{A(E - \Delta E(t), t)} dt \quad (3.15)$$

The time element dt in the denominator can be eliminated, and one can integrate over the number of events instead:

$$\langle F(E) \rangle = \frac{1}{T} \int_{N(E, 0)}^{N(E, T)} \frac{dN(E, t)}{A(E - \Delta E(t), t)} \quad (3.16)$$

From this, the transition to a discrete number of events can be performed:

$$\langle F_i \rangle = \frac{1}{T} \sum_{j=0}^{N_i} \frac{1}{A_{i-\Delta E_j, j}} \quad (3.17)$$

The energy bin is given by i , whereas j runs over individual events. ΔE_j gives the energy correction bias of event j in terms of bins. The time-averaged flux expressed with an event averaged collection area, \bar{A}_i , is given by:

$$\langle F_i \rangle = \frac{N_i}{T \cdot \bar{A}_i} \quad (3.18)$$

Equating the terms in eq. 3.16 and 3.17 gives the event-averaged collection area of bin i , that needs to be used to analyse the energy-corrected events:

$$\bar{A}_i = \frac{N_i}{\sum_{j=0}^{N_i} \frac{1}{A_{i-\Delta E_j, j}}} \quad (3.19)$$

3.3.3 Unfolding of the energy spectra

The reconstructed energy up to this point is technically described as estimated energy. Owing to the limited acceptance and resolution of the telescope, threshold effects, as well as inaccuracies of the indirect measurements of gamma rays, there is a distortion of the intrinsic gamma-ray spectrum of the source. The situation can be expressed in the form of matrix notation:

$$U_i = \sum_j M_{i,j} \cdot S_j \quad (3.20)$$

Here, $M_{i,j}$ is the migration matrix, which represents the described effects and contains the probability that an event in bin j of true energy is reconstructed in bin i of estimated energy. It is derived from MC-simulated data. U_i describes the number of events in energy bin i of estimated energy detected by the instrument, and S_j the number of events in bin j of true energy. The process of unfolding (see Albert et al. 2007 for a comprehensive description) aims to better estimate the spectrum in terms of true energy by inverting the expression to obtain S_j . This resembles a matrix inversion problem.

If now individual events are first corrected by using the LIDAR system, an additional migration of

events is introduced. Hence, a second matrix, $H_{j,k}$, is defined, which contains the probabilities of events in the true energy bin k migrating down to the energy bin j due to atmospheric conditions. Taking both components into account, the combined migration matrix is defined as:

$$M'_{i,k} = \sum_j M_{i,j} \cdot H_{j,k} \quad (3.21)$$

It describes the migration of events due to atmospheric extinction first, and then due to the previously described experimental effects, that are related to the intrinsic processes of measuring the gamma rays. The inversion problem then changes to:

$$Y_i = \sum_j M'_{i,j} \cdot S_j \quad (3.22)$$

Y_i describes the number of uncorrected reconstructed events in bin i . There are then several unfolding methods, which differ in their approach of retrieving S_j (Albert et al., 2007).

3.3.4 Alternative method to compute the LIDAR-corrected effective area

As previously described, the effective area of individual events is corrected by evaluating it at the energy before applying the LIDAR based energy correction. Ideally, events would be grouped into sub-samples, which are defined by a given atmospheric condition. The sub-sample would then be analyzed with the corresponding corrected effective area for all energies. However, this has the disadvantage of creating samples with very low statistics, where the gamma-ray excess might be insignificant. This challenges the extraction of fluxes and the likelihood analyses to obtain spectral fits. Hence, larger samples of data with changing conditions are analyzed together, which covers longer time periods, but requires an averaging of the effective area over the different atmospheric conditions occurring during the observation. In the algorithm described in section 3.3.2, the averaging is performed by inversely summing up the effective areas of individual events before the energy correction, as described in equation 3.19. The larger the number of events in a given energy bin j , and hence given effective area, migrating to the new energy bin i for which the effective area is averaged, the larger the effective area of bin j is weighted. The resulting average effective area is, therefore, obtained by using the number of events under a given atmospheric condition as weights. This approach, only holds strictly when the event rate is strictly proportional to the effective area. This assumption can only be strictly justified for signal events, meaning gamma-ray induced events. In real data sets, however, most events are of hadronic nature, even after applying the previously described gamma-hadron separation. Since the proportionality of the event rate to the effective area is not guaranteed for hadronic events, this might introduce inaccuracies. The expected bias of this effect is not too large because the hadron events surviving the selection cuts resemble gamma rays, otherwise they would have been rejected. Additionally, for energy bins where statistics is poor, not many events for the averaging are available, which can also limit the accuracy of the resulting average effective area.

To address the above-described problems, the alternative algorithm version uses the effective observation time of the telescope under a given atmospheric condition as the weight for averaging, instead of

the event rate. In general, the effective time is given by the elapsed time between events, from which the dead time after a recorded event ideally needs to be subtracted. Since the dead time is very small, it can be neglected for this purpose. Image 3.8 shows the migration of all events of an example data set from estimated uncorrected energy to corrected estimated energy using the LIDAR based energy correction. In the previous algorithm, this histogram contains only the number of events traveling

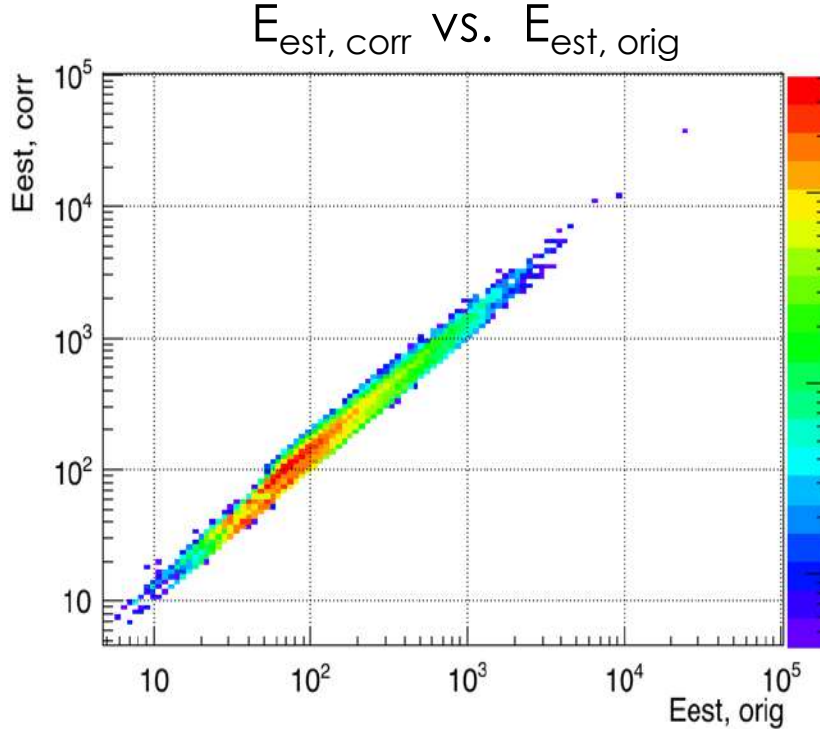


Figure 3.8: Example histogram for the migration of events from uncorrected to corrected estimated energy.

from a given bin of uncorrected to another bin of corrected energy. The current version now fills the histogram with the elapsed time since the last recorded event for all corresponding events. For a given bin combination the elapsed times of all events are summed up. A ratio of two bins, $E_{\text{est,corr},i}/E_{\text{est,orig},j}$, resembles the used correction factor, which equals the integral aerosol transmission. Summing up all bins along the diagonal, where $E_{\text{est,corr}} = E_{\text{est,orig}}$, hence, gives the total time spent under atmospherically perfect conditions, because no energy correction took place. Since statistics, especially for higher energies, can be limited, an energy independence of the correction factor, $E_{\text{est,corr}}/E_{\text{est,orig}}$ is assumed, which could introduce a bias on the other hand. This allows to sum up all bins along the diagonal direction to obtain the total time spent under a certain atmospheric condition and, therefore, where the correction factor had the same value. For the averaging of an effective area of a given energy bin in corrected energy i these total times are used as weights to combine the effective areas of the bins in uncorrected energy j from where events migrated to i . This replaces the previously used average effective area from equation 3.19.

In the transition from the MARS version V2-18-0 to V2-18-1 in February 2018, the implemented correction algorithm was changed by modifying the averaging of the effective area according to the alternative method described in this section (A. Moralejo 2021, priv. comm.). The complete extrac-

tion of the transmission profile from the return signal as well as the correction of the reconstructed energy remains the same. The performance of the two versions of the correction algorithm was initially compared on a small data set covering only four nights. In this work, for the first time, a detailed and comprehensive comparison of the two algorithm versions is obtained. In section 4.3, the results of the comparison of the performance of the two algorithms are presented. In order to abbreviate the two algorithm versions, the algorithm from V2-18-0 will be referred to from now on as the *event algorithm*, whereas the version V2-18-1 as the *time algorithm*, due to their difference in the averaging of the instrument response function.

4. Evaluation of the performance of the LIDAR-based corrections

The following chapter describes the main results of this work. It contains the detailed evaluation of the LIDAR's correction abilities for different atmospheric conditions, energy ranges and zenith angles. To achieve this, a reference data set is defined in the beginning by using data of highest quality to construct reference spectra. Then, the data impaired by atmospheric conditions are analyzed without and with applying LIDAR corrections and compared to the reference data set. The comparison of the corrected and uncorrected data with the reference allows a quantification of the impact of the LIDAR corrections on the data taken under sub-optimal atmospheric conditions. In the final section, the data and analysis pipeline are used to compare two different versions of the correction algorithm.

4.1 Construction of the reference spectra

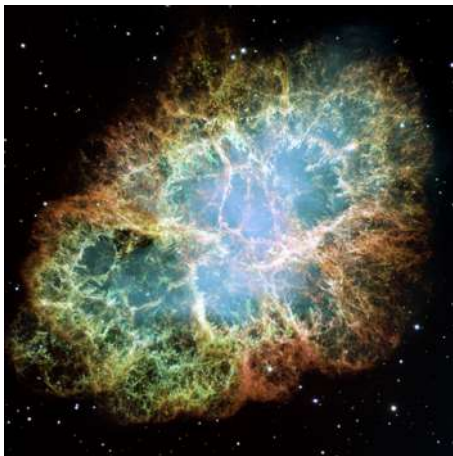


Figure 4.1: Optical image from the Crab Nebula taken by the Hubble Space Telescope (taken from <https://hubblesite.org>).

The Crab Nebula (Aleksić et al., 2015) is a pulsar wind nebula (PWN) originating from a supernova that took place in the year 1054. It is a very young supernova remnant and, with a distance of about 2.0 kiloparsecs from Earth, it is also a relatively close source. In its center lies the Crab Pulsar (PSR B0531+21). It powers the acceleration of relativistic particles, which then provide the basis for the emission in the gamma-ray domain as described in section 1.1.2. The first significant detection of the Crab Nebula at TeV energies was performed by the Whipple Telescope in 1989 (Weekes et al., 1989). The source has been extensively studied by several ground-based gamma-ray telescopes since then, making it one of the best studied non-thermal sources in the sky. It shows a very bright and stable emission along several wavelengths and is considered as a standard candle for many energy regimes including gamma-rays. Due to the stability of the

emission, the observed spectra by MAGIC do not vary significantly more than what can be attributed to the instruments systematics. Hence, if accounted for correctly, the reconstructed spectrum must not depend on the atmospheric transmission or the observational zenith angle. Due to its brightness and stability, the Crab Nebula is observed frequently by MAGIC and there are large amounts of archival

data available. The Crab Nebula was, therefore, chosen as the reference source for this work.

In this study, I analyzed Crab data from mid 2013, shortly after the LIDAR started operating, until early 2020, covering a time period of almost seven years. The Crab Nebula can be observed by MAGIC between September and April. The majority of the data is taken in the colder winter months, when the influence of clouds above the MAGIC site is stronger. The phenomenon of Calima usually occurs from July until September and is therefore represented very little in the given data set. The used data set contains observations taken at zenith angles between 5° and 62° . At even higher zeniths, it becomes increasingly challenging for the LIDAR to reach the necessary heights with its limited range, which makes a sufficient correction for poor atmospheric conditions unattainable. Higher zeniths were hence excluded. Only data taken under *dark* conditions, meaning a low level of night sky background, is used. The strongest source of background light is given by the Moon, so the majority of data come from observations without the presence of moonlight. To quantify the level of background light, the average DC of the PMT anodes in the cameras provides a measurand, since it is increasing proportional to the night sky background. As an upper threshold, a value of $2 \mu\text{A}$ was set.

Before investigating the LIDAR's influence on data taken under sub-optimal atmospheric conditions, a reference for comparison needs to be defined. A simple approach would be to use a single already published spectrum of the Crab Nebula and set it as the reference for all data. However, this approach entails certain downsides. The data set covers a long time period of almost seven years. During this time there were many occasions, where the instrument response of MAGIC changed. Reasons for this can be hardware upgrades or environmental impact like dust deposition on the mirrors. In order to account for known changes in the response function, a new set of MC data is produced, when changes are significant enough. Time frames in which the same MC data applies are referred to as analysis periods. The used data set includes eight analysis periods in total. Since the accuracy of the MC data can vary from period to period, reconstructed spectra can appear slightly different despite originating from a non-varying source. The intrinsic systematic uncertainty of MAGIC on the energy reconstruction is estimated to be below 15% and on the flux normalization to be around 11%-18% (Aleksić et al., 2016b). To have the best possible estimate of how a specific spectra should be reconstructed, the reference spectrum is built from high quality data from the same period.

The data are classified by their concurrent atmospheric transmission from a height of 9 km, $T_{9\text{km}}$. The maximum Cherenkov emission of atmospheric air showers is usually at a height of around 9 km, as described in section 2.4.2. $T_{9\text{km}}$ is used as the standard criteria provided by the LIDAR to estimate the given weather conditions. The general recommendation for the analysis of MAGIC data is that data with a transmission above 0.85 can be used without applying atmospheric corrections. To ensure the data of highest quality are used for the creation of the reference spectra, an even more stringent threshold of $T_{9\text{km}} > 0.93$ was set for this work. In total, around 410 h of Crab data are available in this range over the seven year time span.

A reference spectra is then constructed for every analysis period by fitting the combined data with a log-parabola function:

$$\frac{d\phi}{dE} = f \cdot \left(\frac{E}{200 \text{ GeV}} \right)^{a-b^2 \cdot \log_{10} \left(\frac{E}{200 \text{ GeV}} \right)} \quad (4.1)$$

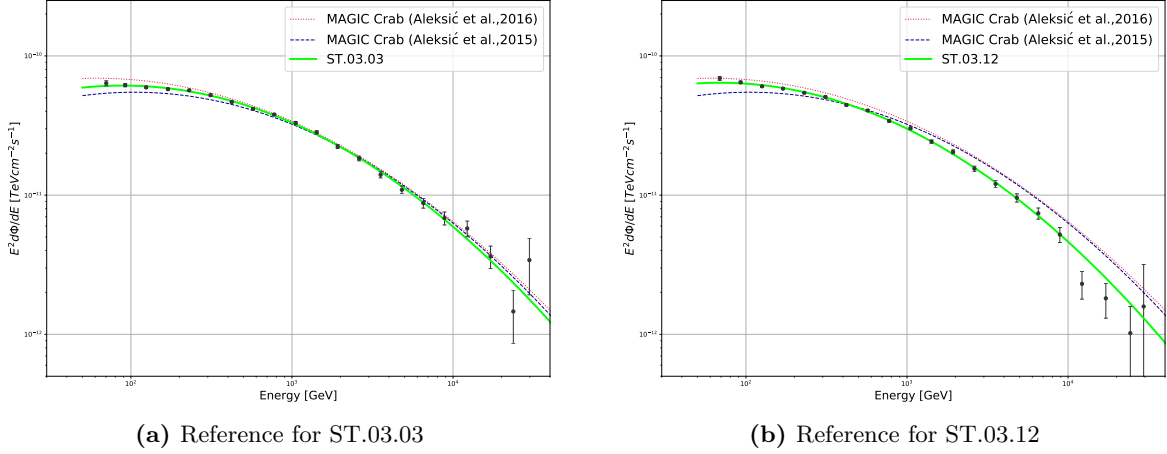


Figure 4.2: Example reference Crab Nebula spectra from the first (ST.03.03) and last (ST.03.12) analysis period used in this study, in comparison to two spectra published by MAGIC.

Figure 4.2 shows two example spectral energy distributions (SEDs) from the first (ST.03.03) and last (ST.03.12) analysis period used in this study. The largest differences in the reconstructed spectra can be observed at the highest energies.

Table 4.1 shows the time period, amount of used data and the fitted spectral parameters of all reference spectra. The analysis period ST.03.03 (marked with *) is interrupted in parts by ST.03.04. The period ST.03.04 is excluded since it only contains stereo data from 27.08.2014 until 30.08.2014 and some mono (only MAGIC II) data from 19.06.2014 until 04.07.2014. Due to its shortness, it does not contain any suitable data. The same applies for period ST.03.08, which covers the time from 02.08.2017 until 02.11.2017 and does not contain usable data for this study.

Table 4.1: Fitted spectral parameters of the reference spectra of all periods.

| Period tag | Time period | Data | f | a | b |
|------------|--------------------------|---------|---------------------------------|------------------|-----------------|
| ST.03.03 | 27.07.2013 - 05.08.2014* | 55.5 h | $(1.43 \pm 0.01) \cdot 10^{-9}$ | -2.17 ± 0.01 | 0.49 ± 0.01 |
| ST.03.05 | 31.08.2014 - 22.11.2014 | 7.4 h | $(1.41 \pm 0.02) \cdot 10^{-9}$ | -2.14 ± 0.03 | 0.53 ± 0.03 |
| ST.03.06 | 24.11.2014 - 28.04.2016 | 136.6 h | $(1.42 \pm 0.01) \cdot 10^{-9}$ | -2.11 ± 0.01 | 0.52 ± 0.01 |
| ST.03.07 | 29.04.2016 - 02.08.2017 | 40.4 h | $(1.43 \pm 0.01) \cdot 10^{-9}$ | -2.23 ± 0.01 | 0.48 ± 0.01 |
| ST.03.09 | 10.11.2017 - 29.06.2018 | 28.9 h | $(1.42 \pm 0.01) \cdot 10^{-9}$ | -2.13 ± 0.01 | 0.52 ± 0.01 |
| ST.03.10 | 30.06.2018 - 30.10.2018 | 16.6 h | $(1.47 \pm 0.02) \cdot 10^{-9}$ | -2.25 ± 0.02 | 0.47 ± 0.02 |
| ST.03.11 | 01.11.2018 - 15.09.2019 | 60.4 h | $(1.48 \pm 0.01) \cdot 10^{-9}$ | -2.25 ± 0.01 | 0.50 ± 0.01 |
| ST.03.12 | 16.09.2019 - 22.02.2020 | 63.4 h | $(1.42 \pm 0.01) \cdot 10^{-9}$ | -2.23 ± 0.01 | 0.49 ± 0.01 |

The top plot of figure 4.3 shows the reconstructed spectra, which were obtained by using a forward unfolding approach implemented in the MARS program *fold*. In order to visualize the relative difference of the spectra, they are all compared to a published Crab spectrum (Aleksić et al., 2016b) in the lower plot by taking the ratio of the SEDs. Again, the spectra differ most in the high-energy region, where data becomes scarce and the statistics is quite low. Here, they can reach a difference as high as 40% in some periods. In general, the published SED shows a larger flux compared to the SEDs

from the included analysis periods of this work. The data used for the publication are covering a time period from October 2013 until January 2014, which is during the first included analysis period, ST.03.03. Therefore, the reference spectra obtained for ST.03.03 shows the best agreement with the published Crab Nebula spectrum. For later periods the deviation becomes larger. Partly unaccounted changes in the instrument response of MAGIC might be the most probable cause for the deviations. The relative difference of the used spectra between each other is, however, much smaller.

These resulting spectra will later on serve as the reference for comparison for the respective period, when investigating the influence of the LIDAR corrections on data taken under sub-optimal atmospheric conditions.

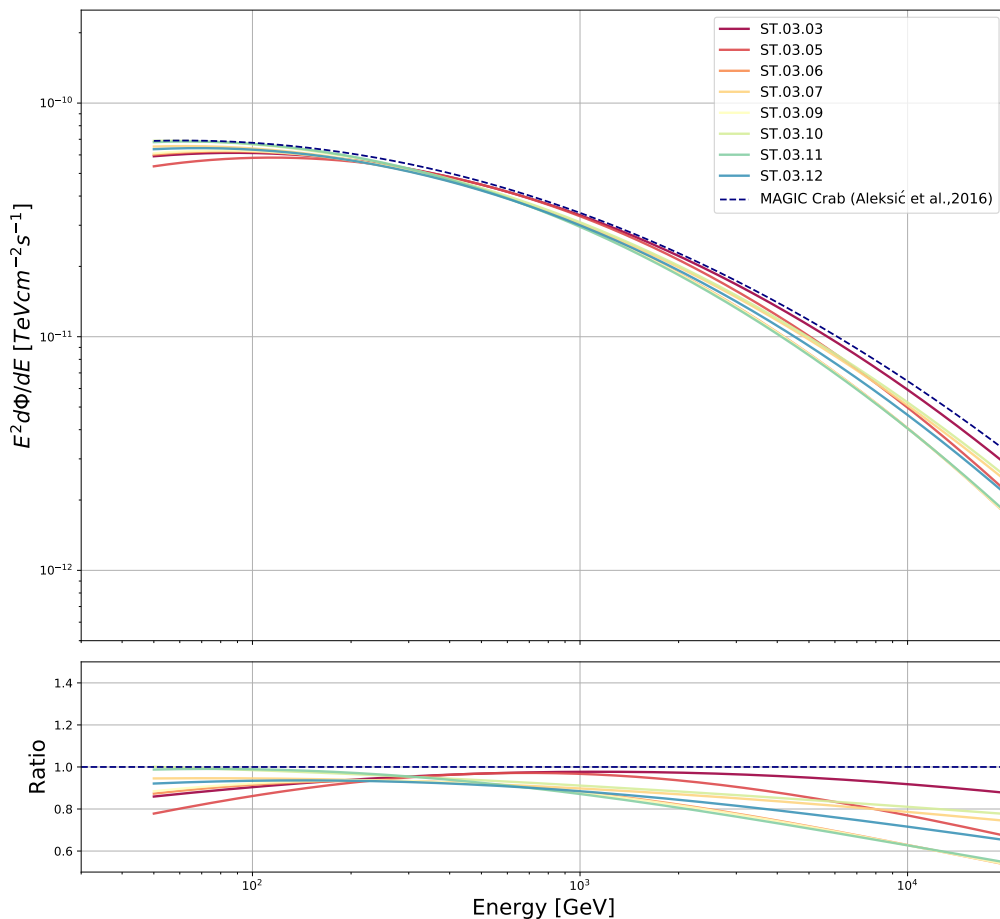


Figure 4.3: Top: Reference spectra of all included analysis periods with a spectrum published by MAGIC (Aleksić et al., 2016b) for comparison. Bottom: Ratio between the spectrum of a given analysis period and the published spectrum.

4.2 Evaluation of the current performance

4.2.1 Methodology

In order to investigate the influence of the LIDAR corrections under different gradations of atmospheric transmissions, the remaining data are further divided into three transmission bins according to their

transmission from 9 km, $T_{9\text{km}}$. A high transmission bin ranging from 0.85 until 0.93, a mid transmission bin from 0.7 until 0.85 and a low transmission bin from 0.55 until 0.7. Data with an associated transmission of below 0.55 cannot be adequately recovered anymore and is not included in the sample. Although data above 0.85 are generally considered usable without applying corrections, the high transmission bin is introduced to reevaluate this recommended threshold. For cutting data with an upper limit on transmission, the data selection program of MARS had to be modified, since upper transmission limits are not reasonable for regular MAGIC analyses. Table 4.2 shows the amount of available data in each segment and the number of nights over which the data are distributed over.

Table 4.2: Amount of used data for the given transmission bins.

| Transmission | Hours | Nights |
|--------------|-------|--------|
| 0.85 - 0.93 | 44.7 | 78 |
| 0.7 - 0.85 | 27.3 | 42 |
| 0.55 - 0.7 | 8.9 | 29 |

This part of the data set, which contains all Crab data with a transmission between 0.55 and 0.93, is analyzed and processed up to an energy spectrum in an analogous way as the reference spectra. As a lower energy threshold, a value of 100 GeV was set for this work. Since an impaired atmospheric transmission raises the energy threshold of IACTs, a rather conservative value was chosen to ensure the usage of data only taken above the adequate threshold.

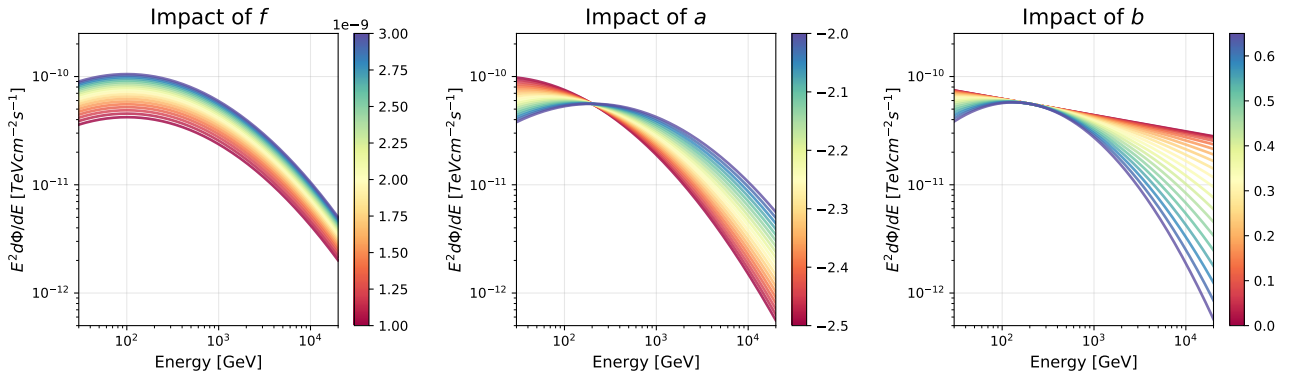


Figure 4.4: Influence of the spectral parameters to the log-parabola function.

In contrast to the analysis of the reference data described above, the data with $T_{9\text{km}}$ below 0.93 will not be fitted with a log-parabola function with three free variables, but with a fixed shape parameter, b . Figure 4.4 shows the impact on the function of varying each of the three parameters. The amplitude, f , scales the whole spectrum and will therefore be affected most by sub-optimal weather conditions. A change in the index parameter, a , results in a tilt of the spectrum. If the influence of the weather and the subsequent LIDAR corrections show a different behavior for lower and higher energies, it would show itself in this parameter. Lastly, the shape parameter, b , defines the curvature of the fitted spectrum and is most sensitive at high energies. The high energy region will therefore influence the shape parameter most, which will also affect the amplitude and index parameter via the correlation

matrix. Since statistics is most limited at this energy region, the shape parameter will be fixed to assist the fitting procedure, and avoid its influence on the other function parameters.

In the first part of the analysis, the data are processed and analyzed into spectra on a nightly basis. Meaning data taken under one observation night get combined into a single spectrum by using the forward unfolding method. The atmospheric conditions of an example night from November 13, 2015, are shown in figure 4.5. It shows the range corrected number of photoelectron counts for different timestamps marked by different color shadings (see explanations in section 3.2.2, as well as figure 3.4 and 3.5). The curves indicate a stronger scattering caused by aerosols above the ground up to an altitude of around 1.5 km. This is followed by a linear decrease of photon counts caused by the molecular scattering in a clear atmosphere to a height of around 8.5 km. The subsequent higher return signal until 11 km reveals the presence of a thick layer of clouds. As described previously, the photoelectron counts can be used to extract the integral transmissions for different heights, which is shown in figure 4.6. The aerosol layer at ground level causes a quick drop off until around 0.75 and the subsequent higher layer of cloud causes a further drop to as low as 0.4. This results in a transmission from 9 km of mostly around 0.75.

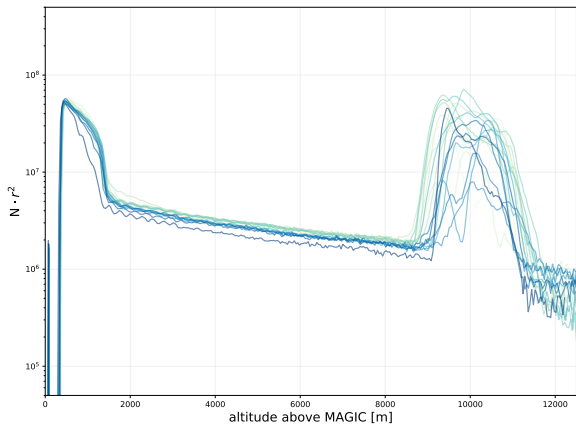


Figure 4.5: Range corrected photo-electron count on November 13, 2015, revealing a higher aerosol content above the ground up to around 1.5 km, as well as a layer of clouds between 8.5 km and 11 km above MAGIC.

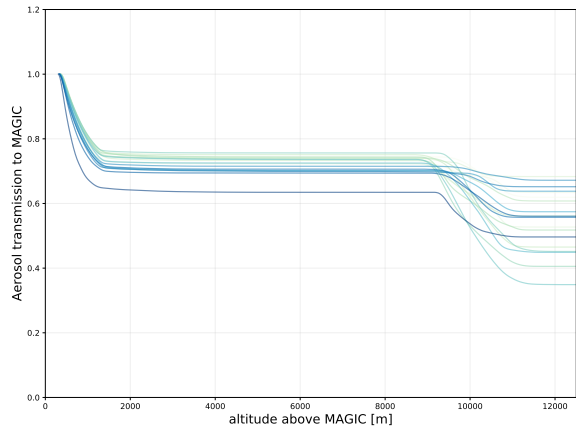


Figure 4.6: Integrated atmospheric transmission on November 13, 2015, indicating a transmission at 9 km of mostly around 0.75.

Figure 4.7 shows the resulting gamma-ray spectrum of the night. The image shows the reconstructed spectral fit and flux without applying LIDAR corrections in red and with the corrections in blue. The corresponding reference spectrum is given by the dashed spectrum in dark green. After applying corrections, an excellent agreement of the corrected spectrum with the reference can be seen.

In order to quantify the impact of the LIDAR corrections, the fitted spectral parameters and fluxes are compared to the corresponding reference spectrum. To further improve statistics, no individual flux points are compared, but instead the summed up flux for three energy bins. The bins cover the region from 100 GeV to 250 GeV (low energy), from 250 GeV to 1 TeV (medium energy) and above 1 TeV (high energy), which are also marked in figure 4.7.

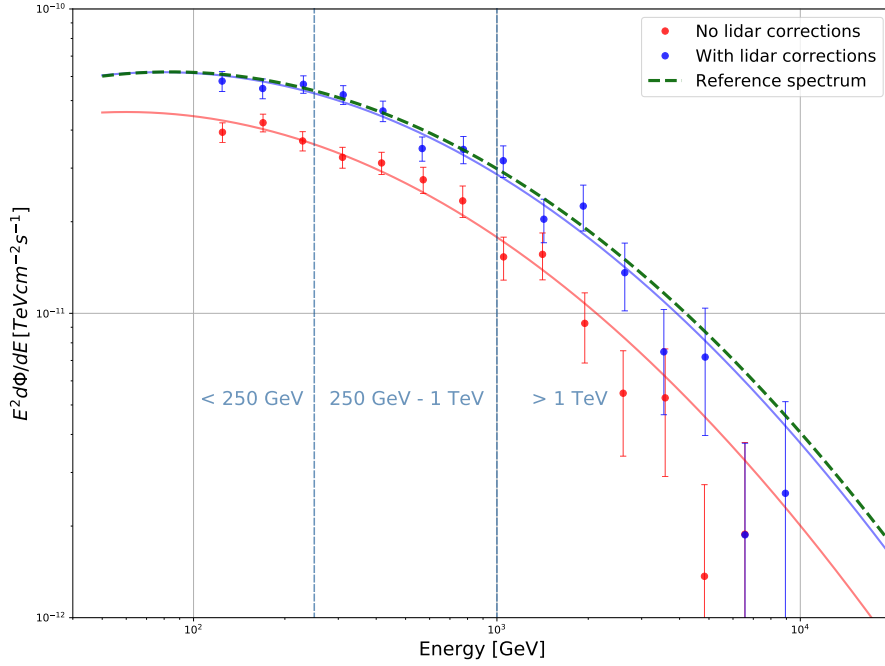


Figure 4.7: Example Crab Nebula spectrum, taken on November 13, 2015, showing the impact of the LIDAR corrections on data in the 0.7 to 0.85 transmission bin.

The comparison of the resulting parameters, p_i , and fluxes, f_i , is performed in two ways. First, the percental deviation from the expected value is determined, to get the relative deviation from the reference:

$$D_{p_i}[\%] = \left| \frac{p_i}{p_{ref}} - 1 \right| \cdot 100 \quad \text{and} \quad D_{f_i}[\%] = \left| \frac{f_i}{f_{ref}} - 1 \right| \cdot 100 \quad (4.2)$$

The uncertainty of a given deviation is then given by:

$$\Delta D_{p_i}[\%] = \frac{\Delta p_i}{p_{ref}} \cdot 100 \quad \text{and} \quad \text{analogous for } f_i \quad (4.3)$$

Second, to estimate the statistical significance of a given deviation, also the deviation in units of standard deviations is determined:

$$D_{p_i}[\sigma] = \left| \frac{p_i - p_{ref}}{\Delta p_i} \right| \quad \text{and} \quad \text{analogous for } f_i \quad (4.4)$$

Since the deviation is quantified in units of the uncertainty of the deviation, the error is already taken into account. The error hence is given by 1:

$$\Delta D_{p_i}[\sigma] = \left| \Delta p_i \cdot \frac{\partial D}{\partial p_i} \right| = \left| \Delta p_i \cdot \frac{1}{\Delta p_i} \cdot \frac{|p_i - p_{ref}|}{p_i - p_{ref}} \right| = 1 \quad \text{and} \quad \text{analogous for } f_i \quad (4.5)$$

Together, both quantities provide a reasonable quantification of how substantial a given quantity deviates from the expected value. A large percental deviation with a small statistical deviation can be attributed to low statistics, whereas a large statistical deviation with a low percental deviation might be caused by the intrinsic systematic uncertainties in the spectral analysis of of MAGIC data.

4.2.2 Evaluation of the LIDAR performance on a nightly basis

Flux deviations

First, I investigate deviations of the sum of the flux of all three energy bins before and after LIDAR corrections. As just described, both types of deviations, the statistical and percental, together provide a conclusive measurand for the severity of a given deviation. Before looking at nights with an impaired atmosphere, nights during clear atmospheric conditions ($T_{9\text{km}} > 0.93$) are inspected. In order to demonstrate how much the results from individual nights deviate from the average spectrum they create, the results are shown in the form of scatter plots and distributions. Figure 4.8 contains the statistical and percental deviations of the summed up fluxes compared to the reference flux. An individual scatter points represents the flux deviation of a single night and for one specific energy bin. To demonstrate the overall correction influence all three energy regions are shown simultaneously in the plot. The distribution of nights is projected onto two histograms on the side and top. The majority of nights show deviations below 2σ and 20%, respectively. The projected histograms roughly resemble Gaussian distributions with a standard deviation of around 1σ and 10%. These provide the best attainable results for the nights, that are impaired by the atmospheric conditions, and, hence, need LIDAR corrections.

Figure 4.9 shows the same type of plot, but for data from the three different atmospheric transmission bins with $T_{9\text{km}} < 0.93$. Now, the plots contain the distribution of nights with and without applying LIDAR corrections. The top plot shows the transmission region from 0.85 until 0.93. Due to the already relatively good atmospheric conditions, only slight improvements can be observed when applying the LIDAR corrections. This confirms $T_{9\text{km}} > 0.85$ can be considered as good atmospheric conditions, and, hence, LIDAR corrections are not really necessary. The most substantial improvements can be seen in the middle plot displaying nights during an atmospheric transmission of 0.7 until 0.85. Here, the average percental deviation improves from around 25% down to 15%. On the significance side, an enhancement from around 2σ down to 1σ can be seen. There are only very few outliers with statistical deviations above 3σ . The vast majority of all nightly spectra get sufficiently well restored by applying the LIDAR corrections. In the lower plot, the impact on data taken under the lowest transmission ($0.55 < T_{9\text{km}} < 0.7$) is shown. Due to the scarcity of data in this domain, the projected histograms are relatively noisy, but nevertheless show a clear trend of significant improvement. The percental deviation shows an improvement from around

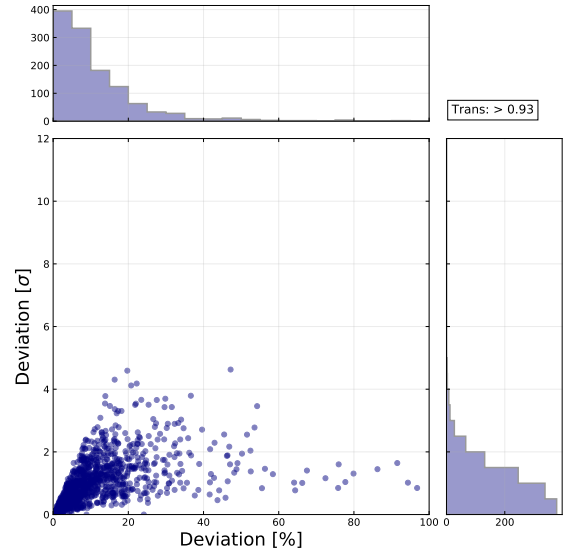


Figure 4.8: Scatter plot and distribution of the percental and statistical flux deviation of individual nights from the reference data to the reference spectrum.

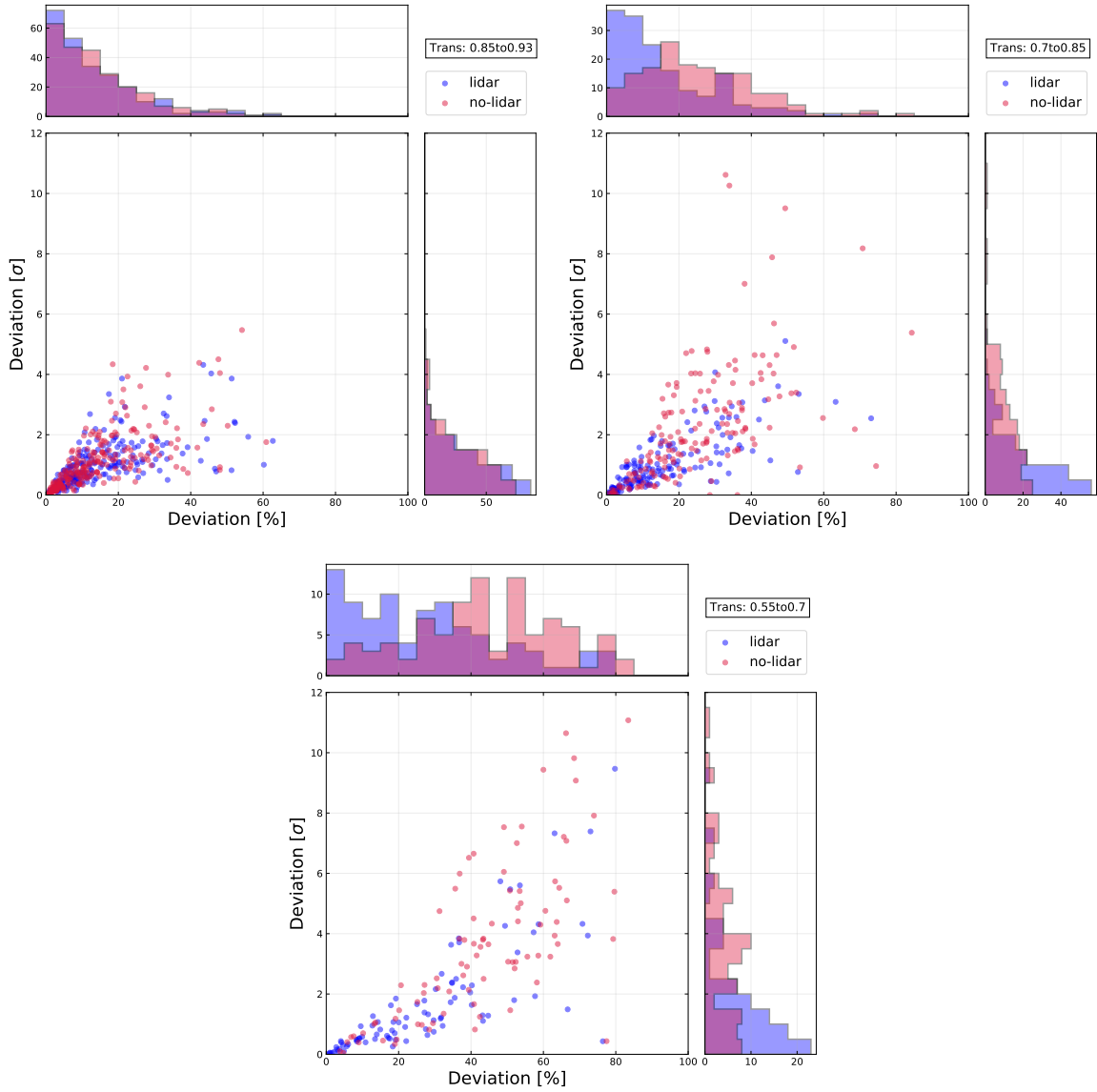


Figure 4.9: Scatter plot and distribution of the percental and statistical flux deviation from the reference spectrum of individual nights. Top left: $0.85 < T_{9\text{km}} < 0.93$, Top right: $0.7 < T_{9\text{km}} < 0.85$, Bottom: $0.55 < T_{9\text{km}} < 0.7$.

50% on average down to around 30%. For the statistical deviation, the mean improves from around 4σ down to below 2σ . Despite the impactful improvements, there are still several incidents, where the deviation is severe, even after applying LIDAR corrections. Around a third of all nights still show deviations above 2σ after corrections, indicating that the LIDAR is not able to sufficiently well reconstruct all spectra in this transmission region.

In order to investigate the influence of different zenith angles, under which the data were taken, the data are further classified into three zenith bins. A low zenith bin from 5° to 35° , a mid zenith bin from 35° to 50° and a high zenith bin from 50° to 62° . The correction effects are now also investigated separately for the three previously introduced energy regions. Instead of depicting deviations from individual nights, the information is now further condensed by taking the mean value of all deviations

in a given parameter realm. This corresponds to the shift of the histogram mean discussed earlier, and allows an isolation of the correction effect for different transmission, zenith and energy regions. In order to account for the statistics of individual night, an error-weighted mean is used for the percental deviation:

$$\bar{D}_f[\%] = \frac{\sum_{i=0}^n w_i \cdot D_{f_i}}{\sum_{i=0}^n w_i} \quad \text{where} \quad w_i = \frac{1}{\Delta D_{f_i}^2} \quad (4.6)$$

The error of the mean is then given by:

$$\Delta \bar{D}_f[\%] = \sqrt{\frac{1}{\sum_{i=0}^n w_i}} \quad (4.7)$$

For averaging the statistical deviation, a standard mean is taken, since the statistical significance is already taken into account:

$$\bar{D}_f[\sigma] = \frac{1}{n} \sum_{i=0}^n D_{f_i} \quad (4.8)$$

The error is given by the standard error of the mean, where σ' describes the standard deviation of the deviations around the mean:

$$\Delta \bar{D}_f[\sigma] = \frac{\sigma'}{\sqrt{n}} \quad (4.9)$$

First, the mean deviations of the nights used for the reference spectra are inspected. Figure 4.10 shows the mean statistical and percental deviation of the flux below 250 GeV for the first two zenith bins. For the highest zenith bin, the energy threshold of MAGIC is above 250 GeV and, hence, the flux above 250 GeV cannot be computed reliably. The percental deviation goes from around 7% for low zeniths up to around 12% for medium zeniths. The results for the energy range below 250 GeV for the data impaired by atmospheric conditions are displayed in figure 4.11. A three by three arrangement covers all combinations of zenith angle and atmospheric transmission bins. An individual plot contains the mean percental and statistical deviation before and after applying LIDAR corrections. The dotted bars indicate the mean values obtained from nights with $T_{9\text{km}} > 0.93$ shown in figure 4.10, to provide the best achievable benchmark. The plots confirm the previously discussed improvements for the three transmission bins. Above a transmission of 0.85, the spectra are reconstructed fully on average, but also show no significant offset without applying LIDAR corrections. For high zeniths, there is again no data available, due to the increase in the energy threshold at high zeniths. The values for the transmission between 0.7 to 0.85, indicate an adequate reconstruction for the low zeniths. For zeniths above 35° , the percental deviation is still almost 10% above the benchmark. Hence, the spectrum is still marginally impaired by systematic uncertainties originating from the atmospheric conditions. For the low transmission, an improvement by almost 20% and 2σ respectively can be seen. The bars still show a significant excess above the benchmark indicating, that on average the LIDAR is not able to reconstruct the spectra sufficiently well for transmission below 0.7.

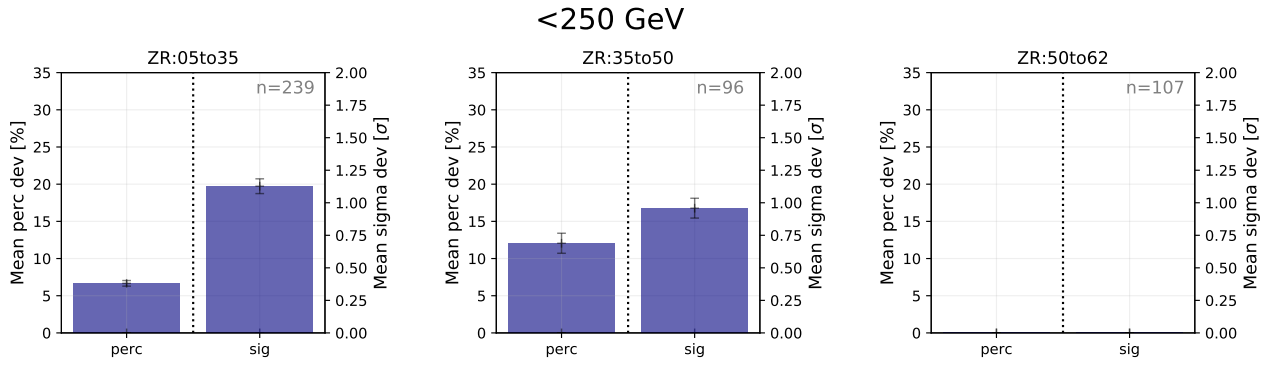


Figure 4.10: Mean percental (perc) and statistical (sig) deviation of the flux of the reference data below 250 GeV from the reference spectrum for three zenith bins. Due to the high energy threshold above a zenith angle of 50° , the right plot does not contain data. The number of averaged nights is given in the top right corners.

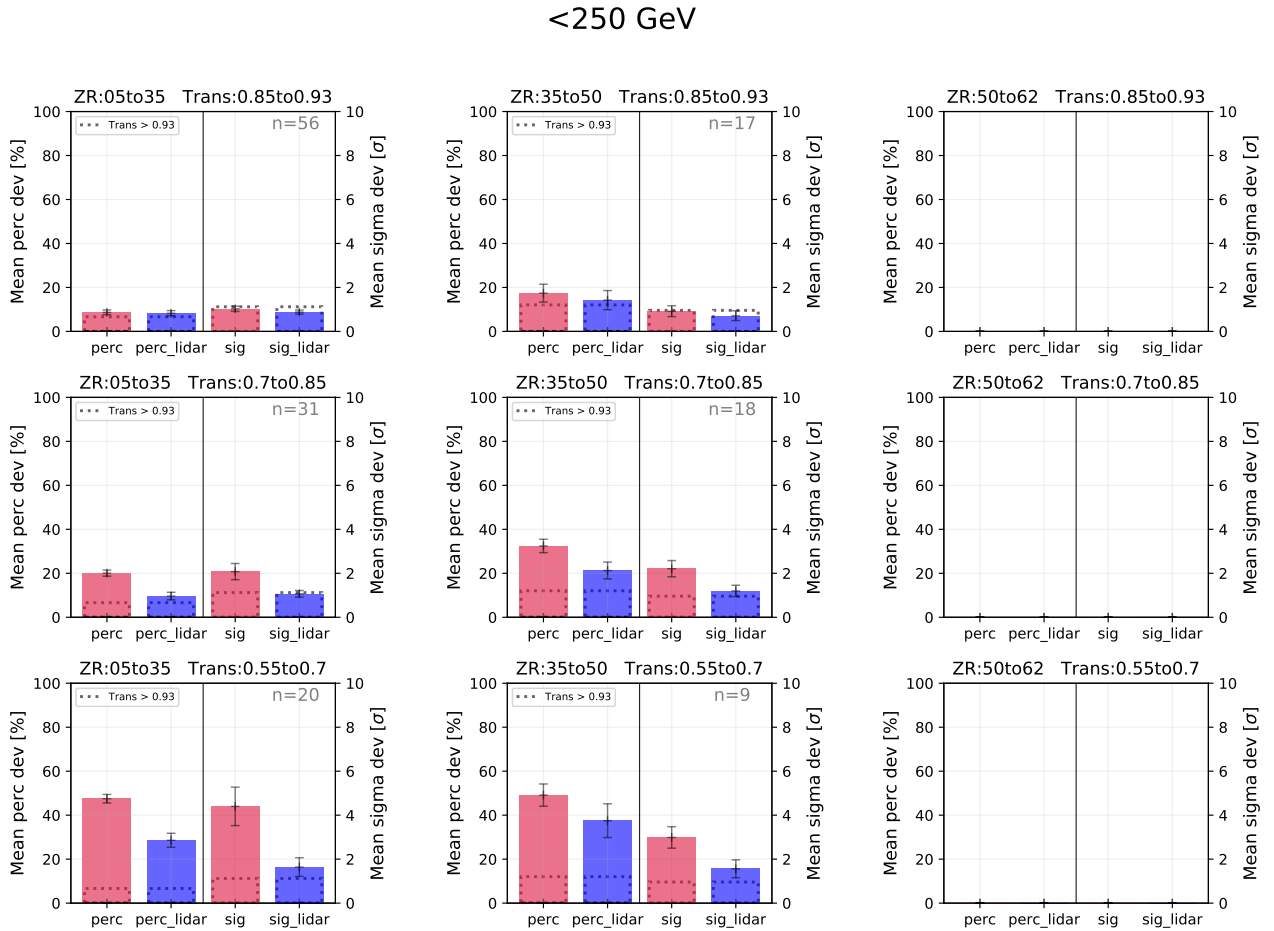


Figure 4.11: Mean percental (perc) and statistical (sig) deviation of the flux below 250 GeV from the reference spectrum without (red) and with (blue) LIDAR corrections for nine zenith and transmission bin combinations. Due to the high energy threshold above a zenith angle of 50° , the right plots do not contain data. The number of averaged nights is given in the top right corners. Benchmark values obtained from the reference data set is given by the dashed black bars.

Figure 4.12 shows both mean deviations of the reference nights for the medium energy range from 250 GeV to 1 TeV. Here, the percental mean is around 7% for the low and medium zeniths but around 13% for the highest zenith bin. The results of the corrected data obtained for the medium energy range are shown in figure 4.13. One can see a similar pattern as in the low energy bin (see figure 4.11). The results for a transmission of 0.85 again show fully reconstructed spectra, but also show very little offset without applying LIDAR corrections. For the transmission between 0.7 and 0.85, the corrections work well for the data taken under a zenith below 35° and above 50° . For medium zeniths, some very slight offset is still present. The low transmission region again shows an improvement by around 10%-20% and 2σ , respectively, with some remaining deviation from the benchmark. The region above 50° only depicts a minimal improvement on the percental deviation of about 5% and on the statistical deviation from 7σ down to 5σ . However, the low number of available nights causes a considerable uncertainty on the result.

Lastly, figure 4.14 shows the results obtained for the reference data above 1 TeV. The percental means are now close to 10% for all zeniths. The results for the energy bin above 1 TeV obtained with data with $T_{9\text{km}} < 0.93$ are portrayed in figure 4.15. The mean deviations of the fluxes show a very similar pattern to the medium energy range (figure 4.13). For the lowest transmission at the highest zenith, there is not sufficient data to produce a robust result.

Overall, the corrections work very well and reduce the systematic uncertainties caused by atmospheric conditions for all energy and zenith regions. In the analyzed data set, there is no clear difference and trend between different energy regions. Hence, the results of this study do not suggest, that there is a different impact from sub-optimal atmospheric conditions on the investigated energy regions of the reconstructed spectra. As previously mentioned, an energy threshold of 100 GeV was used in this work. A stronger energy dependence might show itself if one goes to even lower energies. Poor atmospheric conditions can decrease the trigger efficiency of IACTs, as described previously. This effect is expected to be strongest for low energies, where the light yield of air showers is the weakest. However, this expected behavior could not be observed with the given data sample and chosen threshold, confirming that the threshold of 100 GeV is appropriate when analyzing atmospherically impaired data.

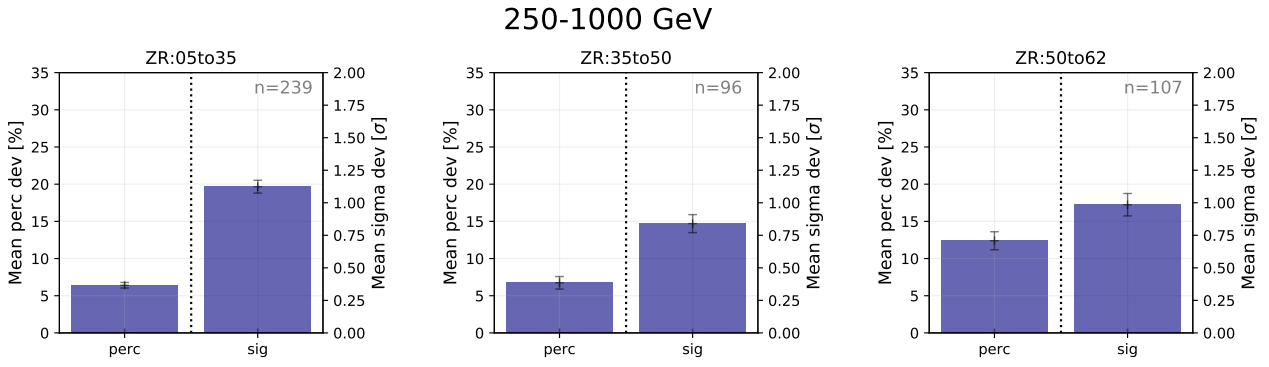


Figure 4.12: Same as figure 4.10, but for the energy region between 250 GeV and 1 TeV.

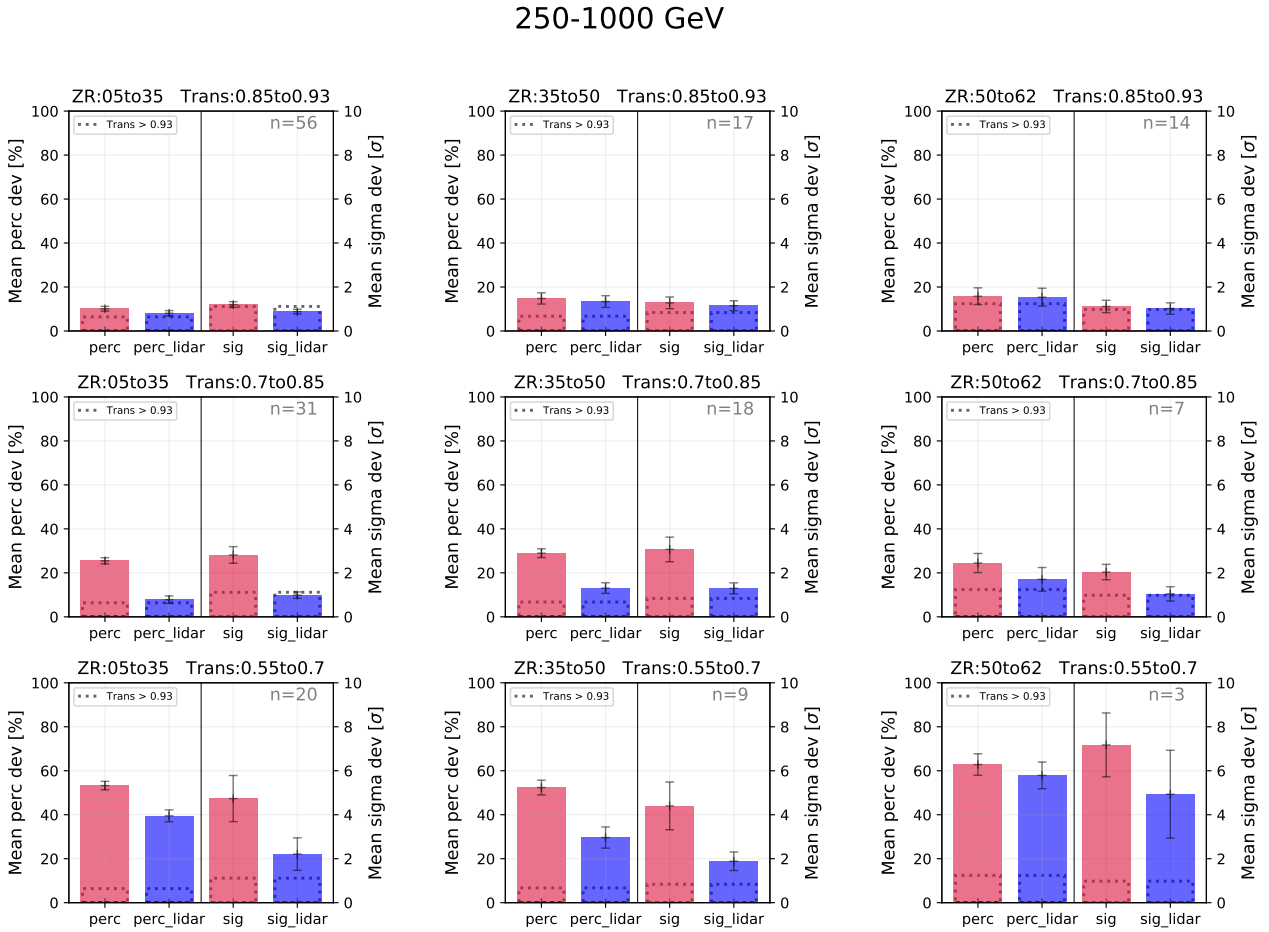


Figure 4.13: Same as figure 4.11, but for the energy region between 250 GeV and 1 TeV.

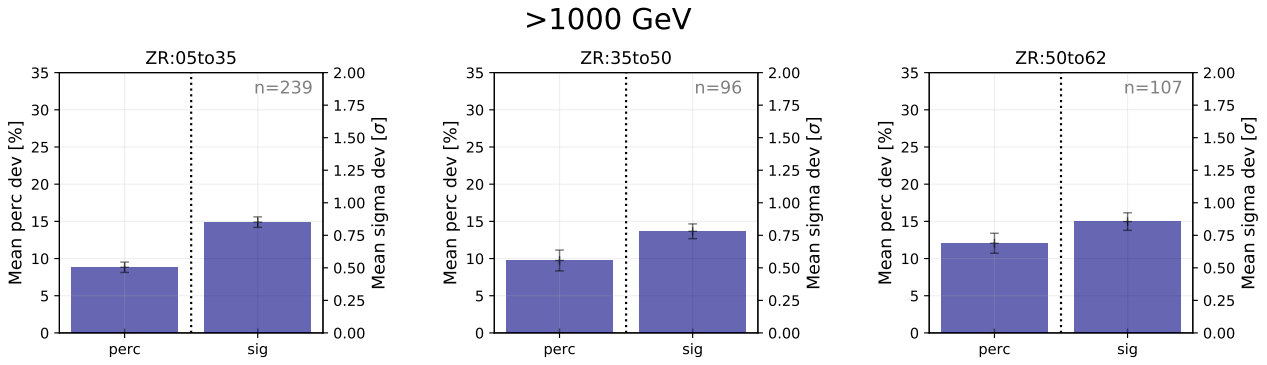


Figure 4.14: Same as figure 4.10, but for the energy region above 1 TeV.

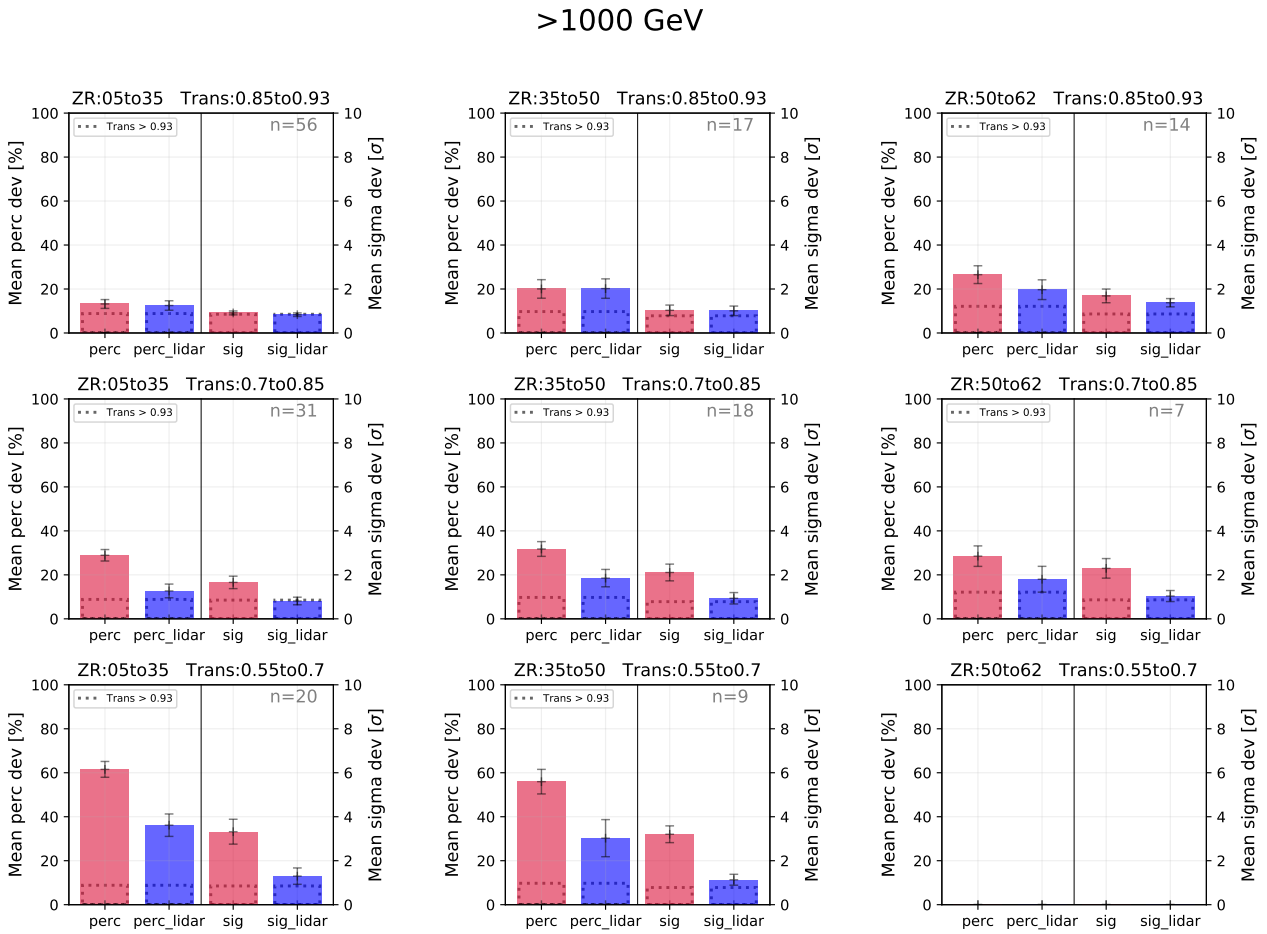


Figure 4.15: Same as figure 4.11, but for the energy region above 1 TeV. In the low transmission under high zenith bin, there is not sufficient data to produce a robust result.

Parameter deviations

In this section, I investigate the impact in the overall spectral shape of the Crab Nebula which is quantified by the parameters of the log-parabola fits. The results are again portrayed in the form of scatter plots showing the deviations from the aspired reference values for individual nights. Figure 4.16 shows the scatter plot and distributions for the reference spectra, as before with the flux deviations. The projected histograms of both plots can again be roughly described by Gaussian distributions. For the amplitude parameter, f , (left plot), the mean deviation of the percental deviation lies at around 10% and for the statistical deviation a bit over 1σ . For the index parameter, a , the distribution is much less spread out. The absolute majority of nights show deviations of below 5% with a mean statistical deviation of around 1σ . This again provides the best achievable standard for the nights with $T_{9\text{km}} < 0.93$, and, hence, require LIDAR corrections.

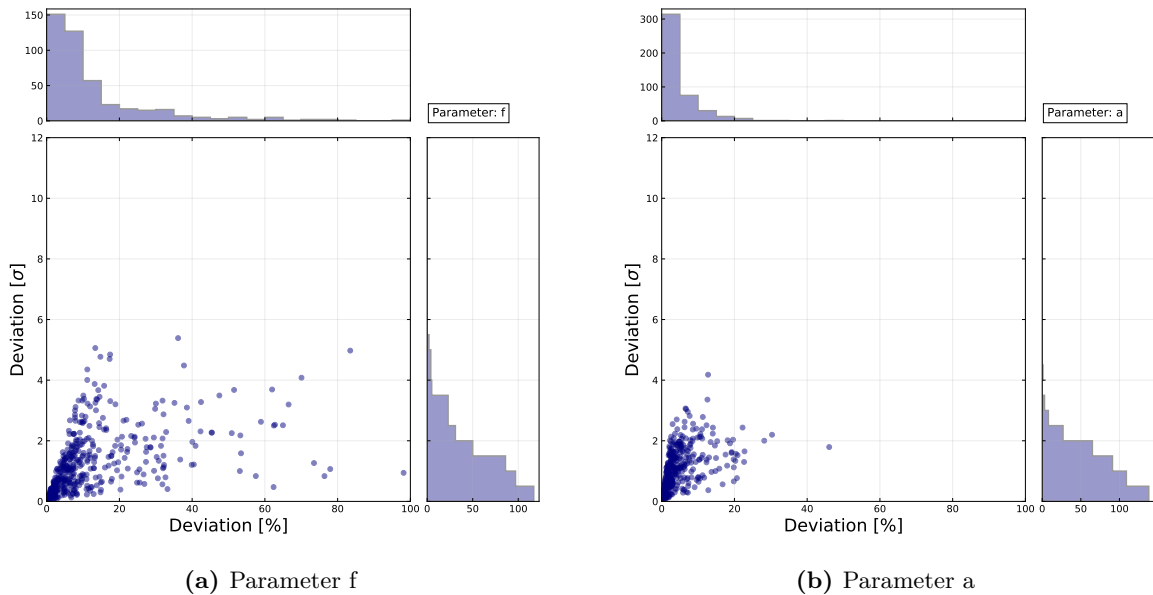


Figure 4.16: Scatter plot and distribution of the percental and statistical parameter deviation from the reference spectrum of individual nights from the reference data.

Figure 4.17 contains the results for both the amplitude and index parameter of the nights with $T_{9\text{km}} < 0.93$. In the left plot, the distribution of deviations of individual nights for the amplitude is presented. The histogram of the percental as well as of the statistical deviations shows a clear shift towards lower values. Also the number of strong outliers with statistical deviations above 3σ is reduced very profoundly. Due to the LIDAR corrections, the majority of extreme outliers are corrected into a more reasonable range. In the right plot, the same diagram for the index parameter is shown. The histograms show no significant improvements after applying LIDAR corrections. However, both distributions contain the majority of nights already at deviations of below 5% and with a mean statistical deviation of around 1σ , similar to the reference nights shown in the right plot of figure 4.16. Hence, they do not require a correction in the first place. Sub-optimal atmospheric conditions do not seem to significantly distort the spectral tilt.

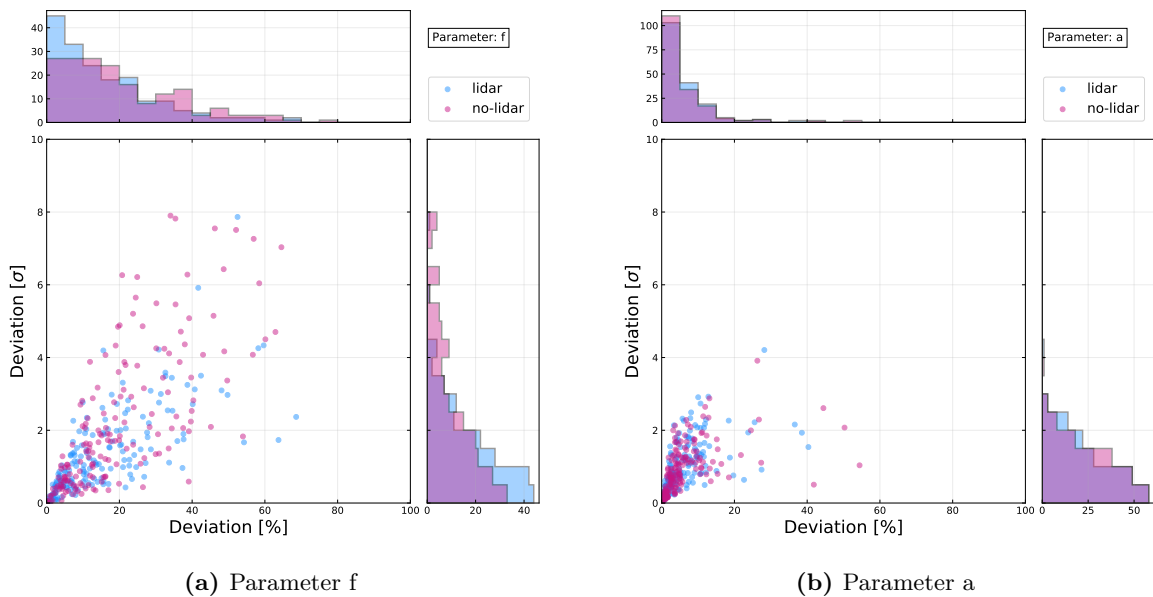


Figure 4.17: Scatter plot and distribution of the percental and statistical parameter deviation from the reference spectrum of individual nights.

Analogous to before, the mean values over all incorporated nights are now taken after further classifying the data in terms of their zenith angle and atmospheric transmission. The fit results of the amplitude parameter of the reference data are portrayed in figure 4.18. It shows a percental deviation rising from 5% for low zeniths, to around 10% for mid zeniths until almost 24% at the highest energies, indicating that an accurate fit becomes more and more challenging at higher zeniths. Figure 4.19 then depicts the results for the amplitude parameter of the corrected data. Again, the effect is investigated for nine different zenith and transmission combinations. In almost all cases with a transmission from 0.7 to 0.85 and 0.85 to 0.93, the amplitude parameter is reconstructed well, as illustrated by the reasonably good agreement with the benchmark values. For the lowest transmission bin, an improvement in the percental deviation from around 50% down to 30% can be seen for a zenith up to 50° . For the highest zenith range, the data do not allow for a meaningful statement due to the low number of available nights. Hence, the data is not fully reconstructed in the mean for low transmissions. However, a strong correction is achieved, which can still enable the usage of the data, but with an increased systematic uncertainty compared to ideal conditions.

The benchmark averages for the index parameter provided by the reference data are illustrated in figure 4.20. It shows a very low average deviation of around 5% on average. In figure 4.21, the mean deviations of a with and without applying corrections are displayed. Overall, there are no significant differences between the mean deviations of the data with and without LIDAR corrections. Both cases are compatible with the benchmark in all zeniths and transmission regions, indicating that sub-optimal atmospheric conditions do not cause a detectable tilt in the spectrum, but only impair the spectral amplitude. Since no spectral tilt towards higher or lower energies could be observed, the results also support the previously asserted energy independence of atmospheric influence.

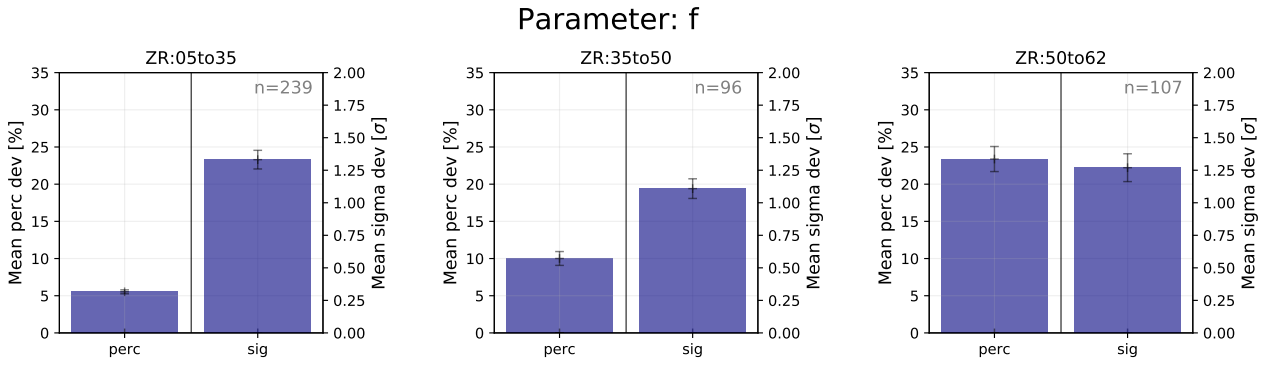


Figure 4.18: Mean percental and statistical deviation of the amplitude parameter, f , for the reference data. The number of averaged nights is given in the top right corners.

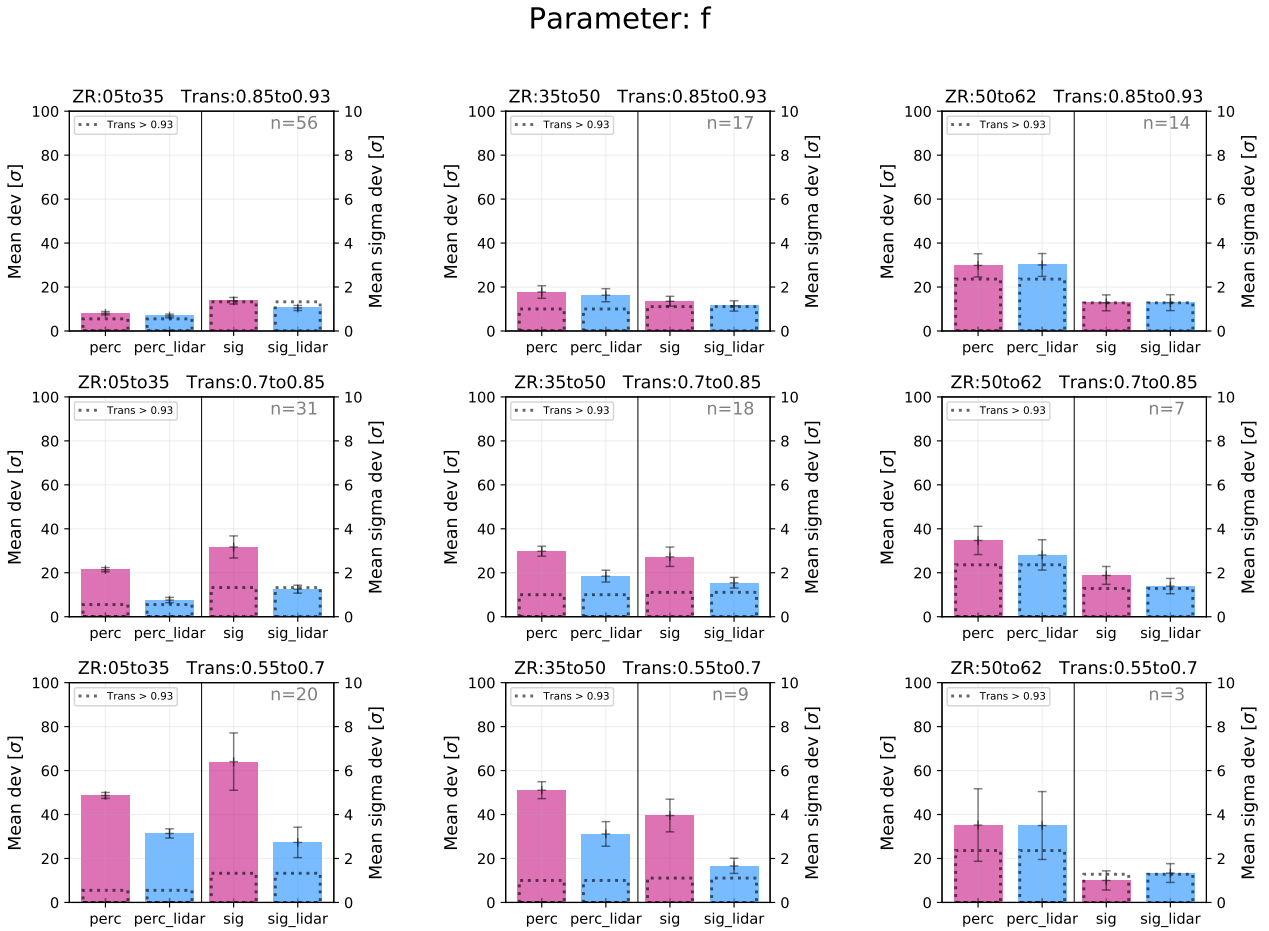


Figure 4.19: Mean percental and statistical deviation of the amplitude parameter, f , without (red) and with (blue) LIDAR corrections. The number of averaged nights is given in the top right corners. Benchmark values obtained from the reference data set is given by the dashed black bars.

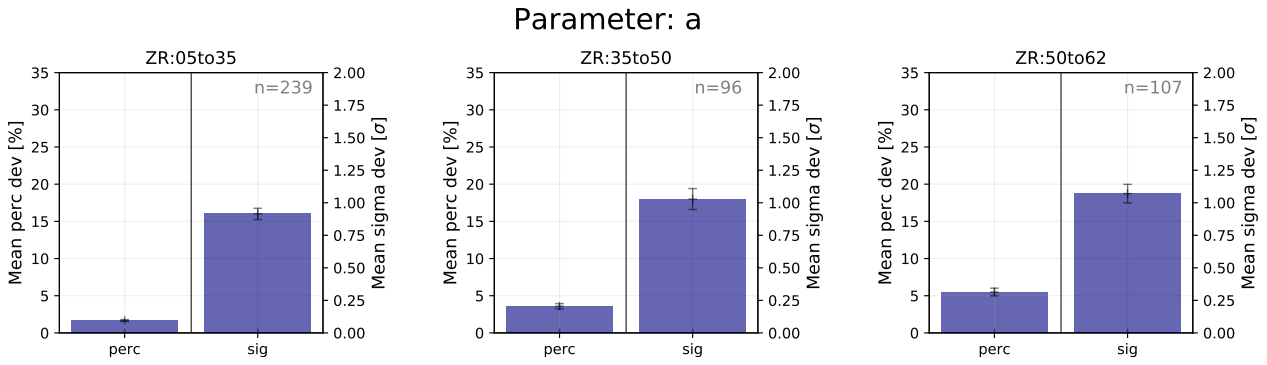


Figure 4.20: Mean percental and statistical deviation of the index parameter, a , for the reference data. The number of averaged nights is given in the top right corners.

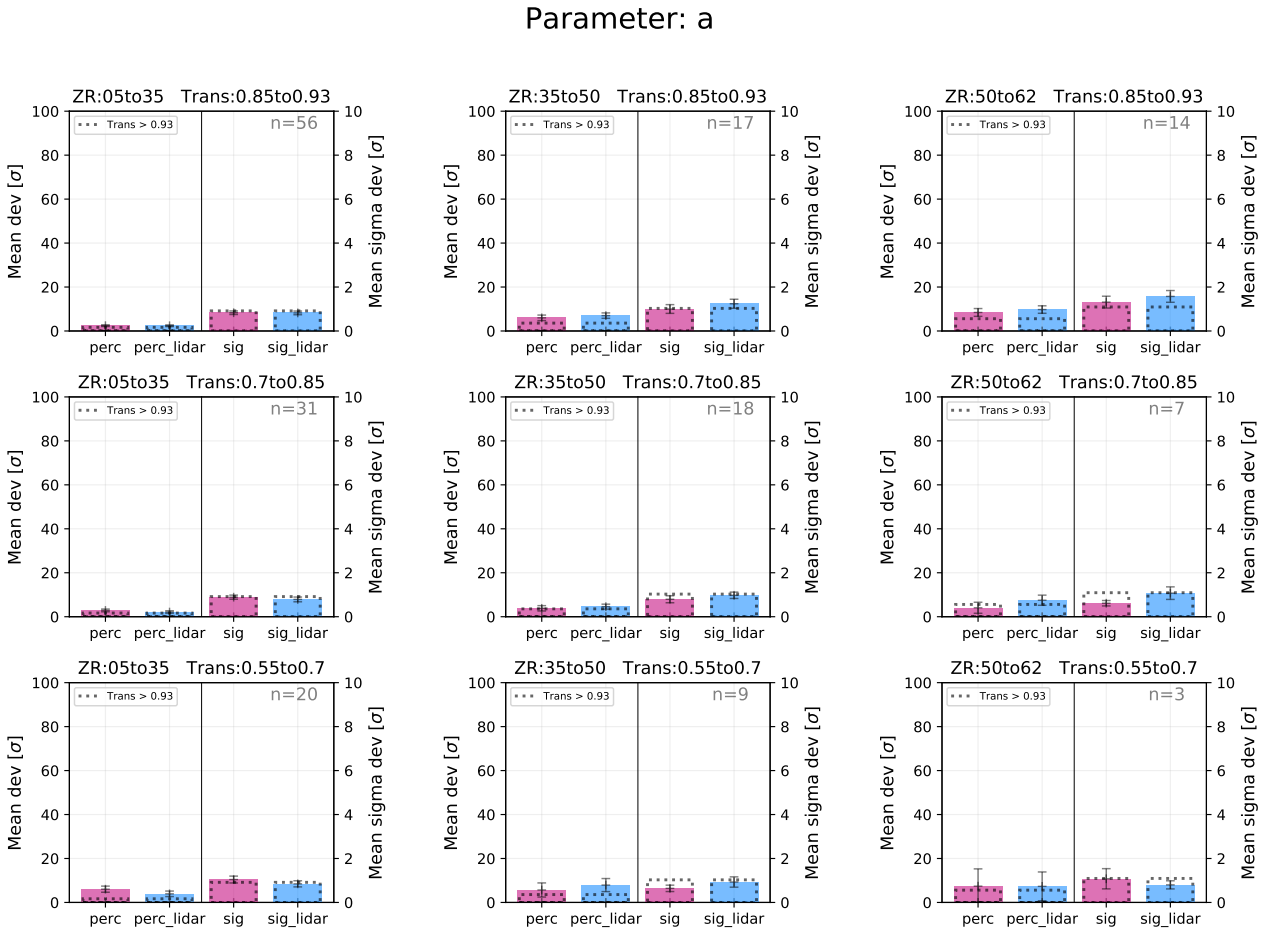


Figure 4.21: Mean percental and statistical deviation of the index parameter, a , without (red) and with (blue) LIDAR corrections. The number of averaged nights is given in the top right corners. Benchmark values obtained from the reference data set is given by the dashed black bars.

Overall, the results from both the flux and parameter deviations yield very similar statements about the effectiveness of the spectral corrections provided by the LIDAR. Data with an atmospheric transmission between 0.55 and 0.7, can be restored in some cases, but on average is not adequately reconstructed. Between 0.7 and 0.85, the reconstruction works exceptionally well for zenith angles below 35° . For higher zeniths, there can still be slight discrepancies to the ideal benchmark, which, however, remain below 10%. For the highest transmission bin from 0.85 to 0.93, LIDAR corrections are not absolutely necessary to use the data.

4.2.3 Period-averaged results

So far, results reported referred to single-night spectra. Only after the reconstruction, individual spectra were evaluated together to draw overall conclusions. As a second approach, data spanning over several nights and different analysis periods is combined into single spectra per zenith angle and transmission bin. This strategy leads to nine spectra with the smallest statistical uncertainties in the given parameter region. Figure 4.22 shows all nine spectra with and without the LIDAR corrections in blue and red, respectively. The effective observation time of the used data is given in the top right corner of the individual plots. The reference spectrum here is obtained by combining all the data used for the respective period-wise references into a single spectrum. This period-averaged reference spectrum also provides the shape parameter, which is then fixed for all the spectral fits. The combination of data across several analysis periods entails the downside of increasing systematics due to the already discussed varying MC-data match for different periods. However, it allows for the construction of spectra with much better statistics. Figure 4.23 shows the same results but in terms of the relative difference to the reference spectrum. In this way, discrepancies of the flux points as well as the different amplitude and tilt of the spectra become more apparent.

Already on first sight, the results from the combined spectral analysis support the previously drawn conclusions. For the low transmission regions, there is strong improvement present but also still a considerable remaining offset to the aspired reference spectrum. Above 0.7, the corrected spectra agree well with the reference. There is some discrepancy for lowest energies at the highest zenith angles. This is expected because there is no data available to constrain the fit in the lowest energy region due to the increased energy threshold.

In order to achieve a more number-based evaluation of the correction performance, the resulting fitted functions are now compared quantitatively to the reference value. Figure 4.24 shows the reconstruction accuracy of the spectral fit with and without the LIDAR corrections. It contains the percental deviation of the amplitude parameter from the reference to illustrate the overall scaling difference. Additionally, the integral over the curve in three energy regions is taken and compared to the reference to investigate the matching of the fit for difference energies. The energy bins considered range from 100 GeV to 250 GeV, 250 GeV to 1 TeV and 1 TeV to 10 TeV. Starting in the top left corner, the results for high transmissions ($0.85 < T_{9\text{km}} < 0.93$) are shown. The results also confirm the previously drawn conclusions. The spectrum can already be considered as adequately reconstructed at zeniths below 35° before applying corrections. Nevertheless, the LIDAR corrections still improves the agreement of the spectrum by a few percent. In the medium zenith region, the spectrum after corrections deviates around 10% for the amplitude and low energies and then decreases for higher energies. Finally,

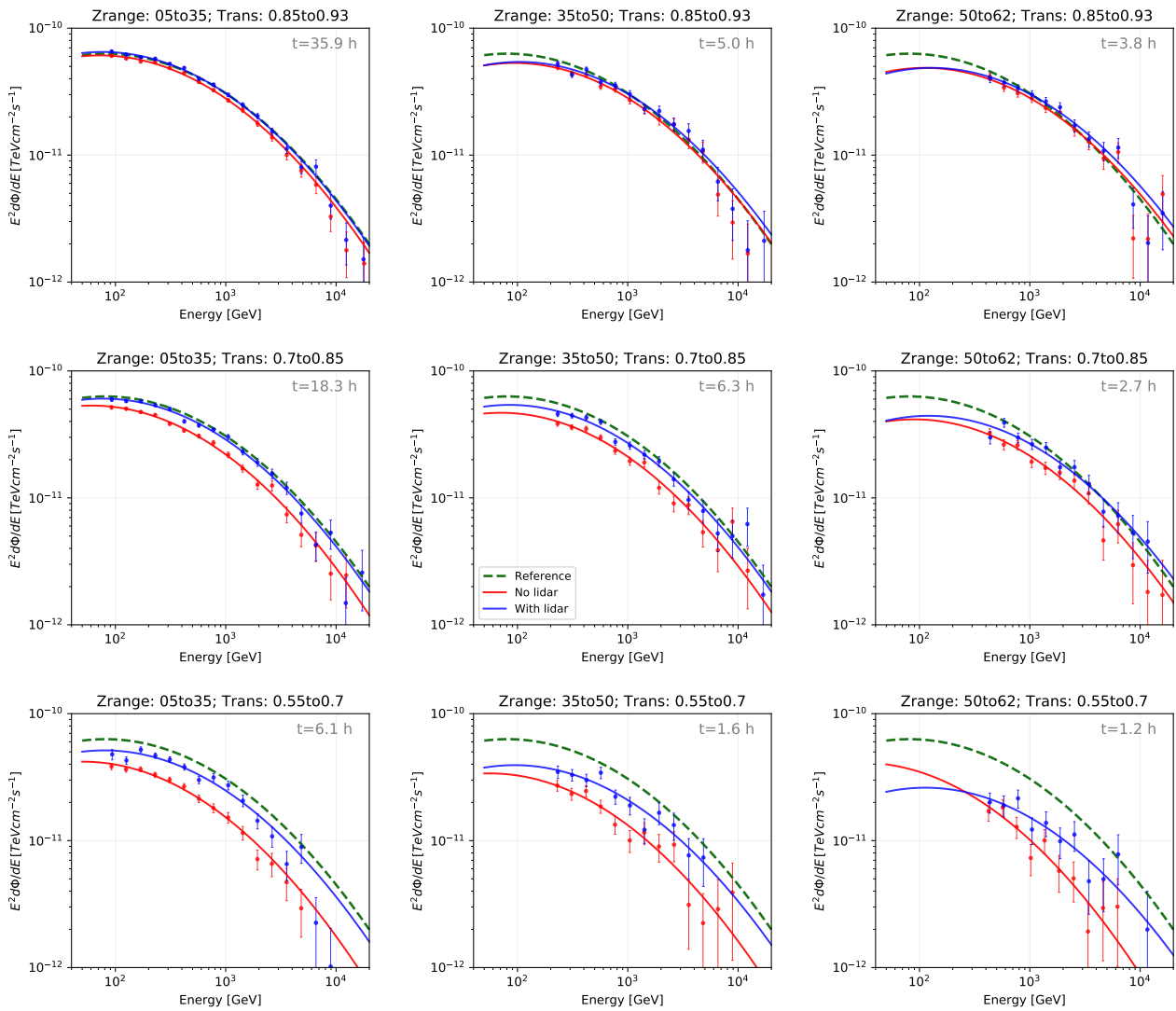


Figure 4.22: Spectra from the Crab Nebula derived with period-averaged data for nine different zenith angle and atmospheric transmission bins without (red) and with (blue) LIDAR corrections. The reference spectrum is shown as the dark green dashed line. The effective time of the data used for the individual spectra is given in the top right corner of each subplot.

the results for high zeniths and high transmission is shown in the top right. The spectrum shows relatively good agreement in the regions above 250 GeV, where the data have constraining power. For the highest energies, the deviations after correcting range between 10% and 20%. The exceptionally low deviation by the uncorrected data between 1 TeV and 10 TeV is the result of the binning choice. As can be seen in figure 4.23, the spectrum first undershoots and then overshoots the reference. In the resulting integral over the complete bin, however, these two effects roughly cancel out and it matches to the reference flux, despite a not entirely accurate spectral tilt. Going back to low zeniths but to a transmission of 0.7 to 0.85, the LIDAR is able to substantially improve the reconstructed spectra. Before corrections, there is a deviation of 20% for the amplitude and lower energies, which reaches values above 30% for high energies. Due to the LIDAR corrections, the new spectrum now shows deviations below 10% in all domains. Since, as mentioned previously, MAGIC estimates its intrinsic

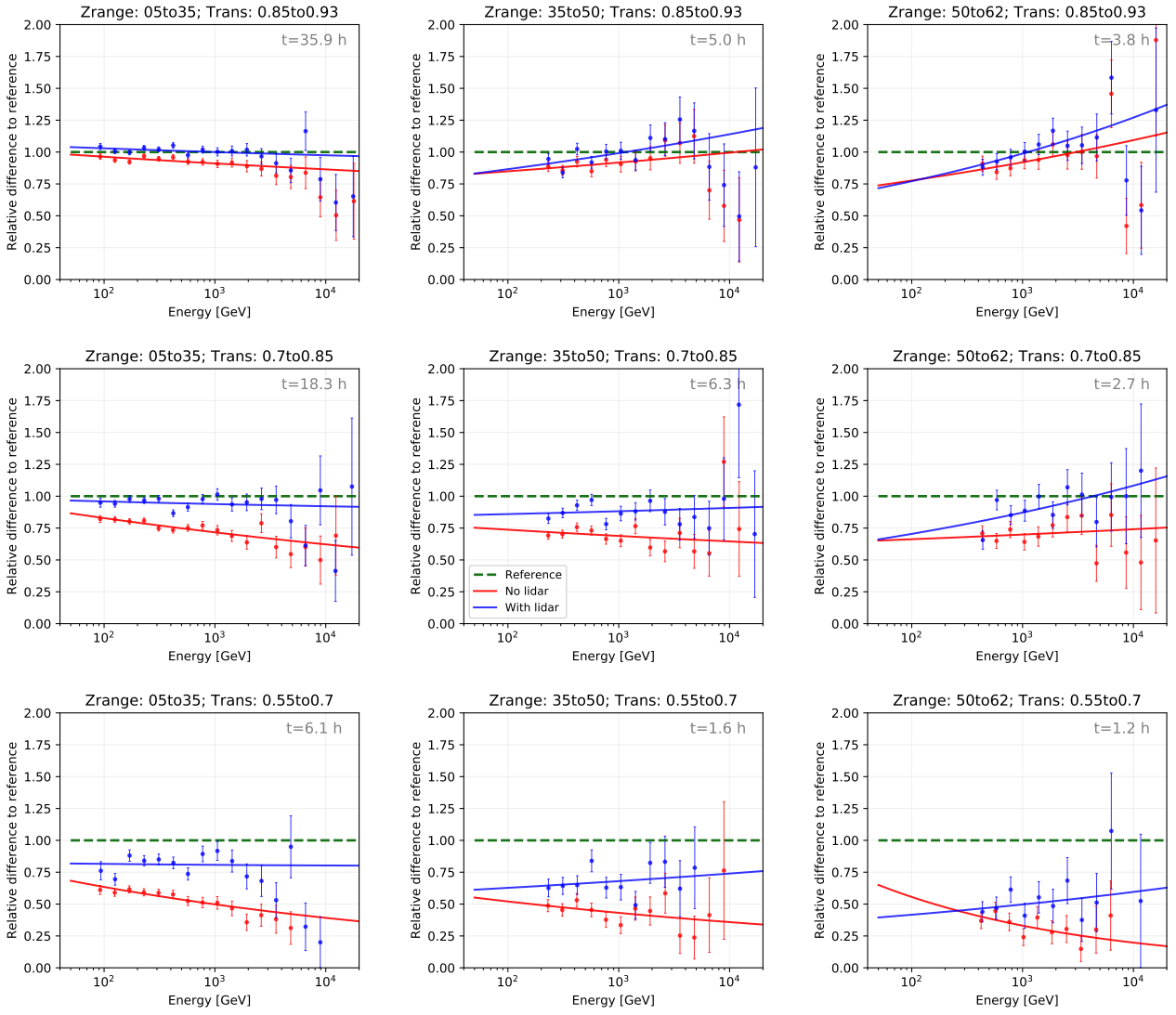


Figure 4.23: Relative difference of the period-averaged spectral fits to the reference for nine different zenith angle and atmospheric transmission bins without (red) and with (blue) LIDAR corrections. The effective time of the data used for the individual spectra is given in the top right corner of each subplot.

systematic uncertainty on the energy reconstruction to be below 15% and on the flux normalization to be around 11%-18% (Aleksić et al., 2016b). The spectrum can, therefore, be considered as fully recovered. For the medium zenith bin, pre-correction deviations are around 30% and get then corrected down to 15% on average. The spectrum is therefore very close to a full recovery, but still shows a slight discrepancy, which is a bit stronger for low energies. For energies above 1 TeV, the deviation goes down to 10%, which corresponds to an adequate agreement as just discussed. For highest zeniths, the amplitude, the low and the medium energy region, all show deviations above 15% after applying corrections, indicating an insufficient reconstruction. The spectrum shows a very precise agreement above 1 TeV. This is partly due to the same effect as before, where the choice of the binning interval causes a cancellation of a slight under- and overshooting. Due to the high energy threshold at around 400 GeV for high zeniths, the data are also constraining the fit best above 1 TeV and the low energy

region can be neglected. In the bottom left plot, the results for low transmission and low zeniths are shown. The LIDAR is able to bring deviations above 40% in all domains down to around 20%. For higher energies, the fit even improves from around 55% down to 20%. Going to higher zeniths from 35° to 50° , the deviations without LIDAR are between 50% and 60%. After corrections they range from around 30% to 45%. Hence, clear improvement can be seen but an adequate reconstruction is not reached. For the highest zenith bin, only 1.2 h of data are available in total, which results in two relatively noisy spectra. Some improvement in the energies above 250 GeV is there, but the statistics of the data are not sufficient to draw meaningful conclusions.

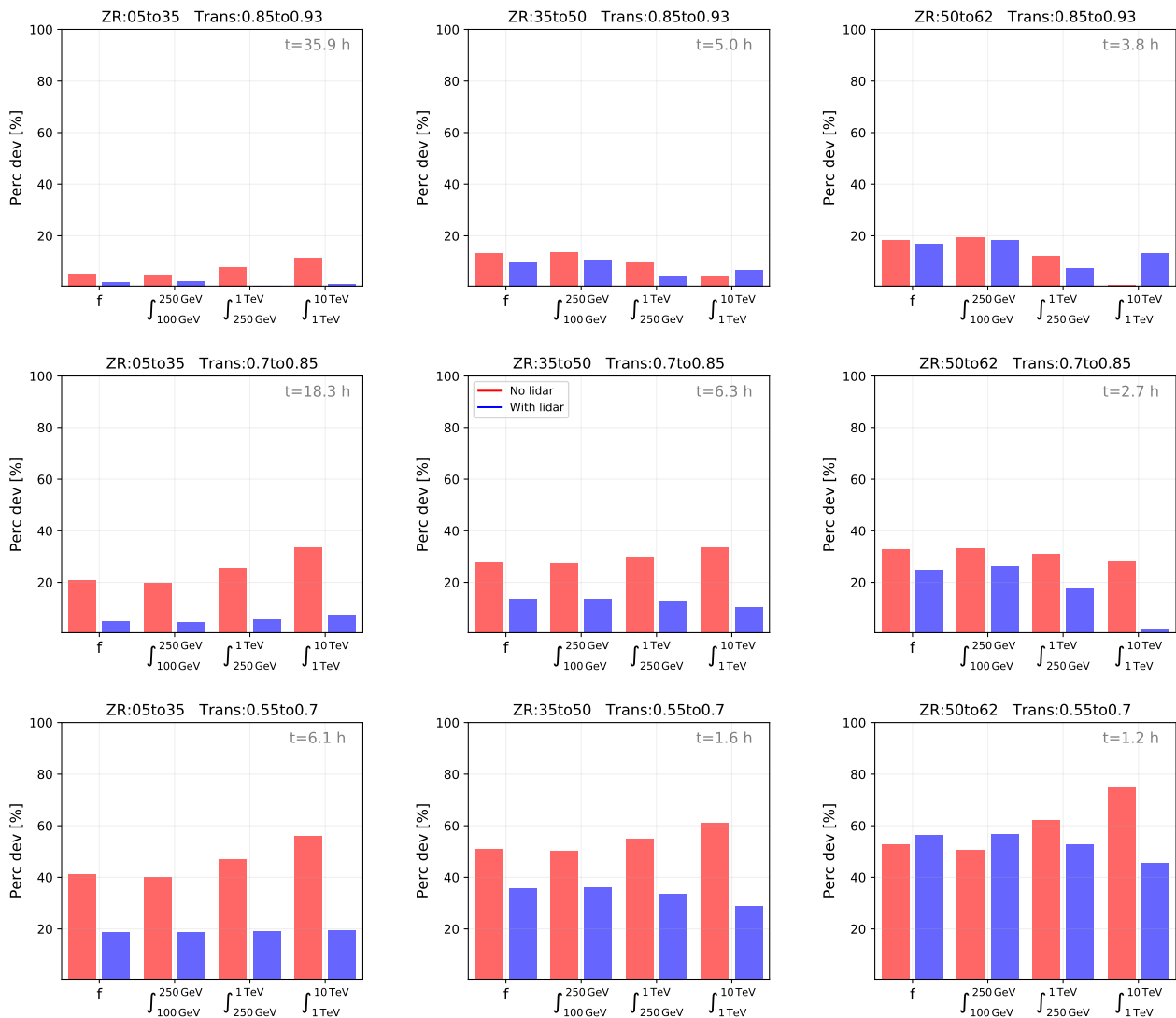


Figure 4.24: Percental deviation to the reference spectrum of the amplitude parameter and the integral over the fitted curve in three energy intervals for the uncorrected (red) and corrected (blue) period-averaged spectral fit. The effective time of the data used for the individual spectra is given in the top right corner of each subplot.

Overall, the LIDAR demonstrates an enormous correction power across all domains. It allows the regular usage of data with a corresponding transmission as low as 0.7 in the majority of cases. For low

zeniths, the systematic uncertainties originating from atmospheric conditions get more than halved and show the best improvements. Also for medium zeniths, substantial improvements restore the data almost completely above 0.7. In the high zenith domain, the results are less conclusive due the scarcity of data. Nevertheless, the findings suggests that the regular usage of data with transmission above 0.7 is enabled by applying LIDAR corrections. Depending on the goal of the analysis, data with a transmission down to 0.55 might be even usable although systematic uncertainties are larger. An example here would be the monitoring of variable sources or transients events, where maximal time coverage is beneficial.

4.3 Comparison of the correction algorithms

As it is shown in the previous sections, the data selection and analysis framework developed for this work can be used to precisely evaluate the current state of the LIDAR's correction abilities. Over the past, however, the MAGIC software was regularly updated and changed multiple times. In the transition from the MARS version V2-18-0 to V2-18-1, changes to the LIDAR's correction algorithm were performed, which are described in section 3.3.4. So far, the only direct comparison between both algorithms was performed after the software upgrade on a small data set covering only four nights. The time algorithm showed a better agreement with the chosen reference spectra. In order to compare the performance of both implementations of the correction algorithm in a more systematic and conclusive manner, the LIDAR corrections are applied with both MARS versions on the data set covering seven years of Crab data. The results are reported in the following two sections.

4.3.1 Comparison of the correction algorithms before unfolding

In the previous sections, the data were processed into spectra and unfolded as a last step using the forward unfolding approach implemented in *fold*. However, *fold* is only able to apply LIDAR corrections since the software upgrade of MARS V2-18-1. Therefore, the analysis pipeline used in the previous section can not be used for preceding MARS versions. The second unfolding program implemented in MARS is *CombUnfold*. It also allows the application of the forward unfolding method, but requires a manual tuning of the used energy regions of the true and estimated energy. This manual tuning needs to be performed iteratively for every single spectrum, and is hence not suited to process hundreds of spectra automatically and uniformly. The comparison of the algorithms on a nightly basis will nevertheless be performed in a similar way as before, but now with the analyzed spectra before applying the unfolding. The spectra are hence expressed in terms of estimated energy. This already contains the main impact of the correction and therefore still allows for a meaningful comparison.

Again, the data are classified into transmission and zenith angle bins and is then evaluated for three different energy regions. To isolate the overall effect, the mean deviations from the reference spectrum for a given parameter region are used in an analogous way to the previous sections. Starting at the lowest energies, figure 4.25 shows the percental and statistical deviations averaged over all available nights for the summed up flux below 250 GeV. The individual diagrams show three different bars, which correspond to the flux deviations without LIDAR corrections in red, with LIDAR correction using the event algorithm from MARS version V2-18-0 in green and lastly using the time correction

algorithm from V2-18-1 in blue. Uncorrected data show the same results for both versions. For the transmissions above 0.85, the results are very similar to each other and no clear performance difference

<250 GeV

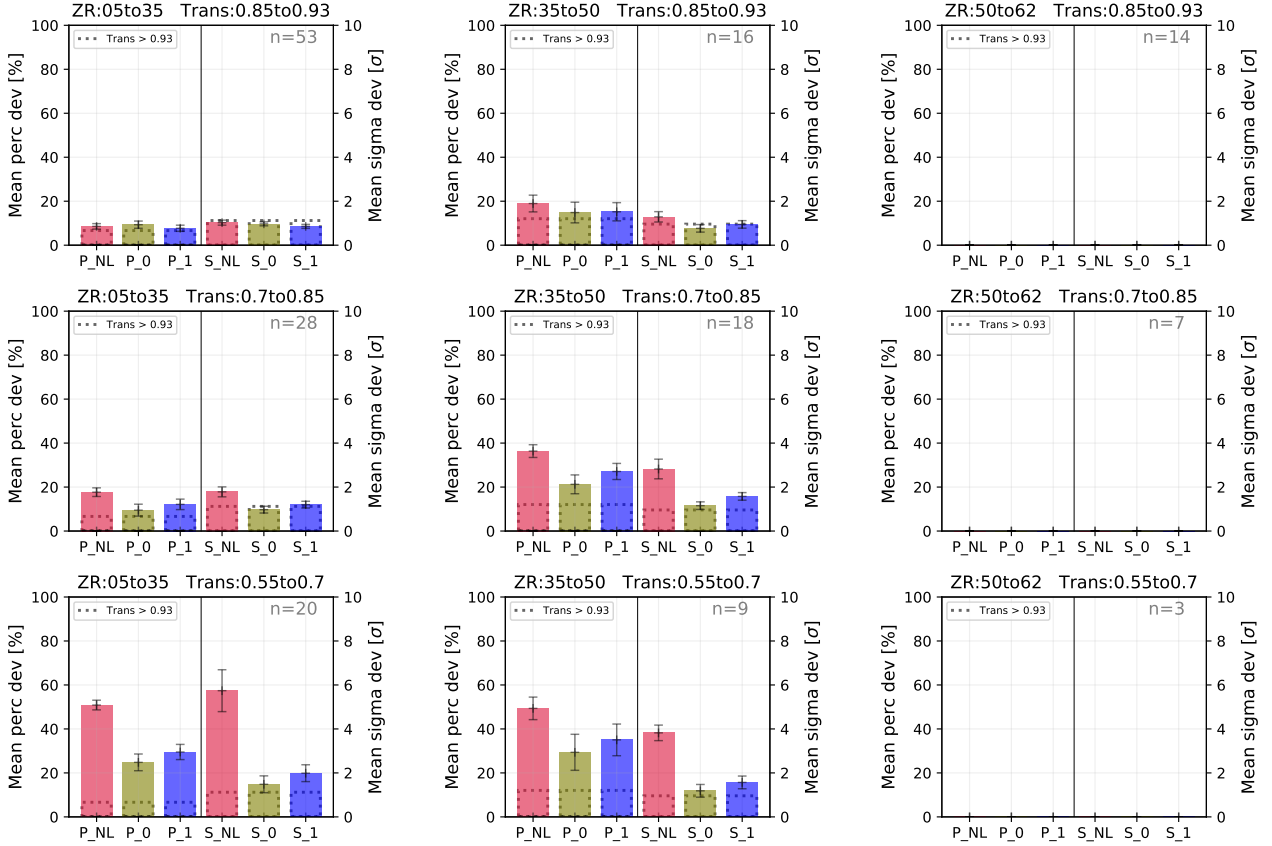


Figure 4.25: Mean percental (P) and statistical (S) deviation of the flux below 250 GeV from the reference spectrum without (red) and with (green/blue) LIDAR corrections from both correction algorithms for nine zenith and transmission bin combinations. The tags NL refer to no LIDAR correction, 0 to the event algorithm implemented in V2-18-0 and 1 to the time algorithm from V2-18-1. Due to the higher energy threshold above a zenith angle of 50° , the right plot does not contain data. The number of averaged nights is given in the top right corners. Benchmark values obtained from reference data set is given by the dashed black bars.

is observable. For the transmission bin between 0.7 and 0.85, differences become more apparent. For the lowest zeniths, the event algorithm shows only a marginally better performance, but for zeniths above 35° , the percental deviation improves from around 35% down to 20% for the event algorithm and down to only 25% for the time algorithm. This corresponds to a statistical improvement from almost 3σ down to around 1.3σ and 1.7σ , respectively. The last row depicts results from the lowest transmission bin with $T_{9\text{km}}$ between 0.55 and 0.7. For zeniths below 35° the percental deviations improves from around 50% on average down to 25% for the event algorithm and to around 30% for the time algorithm. This corresponds to an improvement of the statistical significance from above 5σ down to 1.5σ and 2σ respectively. The event algorithm hence results in a better correction in this first realm. A similar behavior is observed for the zeniths between 35° and 50° . Here, it shows a

better improvement on the percental side by achieving a correction down to around 30% and almost 1σ on the statistical side. The energy threshold for zeniths above 50° is again too high to acquire meaningful data below 250 GeV.

Looking at the energy range from 250 GeV to 1 TeV, shown in figure 4.26, the results for both methods are more similar. The performance difference for the transmission above 0.85 is quite similar for zeniths below 50° . In the highest zenith bin, however, event algorithm is almost 5% better and is able to fully reconstruct the flux observed in nights with perfect transmission. In the transmission bin between 0.7 and 0.85 the results are very comparable across the whole zenith angle range. The event algorithm, nevertheless, tends to perform slightly better at zeniths above 35° . Lastly looking at low transmission and low zeniths, there is almost no difference in the performance of both algorithms. They produce almost identical mean deviations with differences below 2% and 0.2σ . A stronger recognizable difference can be seen for zeniths between 35° and 50° . Here, the event algorithm shows a slightly better flux reconstruction on average by around 3% and 0.25σ . For the highest zeniths, the difference becomes less pronounced again with a minimally better result of the event algorithm.

250-1000 GeV

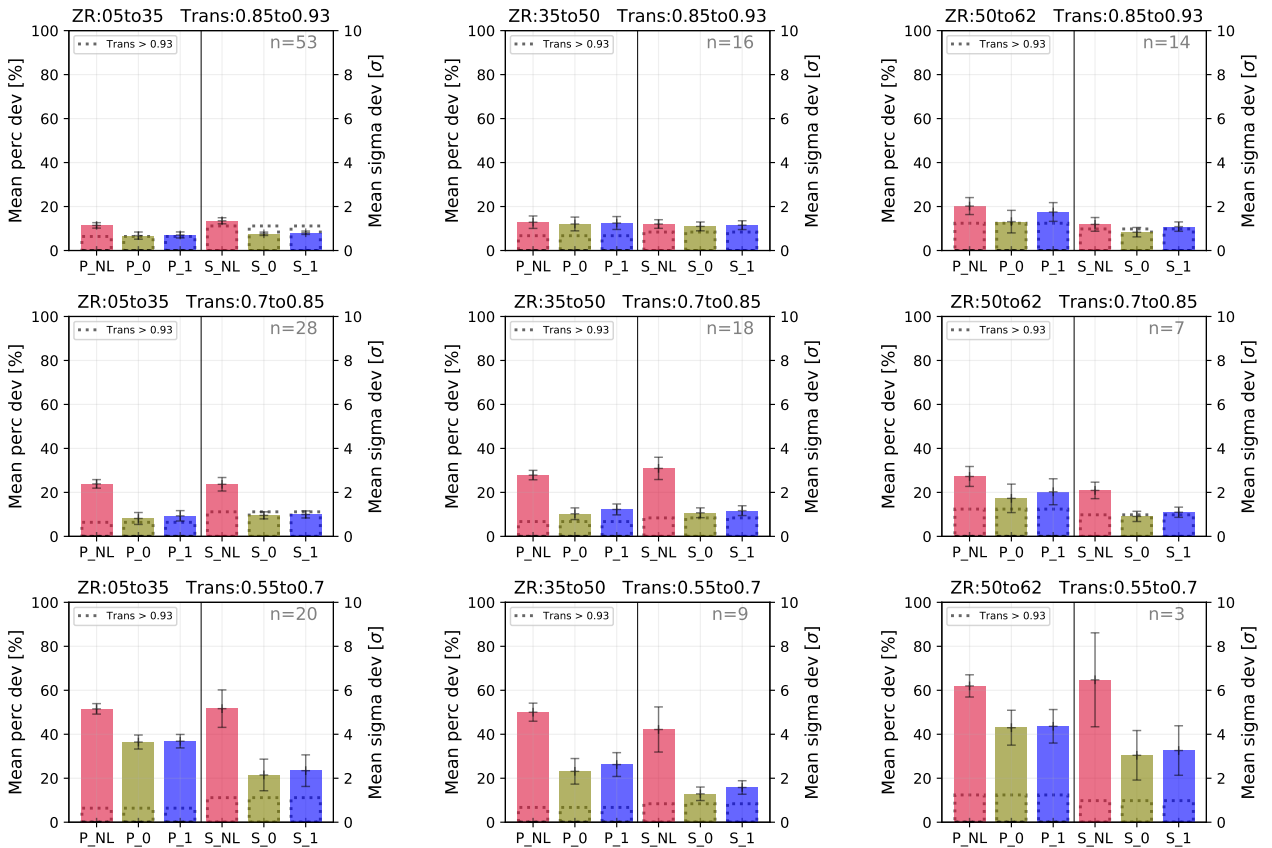


Figure 4.26: Same as figure 4.25, but for the energy region between 250 GeV and 1 TeV.

Lastly, the results for energies above 1 TeV are displayed in figure 4.27. The resulting fluxes of both algorithms differ even less in this regime. In the majority of cases the results agree within 2%.

However, in few cases the time algorithm now produces more accurate results. For low transmissions under medium zeniths as well as for high transmissions under high zeniths, the time algorithm produces spectra with less deviation by around 2%-4%.

As a first conclusion it can be said that the event algorithm shows a better performance at the pre-unfolded stage in the absolute majority of cases. The strongest differences can be observed for low energies and low transmissions. For higher transmissions as well as higher energies the distinctions between the different results become marginal.

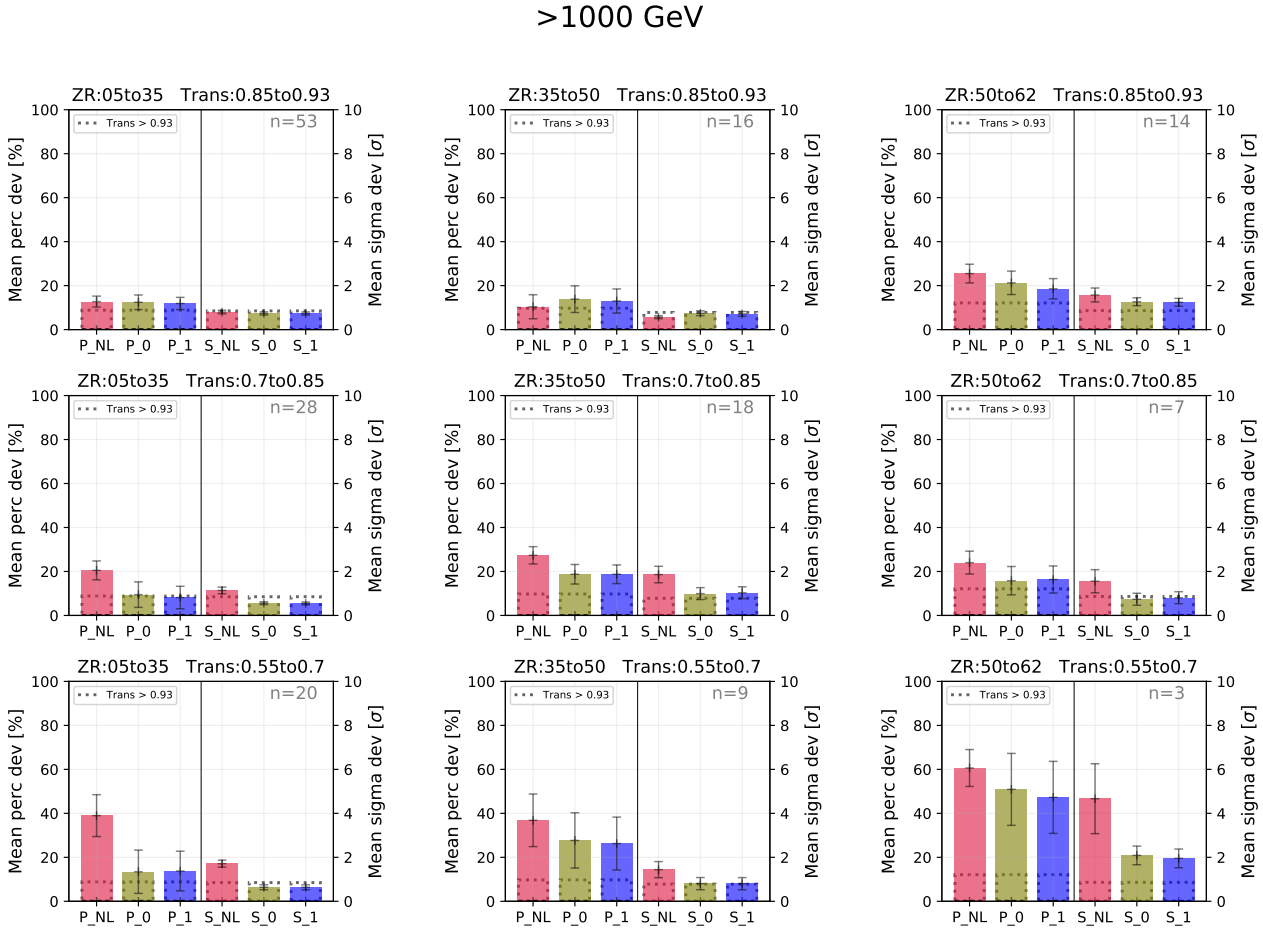


Figure 4.27: Same as figure 4.25, but for the energy region above 1 TeV.

In order to better understand the behavior of the two algorithms, two example spectra are shown in figure 4.28 and figure 4.29. The first shows an example night, where the time algorithm performs better. As was shown in previous results, the fluxes should not differ much for high energies. This is confirmed here by the good agreement of the data points above 300 GeV. For energies below that, the time algorithm (MARS V2-18-1) results in fluxes close to the reference spectrum, whereas the event algorithm (MARS V2-18-0) tends to overcorrect more and more for lower energies. The latter figure shows an example, where the event algorithm results in a more accurate reconstruction. As can be seen by the large deviation from all spectra, the atmospheric conditions were quite impairing. Nevertheless, the LIDAR achieves an impactful correction and the event algorithm shows a much

stronger correction. In general one can say, that the event algorithm tends to correct stronger in most cases, which is of great advantage when the atmospheric conditions are strongly impairing. In cases, where the transmission is only slightly impaired, the stronger correction can result in an overcorrection of the spectrum. The former point describes the predominant situation, which results in the unexpected overall advance in performance of the event algorithm.

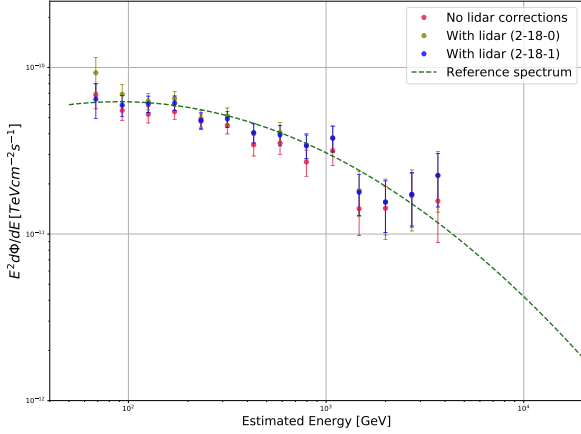


Figure 4.28: Example spectrum from January 29, 2020 during a transmission of 0.7 to 0.85. The spectrum produced by the event algorithm (V2-18-0) overshoots at low energies compared to the time algorithm (V2-18-1).

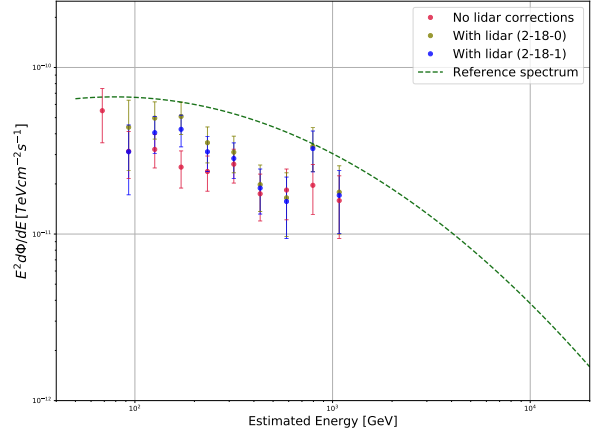


Figure 4.29: Example spectrum from December 6, 2018 during a transmission of 0.55 to 0.7. The spectrum produced by the event algorithm (V2-18-0) shows a stronger correction and hence more accurate reconstruction compared to the time algorithm (V2-18-1).

4.3.2 Comparison of the algorithms on unfolded period-averaged spectra

Investigating the behavior of the algorithms at the pre-unfolded stage allows a first estimate of the performance differences. For a completely valid comparison, however, the spectra need to get unfolded, since the LIDAR corrections are also incorporated in the unfolding procedure by altering the migration matrix as described in section 3.3.3. Because the usage of *CombUnfold* is not suited for the processing of hundreds of spectra, the comparison will be executed on the combined data sets, which were already used in section 4.2.3.

Figure 4.30 shows the resulting fits to the combined data set for the usual nine different transmission and zenith angle combinations. In red, the spectral fit produced by *CombUnfold* without applying any LIDAR corrections is shown as a baseline. The result from the event algorithm, meaning the MARS version V2-18-0, are given by the purple spectra. The new MARS version, V2-18-1, is able to apply LIDAR corrections with *CombUnfold* and *fold*, which is shown in cyan and dark blue respectively. Results from both can differ due to a different statistical treatment of the data in the implementation of the respective algorithms. This effect becomes most pronounced in cases of low statistics. Again, the reference spectrum is obtained by combining data from all available clear nights.

The relative difference of all spectral fits and SEDs to the reference spectrum can be seen in figure 4.31. Again, the differences of the fits become clearer. On first sight, all algorithms provide a substantial improvement to the reconstructed spectra. In most cases the event algorithm causes the strongest correction, which results in a better agreement with the reference. The quantitative evaluation is

again performed by taking the percental deviation of the amplitude parameter and the integral over the curve for three energy regions. The results are shown in figure 4.32.

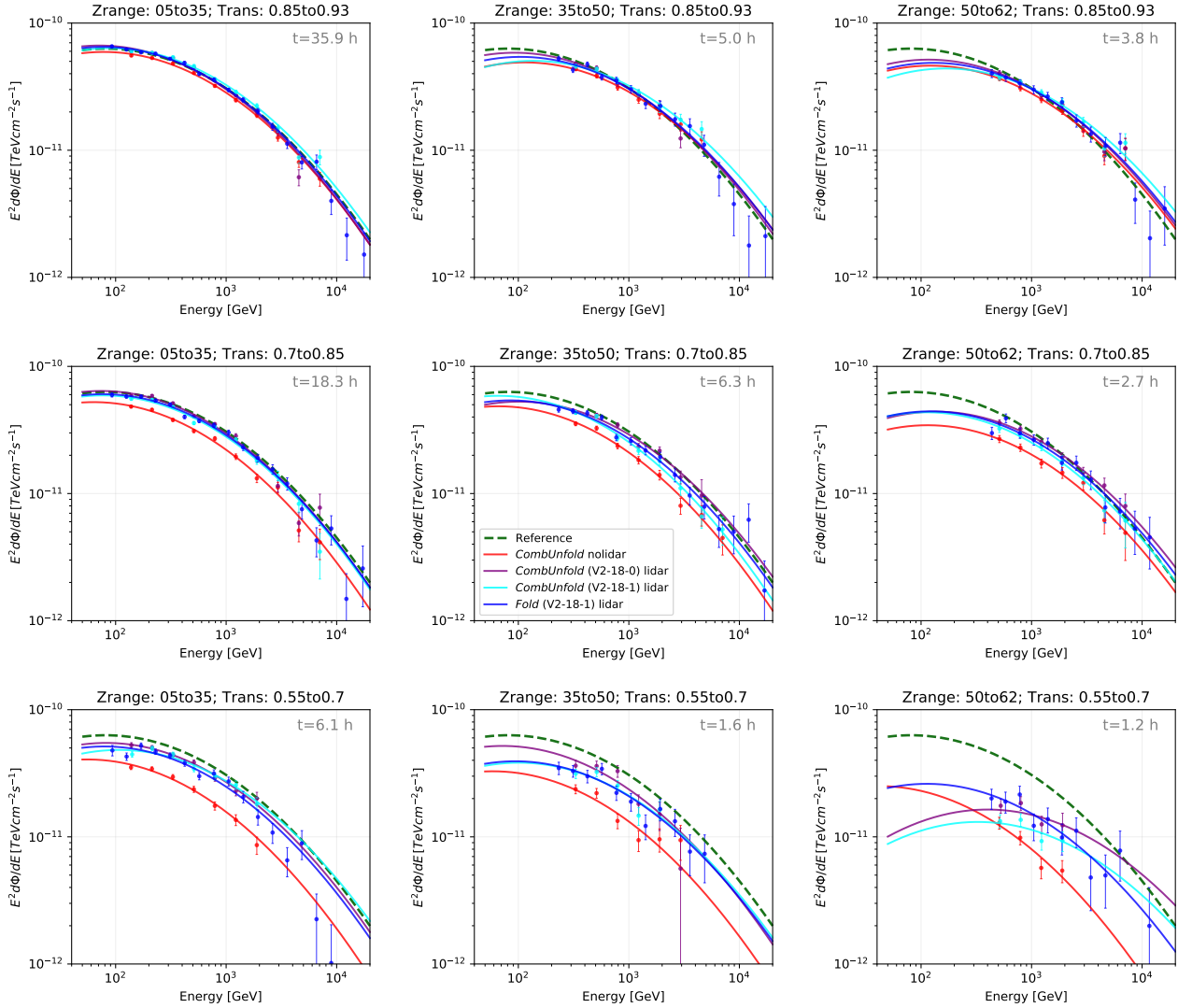


Figure 4.30: Spectra from the Crab Nebula derived with period-averaged data for nine different zenith angle and atmospheric transmission bins. Results are shown for *CombUnfold* with no corrections (red), the event algorithm from V2-18-0 implemented in *CombUnfold* (purple), the time algorithm from V2-18-1 implemented in *CombUnfold* (cyan) and the the time algorithm implemented in *fold* (blue). The reference spectrum is shown as the dark green dashed line. The effective time of the data used for the individual spectra is given in the top right corner of each subplot.

As can be expected, all versions produce satisfactory results for low zeniths under high atmospheric transmissions. In all areas the deviations are below 5% after applying corrections. The only exception is given by the new implementation in *CombUnfold* for high energies. Here, the fitted spectrum overshoots the reference spectrum. This overshooting at high energies can also be observed for the two remaining zenith bins, where it results in quite substantial deviations above 20%. The old *CombUnfold* version and *fold* produce more accurate and comparable results. The event algorithm, however,

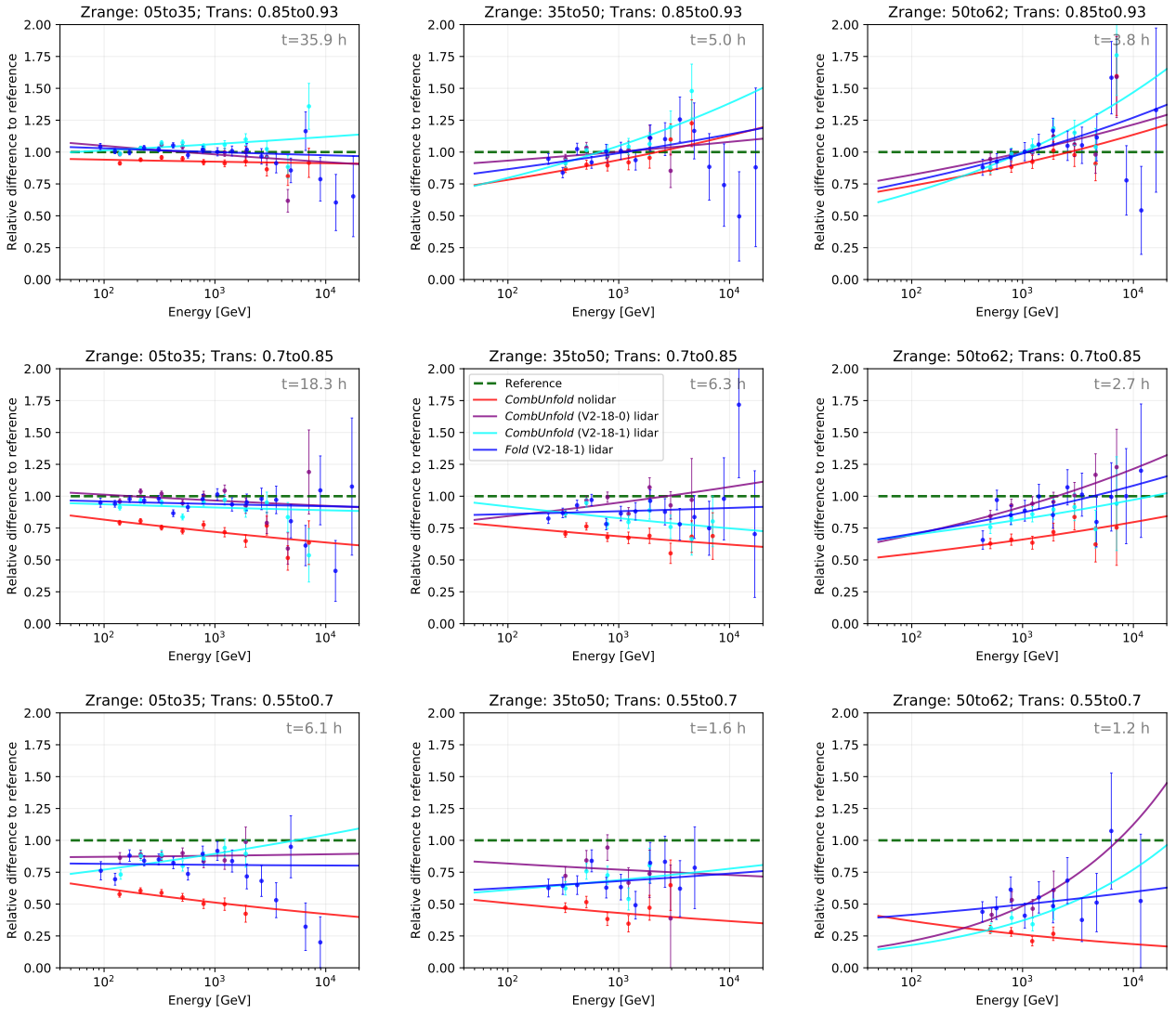


Figure 4.31: Relative difference of the period-averaged spectral fits to the reference for nine different zenith angle and atmospheric transmission bins for different correction algorithms. The effective time of the data used for the individual spectra is given in the top right corner of each subplot. The color coding is the same as in figure 4.30

continues to yield the best spectra with an improvement down to below 5% for medium zeniths and down to between 5% and 15% for high zeniths. In the low zenith region under medium transmissions, all three versions produce very accurate reconstructions. They all bring the mean deviation from above 20% down to 5%-10%. The event algorithm produces exceptionally good results with a matching of the amplitude parameter and flux at low energies to the reference by less than 1%. For the medium zenith bin, the results are comparable between the algorithm versions in most areas. For high energies the event algorithm again takes the lead in performance. In the highest zenith bin, all algorithms show rather large deviations for low and medium energy due to the lack of data constraining the fit. For the highest energies, the fit produced by *fold* gives the most accurate reconstruction followed closely by the event algorithm. Looking at low zenith angles during low transmissions, the different algorithms produce comparable results. All three implementations of the forward unfolding method result in a

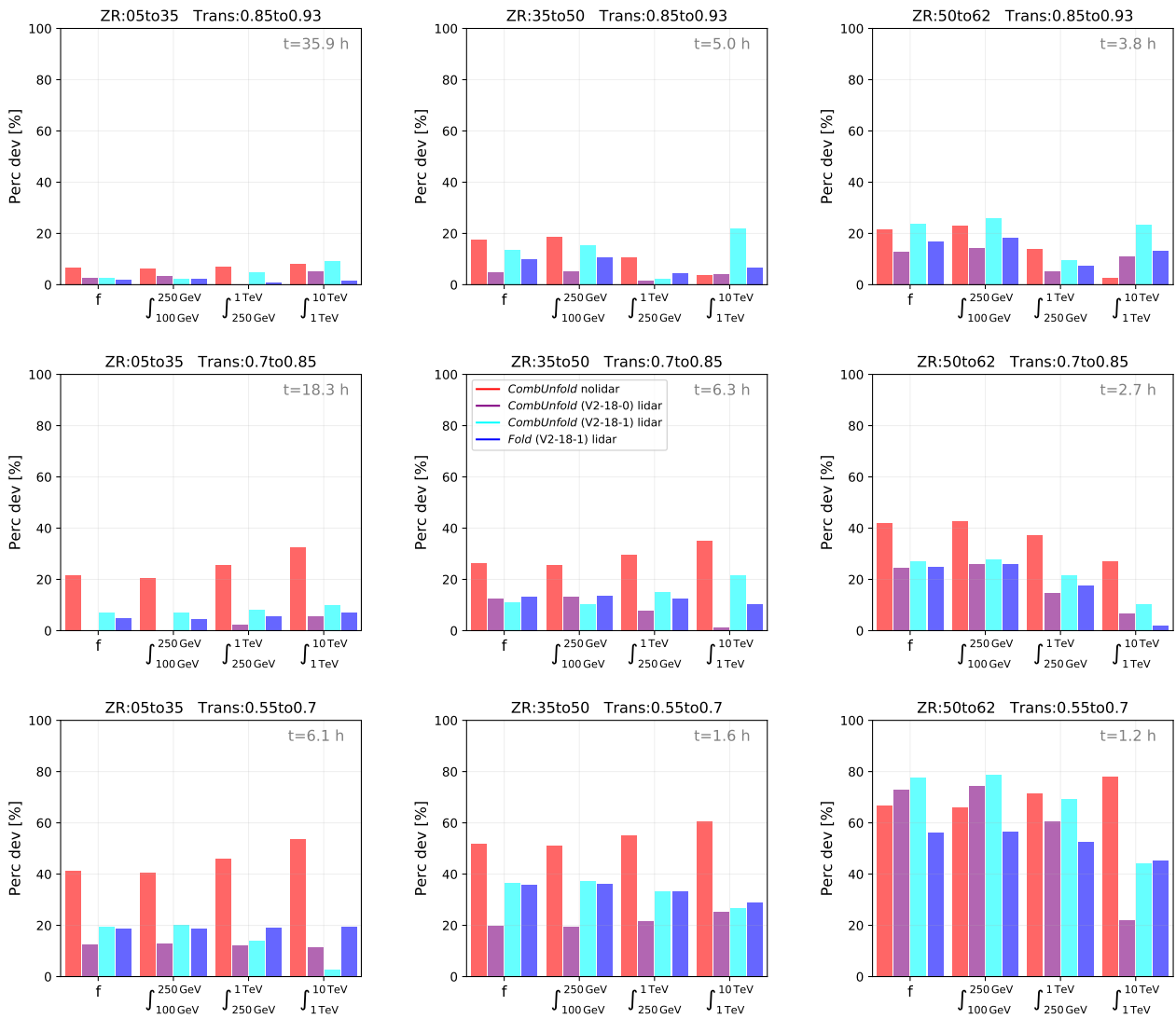


Figure 4.32: Percental deviation to the reference spectrum of the amplitude parameter and the integral over the fitted curve in three energy intervals for the uncorrected and corrected period-averaged spectral fit of different correction algorithms. The effective time of the data used for the individual spectra is given in the top right corner of each subplot. The color coding is the same as in figure 4.30

significant improvement over the uncorrected spectrum. For the amplitude parameter as well as for low and medium energies, the event algorithm produces the best results. It improves the deviations of above 40% in all regards down to around 15%. As can be seen from the spectra, the correction is stronger at low energies, which is advantageous for low transmissions, where the LIDAR tends to undercorrect. For higher energies, the fit from the new *CombUnfold* matches best. However, as can be seen by the distribution of data points, the amount of data and hence constraining power of the fit becomes rather little above 1 TeV. Going to higher zeniths between 35° and 50°, again the event algorithm shows the best performance due to the stronger correction. It achieves an improvement from above 50% deviation down to around 20%. The two new versions of the algorithm are more than 10% above this in most regards. For the highest zeniths, *fold* shows the best results. But looking at the spectra, it becomes apparent that 1.2 h of data under this transmission and zenith results in a

very poor statistics.

4.3.3 Discussion

The presented results from the last two sections indicate, surprisingly but conclusively, a better performance of the event algorithm in the vast majority of cases. There are two apparent possibilities of how to explain this behavior: Either the implementation of the time algorithm entails some form of software bug, that leads to an unexpectedly worse outcome in some situations, or the chosen changes to the event algorithm seem reasonable on first sight, but manifest themselves in an overall worse performance. The result of this work initiated a discussion about both options with the authors of the event and time algorithm. As of October 2021 no conclusive solution to the issue has been found. As described in earlier chapters, the ideal method for analyzing atmospherically impaired data is the building of tailored MC data, which is not feasible due to the complexity and variety of the possible conditions. Hence, the LIDAR correction algorithm makes approximations at several stages, to achieve a the best possible result. A critical stage of the algorithm is the averaging of the instrument response function over the observation time. Here, the two algorithm differ most and there is no unanimous agreement on which method is most reliable. Discussions will continue and will hopefully converge into an agreement about the method of averaging, that will produce the best final outcome.

5. Conclusion

The MAGIC telescopes at the Roque de Los Muchachos Observatory are one of the leading experiments in ground-based gamma-ray astronomy. They are a pair of IACTs with a mirror diameter of 17 m each, and can detect gamma radiation between 50 GeV and 50 TeV. IACTs observe primary gamma rays by detecting the Cherenkov light emitted by secondary particles of the induced air shower. They use the atmosphere as a calorimetric element in the detection process. Through this technique, effective areas in the order of km^2 are achieved, which enables a wide-reaching energy range as well as the observation of very low photon fluxes, compared to satellite experiments, that typically have effective areas of around 1 m^2 . However, the atmosphere is subject to environmental conditions at any given time, and represents an uncontrollable external factor to the experiment. The atmospheric conditions of the observation site can change on the timescale of minutes up to a seasonal variability due to the occurrence of higher dust levels or the presence of clouds. The higher aerosol content in the atmosphere can decrease the brightness of the shower image detected by the telescope camera, and reduce the trigger efficiency of the telescope. These effects lead to a wrong reconstruction of individual events, which can lead to incorrect high-level scientific results, like the obtained gamma-ray flux in a given time interval. IACTs, therefore, greatly benefit from a real time range-resolved monitoring of the atmospheric conditions to characterize and select good-quality data data, as well as to correct atmospherically impaired data.

The main instrument of the MAGIC collaboration for this purpose is the MAGIC LIDAR, which was built by the MPP group and is operated continuously since 2013. It is the only LIDAR operating together with an IACT in real time. The LIDAR is located under a protective dome on top of the control building of the MAGIC telescopes. It emits short laser pulses at 532 nm at a rate of 250 Hz from a Q-switched, frequency-doubled Nd:YAG laser with $25 \mu\text{J}$ pulse energy. The emitted light gets absorbed and scattered by the presence of molecules and aerosols in the atmosphere. A 60 cm aluminium mirror collects the backscattered portion of the light, and focuses it into a hybrid photo detector (HPD). Using the information about the arrival time and signal intensity, the atmospheric transmission caused by aerosols can be extracted. This allows an accurate evaluation of the present atmospheric condition, and with that information one can further evaluate the quality of the data taken with the MAGIC telescopes. Furthermore, it allows the correction of atmospherically impaired data.

The importance of applying corrections provided by the LIDAR system is varying with the scientific goal of the respective analysis. Very sensitive analyses, e.g. searches for Dark Matter in dwarf galaxies, might put very stringent constraints on the allowed atmospheric transmissions, and may use data taken under exceptionally clear atmosphere. In these cases, the signal is normally expected to be constant

with time, and the specific time of observation does not matter. Because of that, one can easily select data from time intervals with an atmospheric transmission from 9 km larger than 0.85. In cases, however, where the exact timing of the observation is of great importance, one is forced to use the data that may have been taken under sub-optimal atmospheric conditions, and the LIDAR system becomes indispensable. Examples here are transient events like GRBs, flares of AGNs or the possible case of a galactic supernova. Sub-optimal atmospheric conditions can then have a serious impact on the quality and scientific success of the observations. It is hence necessary to have an operating LIDAR system to either fully or partially recover the gathered data, and have an accurate estimate of the reliability of the data at hand.

This thesis provides the most accurate study about the impact of applying LIDAR corrections to atmospherically impaired data taken by the MAGIC telescopes. Previous investigations relied only on very small data sets of up to a few nights, and the validity of the results was very limited. In this work, I used almost seven years of data from the Crab Nebula and a dedicated set of scripts to perform a systematic study over many different conditions. The data with a transmission from 9 km above 0.93 were used to establish accurate reference spectra for individual analysis periods of MAGIC to have the best possible reference for comparison. The remaining data with transmissions between 0.55 and 0.93 was then classified by their atmospheric transmissions to investigate the correction potential for different degrees of impairment. Further classifications into zenith angle and energy ranges allowed an even more nuanced analysis.

In short, the results can be summarized as the following: In the vast majority of cases, a transmission from 9 km above 0.85 is sufficient to use the data without applying corrections. In case there is LIDAR data available, using it still provides small improvements, and is recommended. In the region between 0.7 and 0.85, the usage of LIDAR data is strongly recommended. The distortions in the gamma-ray spectra are larger and one needs the LIDAR corrections to reconstruct the actual spectrum of the source. The corrections achieve a full recovery of the actual spectrum for zeniths below 35° and a very close to accurate reconstruction for zeniths above 35° , where the impact of the non-perfect atmosphere is even larger. Data below 0.7 should not be used if data with systematic uncertainties below 20% are desired. The corrections improve the data profoundly, but do not achieve a full correction. These guidelines can be used by future analyzers of MAGIC data to better judge the reliability of their data for the intended scientific purpose.

Besides investigating the current performance of the LIDAR corrections, the selected data and methods of this work were also used to compare different versions of the correction algorithms. Surprisingly, the old algorithm, which uses an event-based averaging (instead of a time-based method) to compute the effective area, resulted in a better reconstruction for the performed tests. The interpretation of this result and proper way to resolve this issue is still under discussion within the MAGIC collaboration. Any future modifications in the software and correction algorithm can be easily tested and compared to previous performances using the now prepared data set and analysis pipeline that I built. It can therefore function as a standard tool for the comparison of algorithms.

I also made several minor hardware improvements to the LIDAR system and contributed to the trouble-free operation of the LIDAR system by resolving a long standing issue in its operation. These interventions helped to avoid future down time periods and simplified the maintenance of the LIDAR.

The presented work of this thesis allows for follow-up investigations at several points. A first limitation of this study is the exclusive usage of data taken under conditions with minimal background light of the night sky, primarily caused the presence of the Moon. This is referred to as *dark data*. A significant fraction of MAGICs observation time happen during higher light background levels, which increases the trigger threshold, and the analysis energy threshold of MAGIC. The influence of atmospheric conditions might then be deviating from their behavior under low-light background. The investigation of extended data sets taken under higher moon background levels would allow to also draw precise statements of the correction abilities of the LIDAR under conditions of higher night sky background. Another possible extension of this work could be achieved by including another reference source than the Crab Nebula. The Crab Nebula is an exceptional stable and bright source, but is only visible between September and April. This covers the majority of the year, but leaves out the hottest summer months, where the influence of Calima is strongest. The atmospheric impairment in the analyzed data set is hence mostly caused by the presence of clouds in the colder winter months. Including a source visible in the summer months would enable a more detailed investigation of the data correction under Calima, and would allow a better comparison of different weather phenomena. On the hardware side, further upgrades to the LIDAR are also desirable. The current aluminium mirror used in the LIDAR was installed in 2008, and shows a serious degradation of reflectivity due to environmental impact. During the work on this thesis, I investigated several options for a new mirror for the LIDAR and I contacted different mirror manufacturers. After discussion with my colleagues at the MPP group we decided to purchase a 61 cm mirror made from borosilicate glas with a quartz protected aluminium coating made by the Italian manufacturer *Media Lario S.r.l.*. The expected delivery time of the mirror is mid to end of October, 2021. Since the manufacturing and assembly of the new mirror was not completed within the time scope of this thesis, it was not further discussed.

The MAGIC collaboration has pioneered the application of LIDAR systems to correct IACT data, and is currently the only IACT collaboration that is successfully operating a LIDAR system for atmospheric monitoring and correcting impaired data. The insights gained during the development of the LIDAR and the characterization of its performance presented in this work will be of great value to future observations with MAGIC, as well as to the next generation of IACTs. The third generation of IACTs, namely CTA, is currently being constructed. CTA will rely on LIDAR systems to monitor and characterize atmospheric conditions of their observation sites. The usage of LIDAR systems will hence be further refined and continue to be a critical part of ground-based gamma-ray astronomy for the next decades.

A. Investigation and resolution of recurring LIDAR crashes

As part of my master thesis program, I became part of the team responsible for the LIDAR system within the MAGIC collaboration. During my time working as a master student, I addressed a long standing problem in the operation of the LIDAR. In the years from 2018 until 2020, the LIDAR repeatedly stopped operating, apparently due to a crash of the instrument with the protective dome. This happened rarely at the beginning, but the number of crashes increased in the year 2020, where it happened multiple times over the summer and autumn. The last collision took place in October, 2020. As a result of this incident, the instrument suffered several damages as is shown in figure A.1. The LIDAR seemed to have hit the dome on the side, where the laser guidance tube is mounted. The impact heavily bent down the laser guidance tube (figure A.1 (a)). The tube is attached close to the beam expander, and aims to reduce any remaining stray light after the beam leaves the expander. Since the tube needs to be very precisely aligned coaxial with the laser beam, any slight nudge to the tube makes the LIDAR non-operational. Additionally to the tube, the telescope spider, which mounts the detector and with one of its legs also the guidance tube, got damaged (figure A.1 (b)). The inner part of the LIDAR dome indicates the location, where the LIDAR seems to have hit the dome. Figure A.1 (c) shows some scratches and dents from the collision. Since the laser guidance tube is mounted on the same plate as the laser itself, any impact to the tube also leads to misalignment of the transition from beam expander to guidance tube as well as the laser itself (figure A.1 (d)). For the operation the laser also needs to be aligned very precisely to achieve an early overlap with the telescopes field of view. The plate can be adjusted in two axis by screws, but is very sensitive to external impact. An incident like this results in a downtime of the LIDAR until the local staff on La Palma realign the tube and the laser. The laser can only be realigned during the night, and the process can take up to several hours. Therefore, the reoccurring of such incidents reduced the operation time of the LIDAR, and resulted in fraction of the MAGIC data not being supplemented by LIDAR data.

A common pattern of some of the crash nights was the scheduling of sources at very large zenith angles (VLZA), meaning zenith angles above 70° . As a first assumption, it was therefore suspected that the LIDAR collides with the dome when moving to high zenith angles. Since the LIDARs telescope frame is longer than the dome's inner radius, it is placed off center and can only move completely free in the northern direction. A high-zenith observation in southern direction could cause a collision, but it should be restricted by software limits. The incidence happened during night time, and the shifters could not investigate the problem immediately. They have to ensure the ongoing operation of MAGIC



(a) Bent down laser guidance tube



(b) Bent aluminium cross of the detector mount



(c) Marks of impact on the inner dome



(d) Misaligned transition from laser beam expander to guidance tube

Figure A.1: Hardware damage and misalignment as a consequence of the LIDAR crash in October, 2020.

and also lack the specific knowledge to tackle problems of subsystems.

In order to investigate the issue and resolve the cause of the collisions, I traveled to La Palma for three weeks in November, 2020. As a first measure, the LIDAR was moved through several azimuth and zenith combinations to sample the full range of motion of the LIDAR. I did not find any problematic position or possibility of collision. To exclude that the LIDAR might take an unusual path at certain coordinate transitions, due to the equatorial telescope mounting system, I tried all scheduled MAGIC sources from the nights, where crashes occurred. Recreating the paths from the crash nights did also not result in any LIDAR movement that could have caused a collision. However, I noted that during operating the LIDAR manually for longer amounts of time, the mount controller of the telescopes tends to freeze from time to time. The problem is easily fixed by rebooting the controller. After the reboot, however, the mount controller loses the information about the current position, and resets its coordinates to certain default values, that were set to $AZ=-99^\circ$, $ZA=-99^\circ$. Only after parking, the telescope resets to the correct coordinate values. At that moment, I understood that this could be the root-cause creating the above-mentioned crashes of the telescope with the dome.

When the shifter personnel of MAGIC notices a problem with the LIDAR, e.g. freezing of the mount controller, they are instructed to power cycle the affected component, shutdown, and then restart the LIDAR again, which solves the majority of issues. However, in case the mount controller is affected, this can result in the wrong transmission of coordinates. During the shutdown procedure the dome

checks if the telescope mount is in parking position by checking the coordinates with only upper limits. A wrong coordinate transmission, such as $AZ=-99^\circ$, $ZA=-99^\circ$, can lead to a miscommunication, and causes the dome to close with the LIDAR still being in an upright position. The LIDAR is then clamped by the closing dome, and the hardware damage described earlier can be the result. I checked the log reports of the concerned observation nights and noticed that such reboot due to a previously occurring problem happened in all nights. The concurrent scheduling of VLZA observations was therefore only a coincidence.

In order to resolve this software vulnerability, all positional checks in the LIDAR software were extended to also verify whether the coordinates describe a reasonable position in the first place. Moreover, the verification of a successful parking position was set more stringent. In the long term, also an external hardware check in the form of a contact sensor might be helpful to verify the parking position externally as well, to provide two independent checks before the dome closes. As of October 2021, no collision of the LIDAR system occurred again since the software intervention, which demonstrates that the problem was successfully identified and corrected.

B. A new laser guidance tube and target for laser alignment

During my three-week stay at the MAGIC site (see Appendix A), two minor hardware upgrade were implemented as well. First, the old laser guidance tube was replaced. As pointed out previously, the old tube is prone to get misaligned easily by slight nudges or bumps. Besides the former collisions, the tube can also be displaced by accidental contact of people performing maintenance tasks inside the dome or by shifters manually parking the LIDAR in case of problems. Additionally, the old tube was made from leftover materials from the MAGIC telescope frame, and the diameter was not perfectly suitable. Since the diameter does not match the outer diameter of the laser beam expander well, a wide gap between the two components remain, where stray light can escape.



Figure B.1: CAD image of the new guidance tube with inserted baffle rings to reduce stray light.



Figure B.2: Implemented tube setup directly mounted at the laser plate and screwed on to the beam expander with no gap.

In order to address all these drawbacks, I replaced the tube by a shorter and better fitting tube. The manufacturer of the laser beam expander, *Thorlabs*, also provides stackable optical tubes that can be directly attached to the expander (see CAD image in figure B.1). Hence, no gap is created, and no stray light can escape sideways. Two different tube lengths allow for the adjustment of the total tube length to the desired length. Since the inner diameter of the optical tubes is larger than the beam width, baffle rings were additionally inserted to reduce the remaining stray light. The guidance tube is now only mounted on the laser plate, as can be seen in figure B.2. Therefore, the laser and the tube can be aligned together in one move, which simplifies the alignment procedure.

As previously described, the realignment of the laser with the telescope's field of view is performed during the night. One person is modifying the two axis determining the pointing direction of the laser,

whereas another person needs to monitor the return signal. The direction modifies until a maximum return signal can be identified. The process can take up to 2-3 hours, and during the time the LIDAR cannot be used to supplement observations with MAGIC. To simplify this alignment procedure, a laser target (figure B.3) was built during my stay on La Palma. It consists of two glass panels holding an adjustable thin sheet of paper in between. The glass panels are screwed on two pieces of metal, which can be mounted rigidly on the top of the telescope. The idea is to align the laser only once with the previously described method. Afterwards the target is attached, and the paper with the target symbol is moved in alignment with the laser beam and fixed. The illuminated target is shown in figure B.4. The target is then removed and the LIDAR can operate normally. In case any future disturbance causes the need for realignment, the target can then be mounted again and the laser beam pointed at the target symbol. This needs to be performed by two people as well, but can be carried out during the day. This makes it more convenient for the local personnel, and does not cause any downtime during the nightly data taking with MAGIC.



Figure B.3: Attachable target for laser alignment during the day.



Figure B.4: Attached target to the telescope frame illuminated by the expanded laser beam.

Bibliography

- A. Aab et al. Inferences on mass composition and tests of hadronic interactions from 0.3 to 100 EeV using the water-Cherenkov detectors of the Pierre Auger Observatory. *PRD*, 96(12):122003, Dec. 2017. doi: 10.1103/PhysRevD.96.122003.
- M. G. Aartsen et al. Multimessenger observations of a flaring blazar coincident with high-energy neutrino IceCube-170922A. *Science*, 361(6398):eaat1378, July 2018. doi: 10.1126/science.aat1378.
- B. P. Abbott et al. Observation of Gravitational Waves from a Binary Black Hole Merger. *PRL*, 116(6):061102, Feb. 2016. doi: 10.1103/PhysRevLett.116.061102.
- B. P. Abbott et al. Gravitational Waves and Gamma-Rays from a Binary Neutron Star Merger: GW170817 and GRB 170817A. *ApJL*, 848(2):L13, Oct. 2017. doi: 10.3847/2041-8213/aa920c.
- F. A. Aharonian. Very High Energy Gamma Rays and Origin of Galactic Cosmic Rays. In *22nd Texas Symposium on Relativistic Astrophysics*, pages 168–181, Jan. 2005.
- M. Ahlers. Neutrino Sources from a Multi-Messenger Perspective. In *European Physical Journal Web of Conferences*, volume 209 of *European Physical Journal Web of Conferences*, page 01013, Sept. 2019. doi: 10.1051/epjconf/201920901013.
- J. Albert et al. Unfolding of differential energy spectra in the MAGIC experiment. *Nuclear Instruments and Methods in Physics Research A*, 583:494–506, 2007. doi: 10.1016/j.nima.2007.09.048.
- J. Aleksić et al. Measurement of the Crab Nebula spectrum over three decades in energy with the MAGIC telescopes. *Journal of High Energy Astrophysics*, 5:30–38, Mar. 2015. doi: 10.1016/j.jheap.2015.01.002.
- J. Aleksić et al. The major upgrade of the MAGIC telescopes, Part I: The hardware improvements and the commissioning of the system. *Astroparticle Physics*, 72:61–75, Jan. 2016a. doi: 10.1016/j.astropartphys.2015.04.004.
- J. Aleksić et al. The major upgrade of the MAGIC telescopes, Part II: A performance study using observations of the Crab Nebula. *Astroparticle Physics*, 72:76–94, Jan. 2016b. doi: 10.1016/j.astropartphys.2015.02.005.
- W. B. Atwood et al. The Large Area Telescope on the Fermi Gamma-Ray Space Telescope Mission. *ApJ*, 697(2):1071–1102, June 2009. doi: 10.1088/0004-637X/697/2/1071.

- C. R. Benn and S. L. Ellison. Brightness of the night sky over La Palma. *New Astron. Rev.*, 42(6-8): 503–507, Nov. 1998. doi: 10.1016/S1387-6473(98)00062-1.
- K. Bernlöhr. Impact of atmospheric parameters on the atmospheric Cherenkov technique*. *Astroparticle Physics*, 12(4):255–268, Jan. 2000. doi: 10.1016/S0927-6505(99)00093-6.
- J. Cervantes-Cota, S. Galindo-Uribarri, and G. Smoot. A Brief History of Gravitational Waves. *Universe*, 2(3):22, Sept. 2016. doi: 10.3390/universe2030022.
- A. De Angelis and M. Pimenta. *Introduction to Particle and Astroparticle Physics*. 2018. doi: 10.1007/978-3-319-78181-5.
- C. Fruck. *The Galactic Center resolved with MAGIC and a new technique for Atmospheric Calibration*. PhD thesis, TUM, 2015.
- C. Fruck, M. Gaug, R. Zanin, D. Dorner, D. Garrido, R. Mirzoyan, and L. Font. A novel LIDAR-based Atmospheric Calibration Method for Improving the Data Analysis of MAGIC. In *33rd International Cosmic Ray Conference*, 3 2014.
- J. A. Hinton and W. Hofmann. Teraelectronvolt Astronomy. *Annu*, 47(1):523–565, Sept. 2009. doi: 10.1146/annurev-astro-082708-101816.
- K. G. Jansky. Radio Waves from Outside the Solar System. *Nature*, 132(3323):66, July 1933. doi: 10.1038/132066a0.
- M. S. Longair. *High Energy Astrophysics*. 2011.
- S. G. Mashnik. On Solar System and Cosmic Rays Nucleosynthesis and Spallation Processes. *arXiv e-prints*, art. astro-ph/0008382, Aug. 2000.
- R. Orito, E. Bernardini, D. Bose, A. Dettlaff, D. Fink, V. Fonseca, M. Hayashida, J. Hose, E. Lorenz, K. Mannheim, R. Mirzoyan, O. Reimann, T. Y. Saito, T. Schweizer, M. Shayduk, and M. Teshima. Development of HPD Clusters for MAGIC-II. *arXiv e-prints*, art. arXiv:0907.0865, July 2009.
- A. N. Otte. *Observation of VHE γ -Rays from the Vicinity of magnetized Neutron Stars and Development of new Photon-Detectors for Future Ground based γ -Ray Detectors*. PhD thesis, Munich, Tech. U., 2007.
- I. Puerto-Giménez, M. Gaug, R. Barrena, J. Castro, M. Doro, L. Font, M. Nieves Rosillo, J. Zamorano, and C. Consortium. Characterization of the candidate site for the Cherenkov Telescope Array at the Observatorio del Teide. In *International Cosmic Ray Conference*, volume 33 of *International Cosmic Ray Conference*, page 2976, Jan. 2013.
- T. M. Shaffer, E. C. Pratt, and J. Grimm. Utilizing the power of Cerenkov light with nanotechnology. *Nature Nanotechnology*, 12(2):106–117, Feb. 2017. doi: 10.1038/nnano.2016.301.
- M. Spurio. *Probes of Multimessenger Astrophysics*. 2018. doi: 10.1007/978-3-319-96854-4.

- T. C. Weekes, M. F. Cawley, D. J. Fegan, K. G. Gibbs, A. M. Hillas, P. W. Kowk, R. C. Lamb, D. A. Lewis, D. Macomb, N. A. Porter, P. T. Reynolds, and G. Vacanti. Observation of TeV Gamma Rays from the Crab Nebula Using the Atmospheric Cerenkov Imaging Technique. *ApJ*, 342:379, July 1989. doi: 10.1086/167599.
- R. Zanin, E. Carmona, J. Sitarek, P. Colin, K. Frantzen, M. Gaug, S. Lombardi, M. Lopez, A. Moralejo, K. Satalecka, V. Scapin, and V. Stamatescu. MARS, The MAGIC Analysis and Reconstruction Software. In *International Cosmic Ray Conference*, volume 33 of *International Cosmic Ray Conference*, page 2937, Jan. 2013.

Acknowledgements

Finally, I would like to take this opportunity to thank all those who made this thesis possible and supported me during my time at the MPP.

First of all I want to thank Béla Majorovits for agreeing to serve as the official supervisor of this thesis. Also thanks to David Paneque, Razmik Mirzoyan and Masahiro Teshima for accepting me as a student in their group. My biggest gratitude goes to David, my day-to-day supervisor, for taking me under his wings, guiding me through this work and helping to proofread the thesis at the end.

Many thanks also to Alexander Hahn, Martin Will, Razmik Mirzoyan and Diana Werner for fruitful discussions or supporting me whenever I needed help. I would also like to thank the rest of the MPP gamma-gay group for welcoming me into the group and the great working environment, even though we barely saw each other during the last year.

I want to thank the MAGIC collaboration and all its members, especially Markus Gaug, Christian Fruck, Abelardo Moralejo and Victor Acciari, for their support in many ways.

Also thanks to my close friends and roommates for the great times and simply getting through lockdowns together. Since this also marks the end of my studies, I want to thank my parents, grandparents and brother from the bottom of my heart for their never-ending support. They have made all of this possible and given me the opportunity to pursue the things I love. Lastly, I would like to thank my girlfriend, Alma, for always being there for me and making the last months of this thesis an absolutely wonderful time.